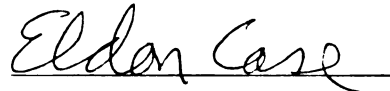This is to certify that the

thesis entitled

Acoustic Emission, Internal Friction and Young's
Modulus in a Mechanically Fatigued GFRP Composite
and Macor, a Glass-Ceramic Composite

presented by

Karl Andre Tebeau

has been accepted towards fulfillment
of the requirements for

_____Master's_____ degree in _Materials Science_

Eldon Case

Major professor

Date _January 30, 1991_

PLACE IN RETURN BOX to remove this checkout from your record.
TO AVOID FINES return on or before date due.

DATE DUE	DATE DUE	DATE DUE
_____	_____	_____
_____	_____	_____
_____	_____	_____
_____	_____	_____
_____	_____	_____
_____	_____	_____
_____	_____	_____

MSU Is An Affirmative Action/Equal Opportunity Institution

c:\circ\datedue.pm3-p.1

ACOUSTIC EMISSION, INTERNAL FRICTION AND YOUNG'S
MODULUS IN A MECHANICALLY FATIGUED GFRP COMPOSITE
AND MACOR, A GLASS-CERAMIC COMPOSITE

BY

KARL ANDRE TEBEAU

A THESIS

Submitted to
Michigan State University
in partial fulfillment of the requirements
for the degree of

MASTER OF SCIENCE

Department of Metallurgy, Mechanics
and Materials Science

March 1991

Abstract

ACOUSTIC EMISSION, INTERNAL FRICTION AND YOUNG'S MODULUS IN A MECHANICALLY FATIGUED GFRP COMPOSITE AND MACOR, A GLASS-CERAMIC COMPOSITE

By

Karl A. Tebeau

The low cycle mechanical fatigue behavior of two types of modern composite materials is explored. The damage induced changes in Young's modulus and internal friction are compared to acoustic emission (AE) detected from the specimen during four point bending. Changes in Young's modulus and internal friction are measured by using the sensitive sonic resonance method. Extensive qualification of the AE data was undertaken, to determine the validity of the AE data taken during the fatigue testing.

The specimens produced substantial AE throughout the flexural cycle. Since it was shown that the AE detected at the points of load reversal was contaminated by system noise, only the AE detected during the midstroke was determined to be fit for analysis. The AE produced during midstroke was noncontinuous, with some parts of the load range being more acoustically active that others, indicating that damage production was also noncontinuous.

Several trends were observed in the data. The maximum changes in the two monitored physical properties increased with increasing maximum fatigue load. Changes of Young's modulus and internal friction for both materials evolved in an unexpected manner, increasing and decreasing periodically throughout fatigue life. It is believed that a fast acting, aggressive recovery mechanism may be at work, periodically set back by continued fatigue flexure.

I am pleased to dedicate this thesis, the culmination of my efforts at M.S.U. to my parents: for their support - both moral and financial, their understanding, perseverance and for not selling off my stuff while I finished.

Acknowledgements

Table of Contents

List Of Tables

List Of Figures

1.   Introduction.

Mechanical fatigue is an important damage source in both polymeric and ceramic composites.   This experimentation explores the low cycle mechanical fatigue behavior of two very different types of modern engineering composite materials: 3 - M composition type 1003, a unidirectionally reinforced glass fiber - epoxy composite and Macor, a glass - ceramic composite.

A comprehensive literature search and review covers the topics necessary to provide a solid basis with which to evaluate and explain the behavior of the materials under testing.   A review of testing methods includes four point bend stressing and sonic resonance determinations of Young's modulus and internal friction. Acoustic emission is examined at length, including terminology, damage emission and analysis methods.   Fatigue processes in both materials are extensively examined, to include relevant mathematical models and recent qualitative mechanical models.

Experimentally, a low cycle fatigue schedule was followed which systematically increasd the maximum applied load per specimen until failure regularly occured.   Changes in Young's modulus and internal friction were monitored to characterize the evolution of damage as it accumulated under continued fatigue loading.   Acoustic emission was simultaneously recorded and later compared with the changes in the physical properties.

Comparison to current work by colleagues and previous studies involving thermal shock may enable us to draw an estimate of internal damage and perhaps an equivalent thermal shock fatigue.

2. Review of literature.

2.1. Inspection and testing techniques.

2.1.1. Nondestructive test methods.

Nondestructive evaluation methods are available that can measure small changes in physical properties. When used in conjunction with other tests, the sonic resonance technique for determining the internal friction and dynamic Young's modulus provides an estimate of a specimen's damage, crack growth resistance, remaining strength and fracture energy [10-14].

2.1.1.a. Internal friction.

Any vibrating solid structure will consume its own vibrational kinetic energy and eventually come to rest, even though it may be totally isolated from its environment [14]. This energy loss effect is known as internal friction. Internal friction characterizes an energy absorbing (or dissipating) mechanism that provides displacement damping as an exponential 'ring-down' of the specimen's vibration. Internal friction arises due to microcracks, grain boundaries, second phases, voids, pores and other smaller contributions in the host material [14].

Several methods, direct and indirect, exist for the measuring of internal friction [10-21]. Specific loss or damping capacity is the most direct method, described theoretically by Kolsky [18], as the ratio

$$\Delta W / W = \text{Damping Capacity} \qquad (1)$$

where

ΔW = energy loss in the specimen during one stress cycle

W = elastic strain energy stored in the specimen at maximum strain.

Indirect methods for determining internal friction rely on the assumptions that frictional or energy absorbing mechanisms are proportional to velocity. This implies that the mechanical damping is of viscous nature, and that the restoring forces are proportional to displacement from the neutral position, further implying Hookean behavior [10-14].

A qualitative measure of internal friction is the relative spread or sharpness of resonance [14]. A plot of the specimen's vibrational amplitude versus driving frequency (at constant RMS amplitude), shows a local maximum at F_r, the fundamental flexural resonant frequency [10, 11, 14, 17-20]. Figure 1 illustrates some vibrational modes of prismatic bars. Other resonant frequencies also show local maxima, but the fundamental flexural mode of vibration is the most easily detected.

The sharpness of the peak is inversely proportional to the internal friction [14]. A specimen with a sharper resonance than another can be said to have a lower internal friction. Relative sharpness can be easily measured by determining the spread of the frequency response at some chosen reference level, usually the 'half power' point, i.e. 0.707, or 0.5 maximum amplitude. This is known as the 'full width at half maximum' method of peak analysis, and is normalized to the resonant frequency [14]

$$Q^{-1} \sim \Delta F / F_r \qquad\qquad (2)$$

where

ΔF = peak width in frequency, at chosen point of reference.

a)

b)

0.224 L

c)

0.132 L

d)
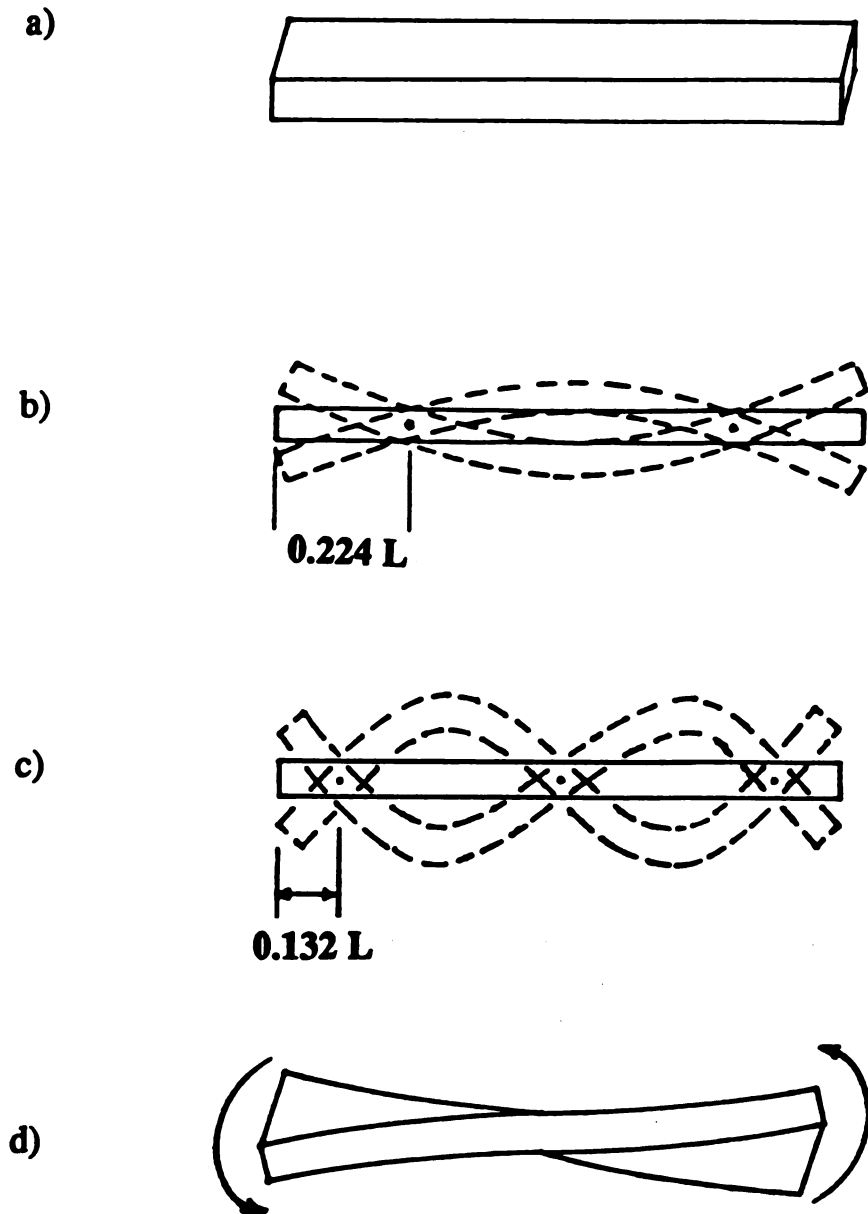
Figure 1. 'Free-free' vibrational modes of prismatic bars. a) quiescent,
b) flexural fundamental, c) first flexural harmonic or overtone,
d) torsional fundamental.

Zener [14, 19] shows that this ratio is related to specific loss (Equation 1) as

$$\Delta F / F_r \;=\; (\sqrt{3} / [2\,\pi])\,(\Delta w / w). \tag{3}$$

A typical definition of internal friction that is used today is the quantity Q^{-1}, derived by Kolsky [14, 18] from analogy with electrical theory, and is defined as

$$1/Q \;=\; Q^{-1} \;=\; \Delta F / \sqrt{3}\, F_r. \tag{4}$$

For low internal friction (less than 10^{-2}) measured at frequencies above 100 Hz [14], it is expedient to use Forster's free-decay method [10-16, 20]. Forster's relationship is written as

$$Q^{-1} \;=\; \ln(A_0 / A_t) / \pi f t \tag{5}$$

where

Q^{-1}	=	internal friction of specimen
A_0	=	driven vibrational amplitude of specimen
A_t	=	vibrational amplitude at threshold
f	=	driven frequency, usually fundamental flexural
t	=	time between driver cutoff and last output cycle to cross threshold
$ft = N$	=	number of times output crosses threshold.

Figure 2 illustrates a typical ring-down output from a driven specimen after cutoff.
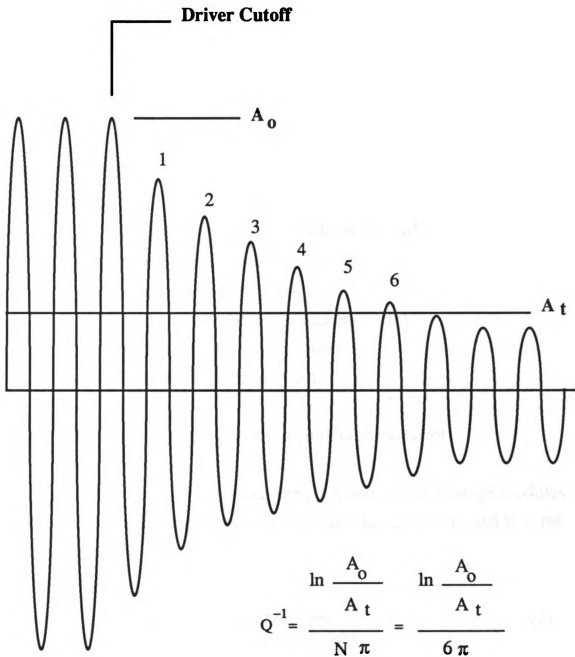
Figure 2.   Sample ring-down output from specimen in sonic resonance.

2.1.1.b.   Dynamic Young's modulus.

Dynamic Young's modulus can be calculated in several ways. One method, used by some researchers [13, 14] is as follows

$$E_d = (9.467 \times 10^{-7})L^3 m f^2 / d^3 b \qquad (6)$$

where, in cgs units

E_d = dynamic Young's modulus (dyne/cm^2)

L = length of specimen (cm)

m = mass of specimen (g)

f = fundamental flexural frequency (Hz)

d = thickness of specimen (cm)

b = width of specimen (cm).

The constant premultiplier is a unitless shape factor.

A second and more widely used approach to dynamic Young's modulus is derived from a relationship developed by Lord Rayliegh [21], and is of the form [13, 14, 21]

$$E_d = (48 \pi^2 \rho L^4 F_r^2) / (m^4 d^4) \qquad (7)$$

where, in cgs units

E_d = dynamic elastic modulus of the bar (dyne/cm^2)

ρ = bulk density of bar (g/cm^3)

L = length of bar (cm)

F_r = fundamental flexural frequency of bar (Hz)

m = mass of bar (g)

d = thickness of bar (cm)

Note : 100 dyne/cm^2 = 1 MPa.

In Equation 7, Lord Rayliegh made several simplifying approximations. Most importantly, that the motion of the bar's elements perpendicular to its length in the plane of flexure is assumed to be the only significant contribution to the kinetic energy of the vibrating bar [14, 21].

Dynamic Young's modulus is typically about 0.1 to 5 percent greater than the static Young's modulus. This phenomena is due to thermodynamic effects during measurement. In general, the difference amounts to adiabatic (dynamic) versus isothermal (quasi-static) methods of measurement, i.e. sonic resonance versus slow pull-test, respectively [14, 27]. In the dynamic test, heat builds up during compression, especially near the free surface (where maximum compression occurs). Compression at the free surface of the specimen leads to heating, and the heat build up causes the lattice to expand thermally. This effect negates, to a small degree, the effort of the driving transducer to displace or vibrate the bar. The lattice expansion gradient results in an apparent increase in stiffness, which is read by the pickup transducer as an increase in the flexural fundamental frequency. The increased frequency is interpreted through Equation 7 as an increase in Young's modulus [27, 28].

2.1.1.c.   Damage versus change in internal friction and Young's modulus.

A change in internal friction or Young's modulus can be interpreted as a measure of internal damage in a specimen [14].   Any change in internal friction or Young's modulus during mechanical flexural fatigue is expected to be due primarily to an increase in microcracking and void formation. This damage will be developed and accumulated by cyclic mechanical loading in four-point bend.

Internal friction is expected to increase as internal damage increases, and thus track the evolution of damage, when plotted against the number of fatigue cycles.

2.1.2   Destructive test methods.

Flexural strength or modulus of rupture (M.O.R.), is defined by the American Society for the Testing of Materials as "the maximum stress in a mode of flexure that a specimen develops at rupture; normally, the calculated maximum longitudinal tensile stress at mid-point of the specimen test span surface" [23-25].

Summary of methods:

Method I: 3-point bend. The bar rests on two cylindrical support pins and is loaded by means of a loading pin midway between the lower loading pins. All load pins should be identical and cylindrical to avoid specimen indentation and to minimize stress concentration at the points of loading.

Method II: 4-point bend. The bar rests on two cylindrical support pins

and is loaded at the two quarter points by means of two loading pins, each an equal distance from the adjacent support point. The distance between the loading pins is one half that of the support pin span.

For three- and four-point bend fixtures, the load bearing contact points should all be identical and have cylindrical edges to minimize indentation of the specimen, or failure due to stress concentration directly under the loading pins may occur (Figures 3 and 4). Load bearing pin diameter should be a minimum of 3.175 mm (1/8 inch) and no greater than the specimen's thickness.

Recommended geometry specifications are [23-25]

L/d = 16   Requires $20 \geq L/d \geq 2$ i.e. support span should be sixteen times the specimen thickness.

L/b = 4   Requires $L/b \geq 0.8$ i.e. support span should be four times the width.

b/d = 4   Requires $b/d \geq 1$ i.e. width should be four times the thickness

where

L = support span, m or in

d = thickness of specimen, m or in

b = width of specimen, m or in.

Flexural strength in four point bend is calculated by the following equation [23-25]

$$\sigma = 3PL/4bd^2 \qquad (8)$$
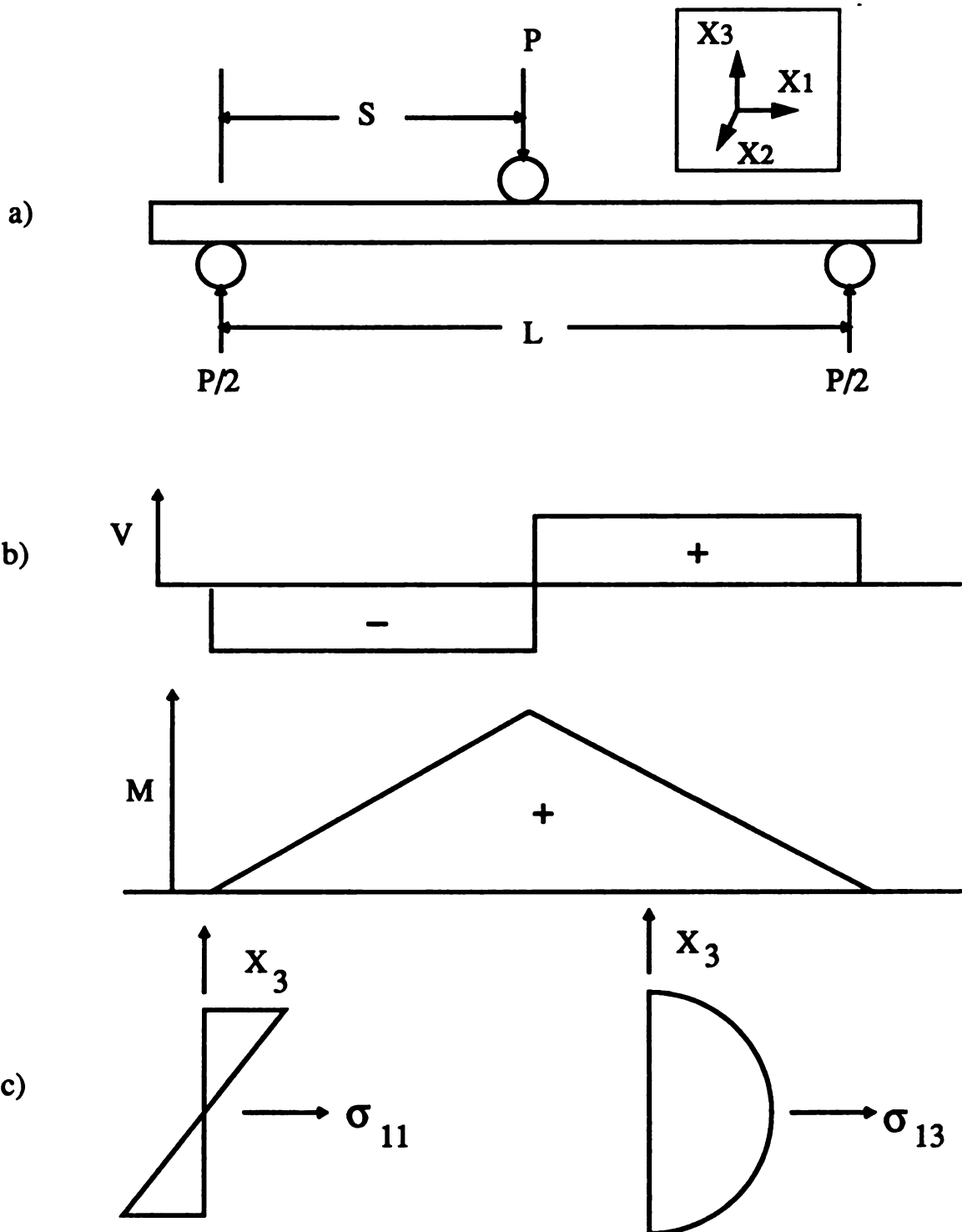
Figure 3. Schematic and static force profiles for three-point bending test. a) dimensional parameters, b) shear force (V) and bending moment (M) distributions along X_1 axis, c) flexural stress (σ_{11}) and shear stress (σ_{13}) distributions in the thickness direction.
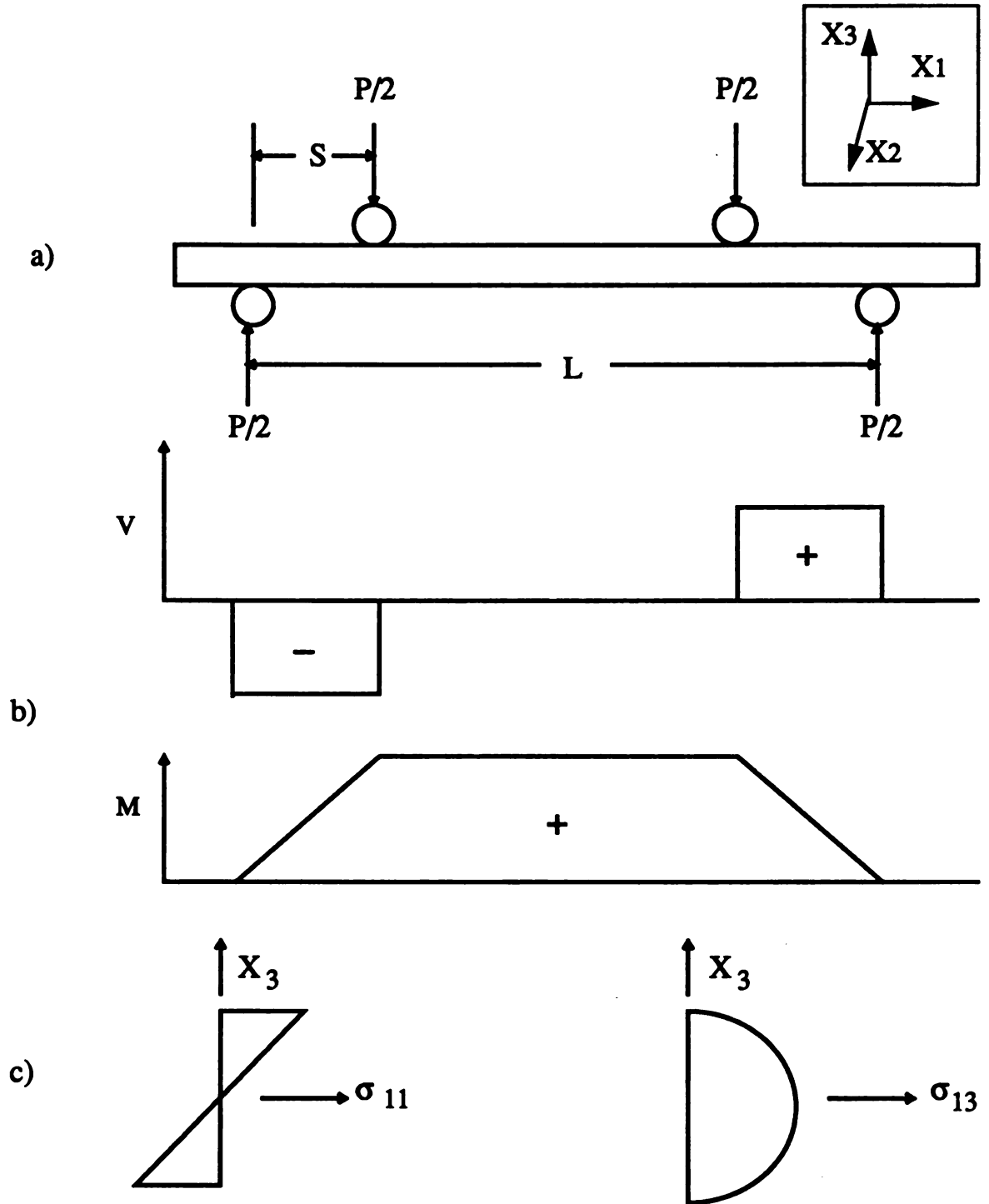
Figure 4. Schematic and static force profiles for four-point bending test. a) dimensional parameters, b) shear force (V) and bending moment (M) distributions along X_1 axis, c) flexural stress (σ_{11}) and shear stress (σ_{13}) distributions in the thickness direction.

where

σ =   flexural strength, MPa or psi.

P   =   load at fracture, N or lbf

L   =   distance between long span of supporting fixtures (roller pins), m or in.

b   =   width of specimen, m or in.

d   =   thickness of specimen, m or in.

Note: if P is read in kgf, σ will be calculated in kgf/mm^2. To obtain σ in MPa with P in kgf, multiply the right side of Equation 8 by 9.807. If σ is desired in ksi and P is recorded in lbf, divide the right side by 1000 [23-25].

The mean flexural strength value of the test lot should be calculated as

$$\sigma = (\sigma_1 + \sigma_2 + \ldots + \sigma_n) / n \tag{9}$$

where

σ =   mean value of flexural strengths for the test lot

$\sigma_1 \ldots \sigma_n$ =   individual specimen flexural strengths

n   =   number of specimens.

The sample standard deviation should be calculated as follows

$$s_{(n-1)} = \{[(\sigma_1 - \sigma)^2 + (\sigma_2 - \sigma)^2 + \ldots + (\sigma_n - \sigma)^2] / (n - 1)\}^{1/2} \tag{10}$$

where

$s_{(n-1)}$ =   sample standard deviation, MPa or psi.

2.2.   Acoustic emission background.

2.2.1.   Physical background.

Acoustic emission (AE) analysis has developed over the past twenty years as an important NDE tool. AE monitors and interprets the elastic stress waves generated by the swift, local redistributions of stress associated with many damage mechanisms.

AE methods may be preferable to the other NDT methods of transmission X-radiography and ultrasonic C-scan, by virtue of real time analysis and the ability to locate damage. Only after significant damage is detected acoustically, in real time, may it be necessary to remove the specimen from the test rig for a more detailed inspection. Multiple AE transducers can in some cases, accurately determine the location of damage by time-of-flight computations.

Acoustic signals are generated within a solid when a defect-containing solid is mechanically stressed [5, 29-45], undergoes some phase change or when a defect is created within an otherwise homogeneous solid [38-40]. The spectral amplitude distribution of the acoustic signal depends on the magnitude and character of the defect [29-45]. Therefore, several intensity thresholds or ranges may exist, depending on the defect structure and their ability to generate AE within the solid [29-34, 36-40, 42, 44, 45].

Dislocation motion in metals exhibits the lowest theoretical level of acoustic emission intensity, but with millions of dislocations sweeping through a volume of material simultaneously, their total acoustic energy may be detected as strain rate dependent [42]. In 1980, Dickinson showed that what many people had previously interpreted as dislocation induced acoustic emission, resulted from an oxide coating that was cracking and separating [45]. Dickinson tested in tension two types of electropolished specimens

made of a 1350 aluminum alloy in a high vacuum (10^{-4} Pa). The specimens were nominally identical, but some had the addition of a 30 mm^2, 300nm thick patch of anodized oxide coating on the gauge section. Dickinson showed that the AE from the patch area of the anodized specimen was over four orders of magnitude greater than the AE from the clean specimen, which gave nearly negligible AE above the background noise of the system [45].

Other common examples of acoustic emission include the well known 'tin cry', associated with Type I deformation twinning in tin single crystals under tensile stress, which can sometimes be heard with the unaided ear [42, 46]. Detectable levels of acoustic energy are also produced during the onset of phase transformations such as retained austenite to martensite in HSLA steels [40] and piezoelectric response and poling effects in PZT (lead zirconate titanate) [38, 39]. A moving defect such as a crack opening or extending [29-34, 36-45] may also generate acoustic emission. This is a manifestation of the Kaiser effect [31, 46], which describes the release of acoustic emission only when the threshold of the previous highest load is exceeded.

Under flexural loading, the surfaces of the crack grate against each other (this is not crack growth, but mechanical contact of opposing crack faces). Frictional asperity contact with grinding and pulverization of debris within the crack may prevent closure [30, 34]. Crack rubbing may generate a level or type of AE (different from that of cracking AE), which is continuously emitted during flexure. Crack rubbing may allow the Kaiser effect to separate 'new damage' AE from continuously-generated frictional AE, if an unambiguous acoustic signature for cracking can be determined.

When an internal microcrack initiates or extends, part of the material is fracturing and creating internal space. Crack extension may occur rapidly with new internal surface areas swept out by the advancing crack front. Alternatively, slow crack growth may fracture and separate a few grains at a time. Both rapid cracking and slow crack growth can fracture transgranularly

(along grain boundaries) or intragranularly (through the grain) [29-37].

During slow crack growth, intermittent bursts of AE energy are released which may be detectable above the background noise of the detection system [30-33]. A slow crack propagating through a matrix with dispersed second phase particles may be modeled roughly by a dislocation in a metal with harder second phases present. The advancing crack front is arrested by two nearby second phase particles. Under continued loading, the crack tip stress intensity rises and the crack front bows out between the two particles [31] (Figure 5). Finally, the crack front either breaks around the particle, or overcomes the strength of the binding particle which then fractures, and the crack front advances to the next set of pinning points [31].

The minimum time required for a microcrack to extend only a few grains is on the order of a few nanoseconds [31], but the acoustic signal is generated for a much longer time due to vibration or ringing of the crack faces, analogous to the ringing of a bell for a time after it is struck. The Rayliegh velocity is the upper speed limit for crack propagation in a solid [31]. Table 1 lists wave velocities for several ceramic materials. Empirically, crack velocities are often much slower [30, 34].

The frequency distribution for an initially sharp pulse broadens as a function of propagation distance [35]. Also, higher frequencies attenuate more with distance than lower frequencies [35].

Elastic stress waves are an inseparable mixture of several different wave types. The wave types of relatively large amplitudes (highest energy) are the longitudinal (compression) and transverse (shear) waves[41]. These two wave types accompany each other but travel by different modes and at different velocities [35, 38, 41]. Shear waves travel at about half the compression wave velocity [38, 41] (Table 1). In practice, the amplitude of the stress wave being sensed depends on where the AE transducer is located and the distance it is from the source. Since AE is sensed on the suface of a

Direction of crack propagation

a)

b)

c)

d)

Fractured
Particles
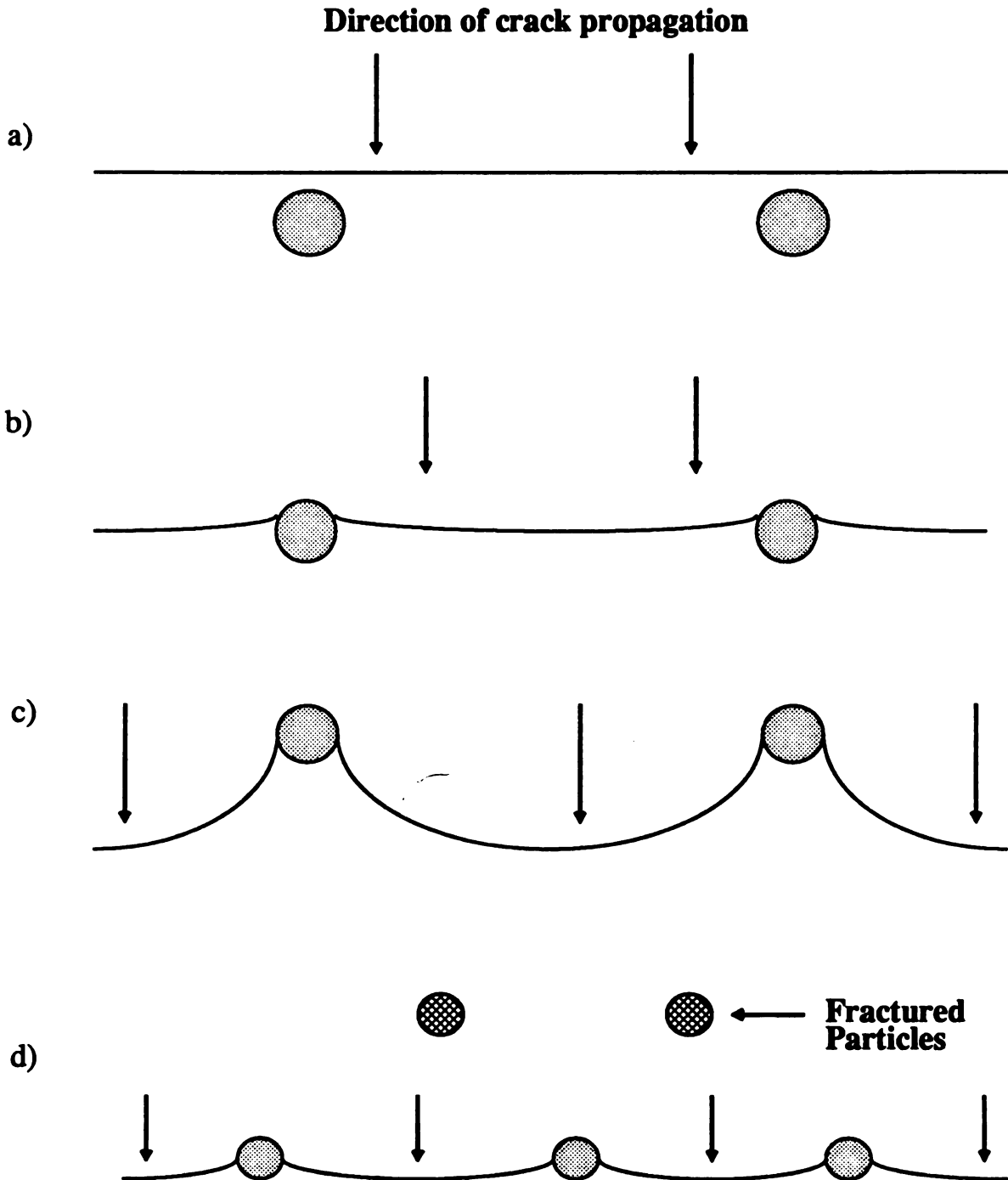
Figure 5. Schematic of crack advancement sequence in a ceramic composite
material. a) crack approaches hard second phase particles, b) crack is arrested
by particles, c) crack front bows out past particles, d) crack front breaks free
of pinning particles, advancing to next set of pinning particles.

18

Table 1. Acoustic wave velocities for several ceramic materials [38, 41, 44].

Material	Wave type	Wave velocity
Si_3N_4	compression	6 mm/μsec
	shear	3 mm/μsec
	Rayliegh	4 mm/μsec
Al_2O_3 *	compression	11.0 mm/μsec
	shear	6.7 mm/μsec
SiO_2 **	compression	6 mm/μsec
	shear	3.8 mm/μsec
PZT ***	compression	3.9 to 5.0 mm/μsec
	shear	1.8 to 2.1 mm/μsec

*   Average of Voight and Reuss values.

**   Values cited are for fused silica. Porosity will decrease wave velocity, up to an order of magnitude for a highly porous specimen.

*** Lead Zirconate Titanate.

specimen, Rayliegh elastic surface waves, are important [27, 41, 44].
A tuned piezoelectric transducer coupled to the surface may sense these elastic
stress waves as acoustic emission. The acoustic energy is transmitted by
atomic displacements.

Several other wave types are also present. Stonely waves travel along
interfaces such as grain boundaries and fiber/matrix boundaries [41], where
differences in elastic modulii exist across an interface. Lamb waves [41, 44],
plate and leaky plate waves [41] become important in specimens thin enough
to allow communication between opposite surfaces. Lamb and Stonely waves
typically have much lower amplitudes than longitudinal (compressive) or
transverse (shear) waves [41, 44].

The interaction of elastic stress waves is an extremely complicated
situation and is beyond the scope of this discussion. As a minumum
comment, it is sufficient to say that elastic stress waves may interact with each
other and every inhomogeniety that they pass across, including, but not
limited to, specimen geometry, free surfaces, other cracks, grain boundaries,
other phases, voids and pores, inclusions, and smaller defects [29-41].
Elastic waves can be reflected, refracted, echoed, attenuated, diffracted,
transmitted and transformed into components of other wave types [41], always
seeking to minimize the specimen's potential energy.

Frequency attenuation and scattering has been shown to be sensitive to
the primary constituents of the microstructure, i.e. grain boundaries, second
phases, voids and pores [35]. Evans et al. showed that ultrasonic attenuation
in ceramics increases nearly linearly with frequency. Attenuations of 1 to 20
dB/cm are typical for MgO, RBSN, PZT and ZnS in the low MHz range [35].

For sintered and hot pressed SiC and hot pressed Si_3N_4 (α and β),
attenuations of 10 to 50 dB/cm were found for frequencies in the 100 to 400
MHz range [35]. An elastic stress wave is attenuated most when its

wavelength is on the order of the size of the scattering center or scattering center separation distance [35].

As a given stress wave encounters a scattering center, it may emerge as a wave or collection of wave components of totally diverse character [41]. This effect means that the interpretation of AE signatures is very difficult. The AE analysis software cannot recognize and differentiate the different waves that stimulate the piezoelectric transducer. The system also cannot distinguish an echo from the original pulse. Thus the 'envelope' that the software responds to can be modified by echo pulses. Echo pulses are attenuated with respect to the original pulse [31], but transmission distances vary with the location of the site of the reflection. The presence of echoes may inflate the number of counts received, potentially leading to an overestimation of the extent of microcracking. Also, a finite dead-time for 'envelope reset' exists between the times the system is able to receive a pulse. Dead time may reduce the number of counts recieved, but this does not necessarily nullify the effects of pulse reflection.

Being aware of this potential misinformation is only the first step to realizing an accurate interpretation of the crack/AE relation. Time of flight data may be obtained from a transducer array to provide a distribution of cracking activity across the specimen. Still, the echo problem is present and must be treated with care. Echoes are attenuated to some degree as shown by Evans [35], but the attenuation may not be enough to allow us to set an amplitude threshold above the echo, and below the original A-E burst. The difficulty comes when trying to distinguish between a nearby echo and a distant pulse due to new damage. Experimental procedure will determine the viability of the use of a threshold as a screen to separate new damage from frictional emission. The business of interpretation of AE signals is certainly challenging, but is still of worthwhile interest and pursuit.

2.2.2. Acoustic emission parameters.

There are several approaches to analyzing acoustic signals. In the literature, the AE count rate is the most frequently used method. The AE count rate is measured by the number of times the RMS voltage amplitude, or intensity, crosses a voltage threshold. The threshold is set somewhat subjectively or empirically by the researcher.

The voltage threshold is usually chosen as low as possible, to give the highest degree of sensitivity without significantly compromising the signal-to-noise ratio. A low amplitude threshold reads more of the lower intensity AE events. If a certain level and higher AE activity is of interest, the threshold setting may be adjusted to screen out the lower intensity events if they detract from the desired data, as may be the case for frictional AE.

To avoid background noise, some threshold above that background noise must be selected, but the threshold must remain low enough to not exclude the expected AE signal [29-40]. Clearly, the choice of threshold level determines the number of counts received during the AE burst envelope (Figure 6). Background and machine noise must be known to enable one to know with confidence, that the data being received is an actual specimen signal and not extraneous acoustic activity. Researchers that report system gain have overall system amplification between 80 and 130 dB [31, 33, 34, 45]. Often the equipment used and control parameters and settings are not specified in detail in the literature.

The exclusion of non-data is not as difficult as one may expect. Machine noise is usually in the low kilohertz range [29]. Cracking in ceramics is usually spread across the zero to 10 MHz range [32], with significant components in the megahertz range (Figure 7).

The time resolution required for our AE equipment is on the order of 0.1 microsecond [42]. In 0.1 microsecond, only one event (though one is
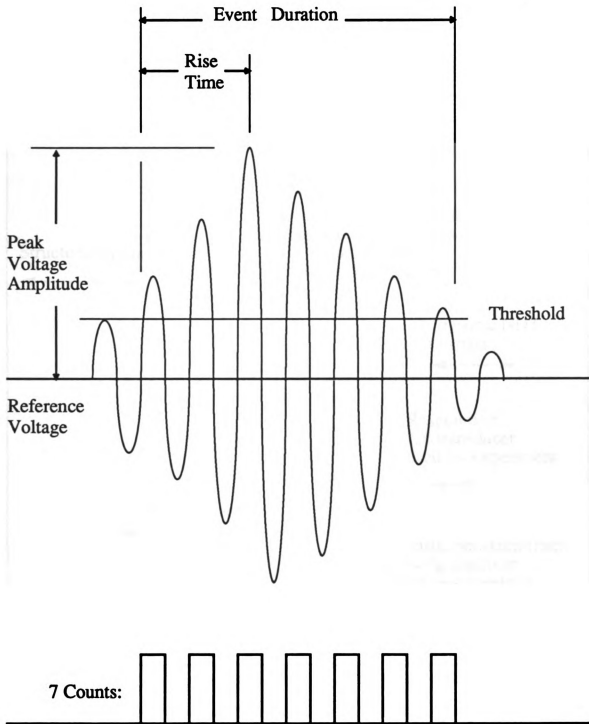
Figure 6. Definitions for acoustic emission elastic stress wave parameters.

Mechanical failures

⟵——————⟶

e.g. damaged bearings,
leaks in pipelines,
seismic disturbances

Structural dynamics

⟵——————⟶

Ultrasonic NDT
of metals

⟵——⟶

Response of
AE transducer
used for experiment

⟵—⟶

Rotor dynamics

⟵——————⟶

Acoustic emission from
growing cracks in
metals and ceramics

⟵——————⟶

| 0.1 | 1.0 | 10 | 100 | 1 K | 10 K | 100 K | 1 M | 10 M |
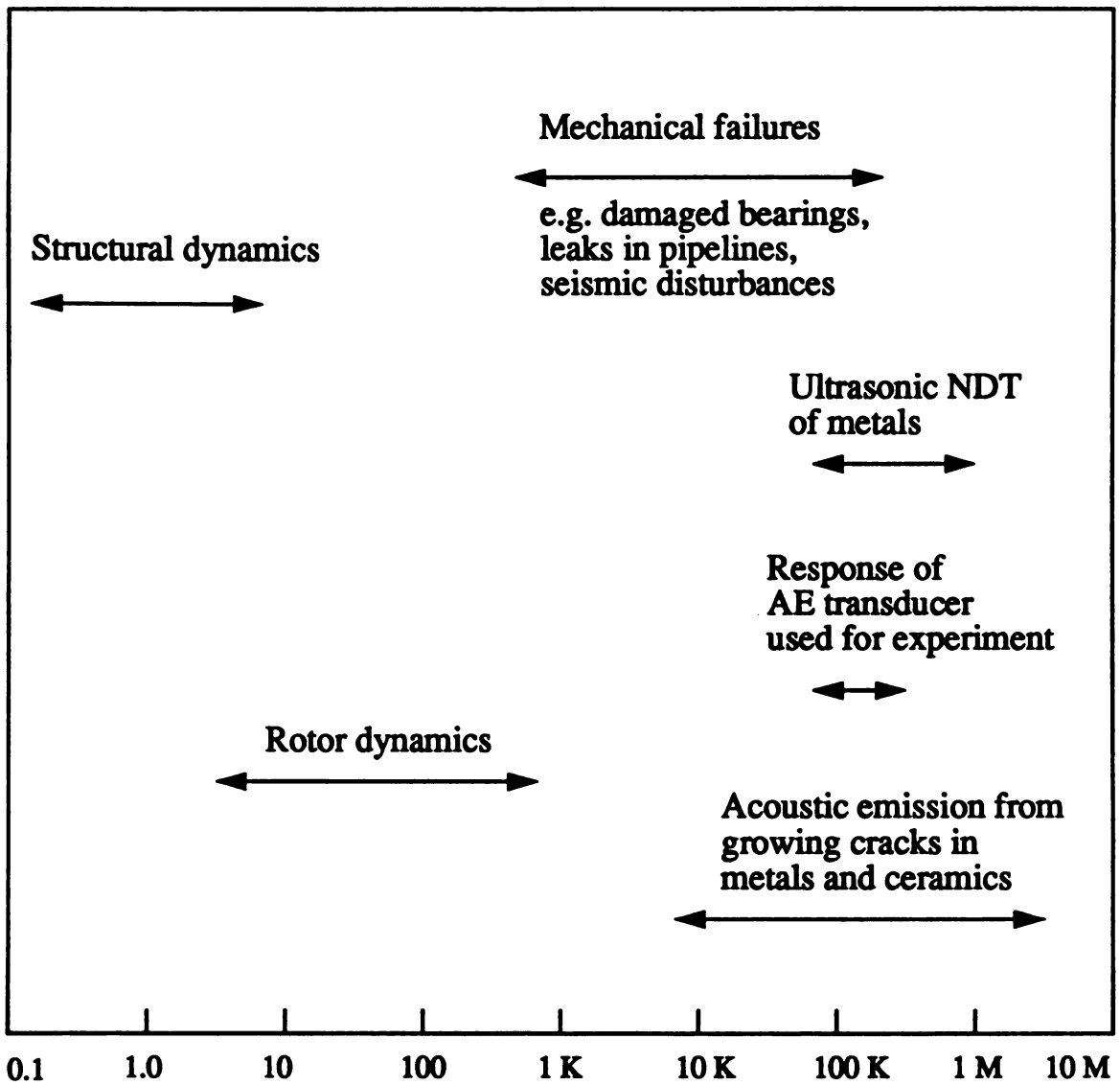
Figure 7. Acoustic frequency ranges for several mechanical sources.

unlikely), or thousands of events may occur. Continuous emission can keep an envelope open due to reflections and echoes.

Awerbuch et.al. presented a method of acoustic emission analysis useful for correlating certain aspects of the AE with other measures of damage [59-61]. The intensity of the AE signal, as measured by counts, rise time or duration, may be screened by setting a lower threshold of counts, rise time or duration. The AE events exceeding the threshold are then analyzed. By knowing the number of fatigue cycles at which the AE was taken, we may plot the AE parameter on the ordinate and the number of fatigue cycles on the abcissa. The choice of an AE threshold depends on the damage that the specimen has undergone.

2.2.3.   Crack growth and acoustic emission rate relations.

Researchers report conflicting relations between emission rate and applied stress intensity about the crack tip. The relation widely used as a starting point for AE rate equations is [30, 31]

$$dN/dt \sim cK_I^n \tag{11}$$

where

$$c = \text{constant scaling factor}$$
$$K_I = \text{stress intensity at the crack tip}$$
$$n = \text{stress intensity exponent, varies with material.}$$

The stress intensity exponent, n, can be as small as 2 or 5 for alumina, and as large as 50 to 100 for the tougher ceramics such as SiC and Si_3N_4.

This range is attributable to a fundamental difference in the materials, and is somewhat dependent on temperature and testing technique.

Crack growth rate may be approximated as

$$da / dt = c K_I^n \tag{12}$$

where

$$c = \text{constant scaling factor}$$
$$K_I = \text{stress intensity for mode I opening}$$
$$n = \text{stress intensity exponent.}$$

The stress intensity exponent, n, has also been shown to vary with temperature from 5 to 10 at room temperature, up to about 100 at 1300 °C for Lucalox [30]. To a first approximation, AE is related to crack growth by combining Equations 11 and 12, which yields [30]

$$dN / da \sim q K_I^2 \tag{13}$$

where

$$dN / da = \text{acoustic emission rate per unit crack area}$$
$$K_I = \text{stress intensity for mode I opening}$$
$$q = \text{microcrack density.}$$

Evans and Linzer [31] develop an AE rate relation for slow crack growth

$$\log (dN / dt) = (m - 1) \log \sigma_a + (1 - m/r) \log \sigma + D' \tag{14}$$

where

dN/dt = AE rate in counts per unit time

m = particle strength distribution parameter

r = slow crack growth parameter

σ_a = applied stress

σ = stress rate

D' = fracture site availability parameter.

The real time sequence of the acoustic emission begins when the stress intensity exceeds a critical local threshold, advancing the crack. The elastic strain energy stored in the crack tip zone then creates new surfaces, generating elastic lattice vibrations as the crack front advances. The amount of strain energy consumed by cracking has been modeled as [31]

$$U = [(\pi\sigma^2 a^2 l) / E] + U_o \qquad (15)$$

where

U_o = strain energy of the uncracked body

σ = stress on body

a = crack surface created

l = length of crack

E = Young's modulus of body.

The crack front advances under a far field tensile stress at an exponentially decreasing rate [31, 33-36]. Once sufficient strain energy has

been released, the crack tip process zone is able to elastically, and to a very small degree plastically arrest the crack front. Acoustic emission is generated during the cracking and for a time afterward as the crack faces vibrate. The generation of AE by crack face vibration not only applies to slow crack growth, but also for cyclic or rapidly applied loads. In most ceramics there is very little or no microplastic deformation, therefore, cracking relieves much of the stress. Toughening mechanisms, such as crack branching and crack tip shielding, dissipate the strain energy with much less macrocracking [14, 31].

The acoustic emission associated with an event is proportional to the strain energy released during that event [31]. Evans and Linzer developed a relation based on strain energy in which AE count rate depends principally on crack velocity, and is relatively insensitive to stress intensity or crack size [31]

$$dN/dt \approx 3 \times 10^5 \, v \log(4 \times 10^{-5} \, K_I \, \sqrt{1/k}) \qquad (16)$$

where

$$
\begin{aligned}
dN/dt &= \text{AE rate} \\
v &= \text{crack front velocity} \\
l &= \text{length of crack front} \\
k &= \text{crack front participation ratio, i.e. the number of active} \\
&\quad \text{cracks with respect to the total number of cracks.}
\end{aligned}
$$

These relations must be empirically calibrated. In practice, internal microcracks are not detectable during measurement, nor is their number density or size known. We may be able to detect the acoustic emission and determine the changes in internal friction and Young's modulus, with perhaps a correlation between them without speaking directly to crack growth rate. Crack growth rate (using a product of number and size) can be approximated via a derived acoustic emission rate.

2.3.   Fatigue in unidirectionally reinforced glass fiber - epoxy matrix composites.

In-service flexural fatigue damage is common for engineered composite structures. Flexural fatigue in glass fiber - epoxy matrix composites occurs by the incremental accumulation of cracking damage under a random or (usually) cyclic load profile. Fatigue damage results from three distinct mechanisms which compete with one another for the demise of the specimen [47]. The damage mechanisms are a function of the material properties (i.e. stiffness, elastic modulus etc.), as well as fiber volume fraction, specimen geometry, interfacial strength, test environment and pre-test treatments.

Mechanical damage mechanisms are (1) flexural tensile failure, which causes transverse matrix cracking with fiber pullout and bridging, (2) flexural compressive failure, which causes fiber buckling and (3) longitudinal matrix splitting on the compressive side and interlaminar shear failure, in which the fiber and matrix debond along the specimen's transverse-axial midplane.

2.3.1.   Stresses in the four point bend test.

In four point bend loading, the specimen experiences a maximum flexural tensile stress on the outer face of curvature and maximum flexural compressive stress on the inner face of curvature, between the short span of load - support pins. The maximum shear stress occurs along the mid-plane of the specimen between the outer and inner load-support pins (Figure 4, page 11) [23-25, 47-49].

In the load span, the maximum flexural stress is given by [47-49]

$$\sigma_{max} = (3PS) / (4bd^2) \qquad (17)$$

28

where, for Equations 17, 18 and 19

σ_{max} = maximum flexural tensile or compressive stress (Pa)

τ_{max} = maximum flexural shear stress (Pa)

P = total load applied (N)

S = span between load pins (m)

b = width of test specimen (m)

d = thickness (height) of test specimen (m).

Maximum shear stress is given by [47-49]

$$\tau_{max} = (3P)/(4bd). \qquad (18)$$

Equations 17 and 18 can be combined to yield [47-49]

$$\sigma_{max} = (4S/d)\,\tau_{max}. \qquad (19)$$

All three failure mechanisms operate on the test specimen simultaneously (Equation 19). It is important to emphasize that different locations on the specimen experience the three different maximum stresses. A test specimen with a 4S / d value less than σ_i / τ_i favors shear failure and is known as the 'short - beam' test [47, 48].

The event of fracture may be conceptualized as failure of the weakest link in a chain [48]. Therefore, fabrication parameters may be tailored to further

improve the performance of the composite. Also, the span to thickness ratio may be adjusted by varying the test fixture span to give either the flexural or the short beam test.

2.3.2.   Fatigue damage modes.

Shih and Ebert note that increasing the composite's fiber volume fraction causes the failure mode to shift from flexural to shear. Both flexural and shear strengths shift to a condition which encourages failure by shear mode [47-49]. The shift of damage modes from flexural to shear occurs for three reasons: (1) the availability of more fibers to bear flexural stress, reducing the likelihood of flexural failure, (2) more fiber / matrix interfaces and (3) less matrix material present.

Shih and Ebert tested the effect of interfacial strength in several combinations of fiber / matrix and coupling agents [47]. The fiber / matrix interface was degraded by boiling the specimen in water for various time durations, then breaking the specimen without prior fatiguing [47]. Modifying the interface 'quality', changed the failure mode from purely flexural tensile failure in the undegraded condition, to flexural compressive failure in the partially degraded condition. Shear failure occured for the most degraded - longest boiling time exposure (Figure 8) [47].

In the flexural tensile failure mode, fiber ridging (not bridging of crack wake) occured prior to matrix cracking. Fiber ridging occured on the tensile face of flexure, as the matrix underwent Poisson contraction trying to pull in between the fibers. Ridging gives the fibers the appearance of bulging out from the surface of the specimen, under a thin skin of matrix material. Fiber ridging is attributed to relaxation of residual stresses in the matrix material after fiber / matrix interface debonding [47]. Fiber ridging was independent of the type of coupling agent (fiber sizing) used [47], as long as failure occured in

31
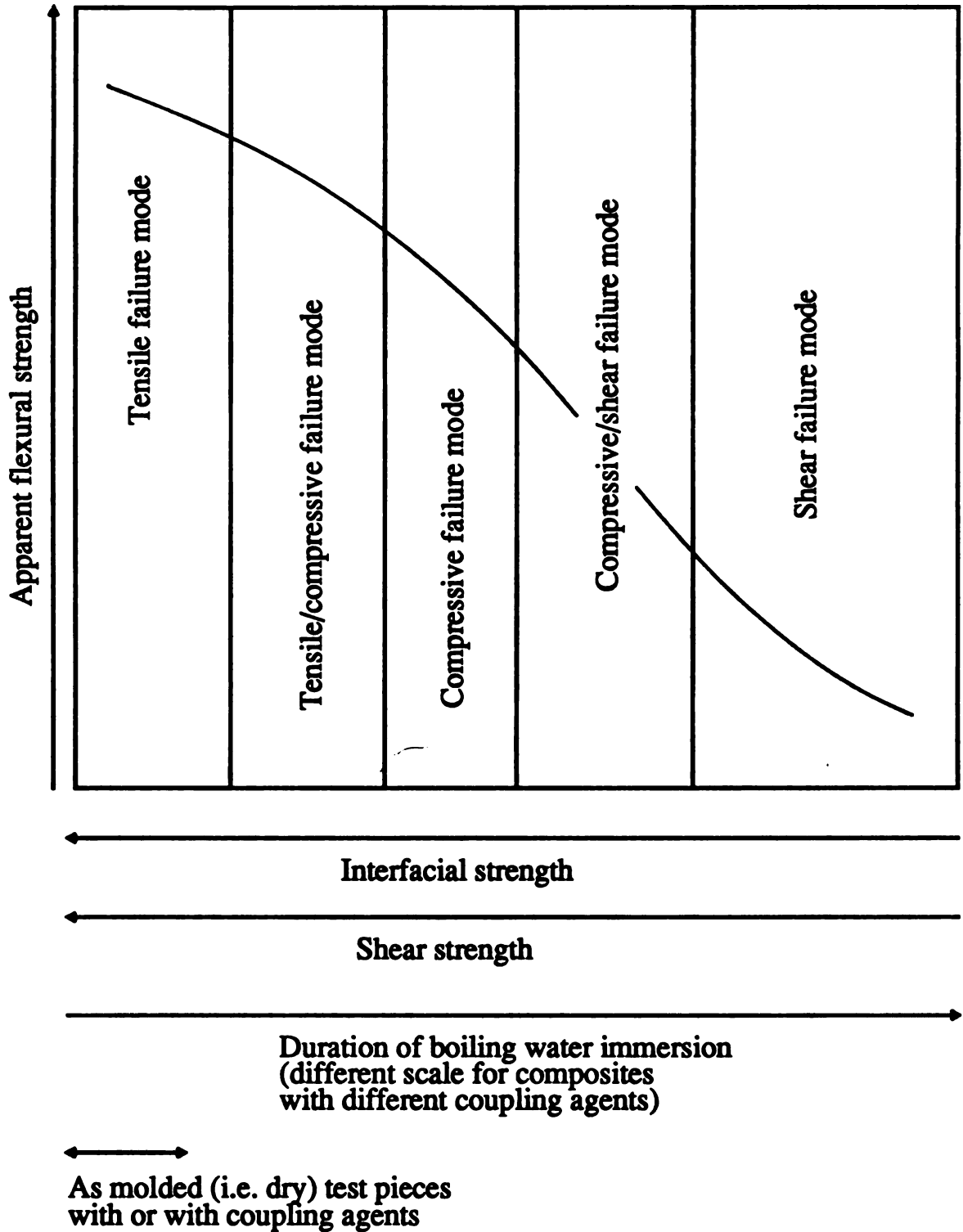
Figure 8. Transition of failure modes as a function of interface condition for GFRP composites under four point bending [47].

the flexural tensile mode. Failure modes were observed in post test optical and scanning electron micrographs.

In addition to fiber ridging, as the load is increased, transverse matrix cracks formed between two or more fibers at a time. The transverse matrix cracks linked up via short longitudinal cracks along the fiber / matrix interface, as observed in scanning electron micrographs [47]. As the loading proceeded, some fibers pulled out and were broken. The remaining nearby unbroken fibers carried the load until they in turn were broken. Eventually, the matrix and all the fibers were fractured. Under flexural tensile failure, fiber / matrix bond strength is critical. Higher bond strength reduces fiber ridging, but enables the matrix crack to penetrate the fiber ahead of the advancing crack tip.

In the flexural compressive failure mode, similar fiber ridging occured along with micro-buckling of the fibers. Shih and Ebert observed matrix spalling over the ridged fibers, indicating fiber / matrix debonding, but reported no matrix microcracking in the vicinity [47]. The failure mode was also independent of the type of fiber sizing agent used. As seen in post test S.E.M. micrographs, microbuckled fibers remained buckled after load relaxation, indicating a permanent displacement between fiber plies [47]. Permanent buckling of a fiber implies that the fiber has been partially pulled out, and resisted being forced back into its matrix hole upon stress relaxation. Again, a stronger interfacial bond reduces micro buckling and fiber ridging, but with the same tradeoff as for flexural tension.

In the shear failure mode, the shear crack propagates in a plane normal to the applied force, splitting the composite through its mid - plane. A strong interface increases shear strength [47], which is characterized by a large proportion of matrix material remaining bonded to the fibers [44]. These markings are referred to as 'hackle' marks [47, 50, 51].

Shih and Ebert found one combination of fiber / matrix and coupling

agent that suffered very little interface degredation in boiling water. This specimen was an Owens - Corning Fiberglas Corp. E - glass fiber and Ciba - Geigy XU235 epoxy matrix with XU205 aromatic diamine hardener in a weight ratio of 100:52, and coupling agent or fiber sizing AAPS (Dow - Corning silane Z-6020) [47].

Fiber pullout and bridging increases interlaminar fracture toughness as delamination grows. Sufficient fiber bridging can create a 'tied zone' [51], which increases fracture toughness and critical load. The tied zone is created when a shear or interlaminar crack propagates through the matrix and opposite ends of a fiber (or group of fibers) remain embedded in opposing faces of the crack.

Fiber nesting occurs when fibers are unevenly distributed throughout the matrix, with clumps of fibers that have very little matrix material within the clump. Fiber nesting occurs routinely in unidirectional layups in which fibers migrate in the autoclave temperature - pressure cycle [52]. Fiber nesting can increase crack growth resistance [50]. Migration of the fibers during autoclaving often twists the fiber bundle, such that the ends of some fibers end up on opposite sides of the bundle.

Shear cracks do not propagate exactly down the center of the specimen. Thus, the fracture surface is far from a perfect plane [47, 48, 54]. The instant at which fiber bridging initiates can vary. Crack bridging by fibers may not occur at all or bridging may initiate at the same instant the crack begins to propagate [51]. Single fibers are usually broken, whereas bundles of fibers tend to share and bear the stress and often peel out from the opposing crack faces, thus creating the fiber bridged 'tied zone'.

Fractography indicates the complex nature of failure modes of unidirectionally reinforced glass fiber/epoxy matrix composites under mode I loading [47, 48, 51, 54]. Smooth and hackled grooves can show the variation of interface bond strength and/or failure mode. The hackled grooves

34

suggest a strong interfacial bond and/or the stripping of the exposed fiber after delamination. The smooth grooves suggest either low interfacial strength and/or fiber pullout ahead of the crack front [47, 48, 51].

The 'tied zone' increases fracture energy. Under constant amplitude cyclic displacement the crack growth rate decreases, due to a load reduction with each increment in damage. However, the crack growth rate increases under constant amplitude cyclic load [51], since the same load is applied with each load cycle.

Hwang and Han [51] investigated fatigue threshold values of strain energy release rates and the effect of overloads by load reduction method. They reported that the delamination growth rate returns to the pre-overload values after the overload [51]. Mall et al. showed that the strain energy release rate range (ΔG_i) was the most important parameter for cyclic debonding [53]. When no fiber bridging occured, the Paris' power law was suggested to be a useful starting point in predicting the cyclic fatigue crack propagation [51-53].

2.3.3. Fatigue life relations.

Hwang and Han [51] studied interlaminar fracture in a glass - epoxy composite. A width tapered double cantilever beam (WTDCB) configuration was used for two advantages over the plain DCB: (1) constant ΔG_i, strain energy release rate being easily controlled by load, and (2) crack growth rate, da / dN remains constant within a determined constant strain energy release rate range [51].

To predict fatigue crack growth accompanied by fiber bridging, Hwang and Han [51] modified Paris' fatigue power law for isotropic materials such that

$$da / dN = B \, \Delta G^n_I \tag{20}$$

and $\qquad \Delta G_I = G_{Imax} - G_{Imin} \tag{21}$

where

da / dN =   crack growth rate

B, n =   material constants

ΔG_I =   applied cyclic strain energy release rate range,

            under mode I loading

N =   number of loading cycles.

For the WTDCB specimen under constant amplitude cyclic load, the cyclic strain energy release rate range is given by [51]

$$\Delta G_I = q \, (P^2_{max} - P^2_{min}) \tag{22}$$

where

$\qquad q = 12 \, k^2 / E^b_x \, h^3$ (Beam Method) $\tag{23.a}$

where

$\qquad q = k \, dC / d(a^2)$ (Compliance Method) $\tag{23.b}$

where

k =   taper of WTDCB (unitless)

E^b_x =   effective bending modulus of the beam

            along the x - axis (MPa)

h = height (thickness) of specimen (m)

C = compliance of specimen

a = crack length (m).

Hwang and Han conclude that their experimental data agrees with the normalization of Paris' power law [51], so that

$$da / dN = B (\Delta G_I/G_{RB}(a))^n \tag{24}$$

where

a = crack length (m)

G_{RB} = crack growth resistance due to fiber bridging.

For the WTDCB specimen under constant amplitude cyclic load range, the crack growth resistance due to fiber bridging can be written in terms of crack length, 'a' [51], such that

$$G_{RB} = q[P_{CI} + \alpha(\Delta A)^B]^2$$

$$= q[P_{CI} + \alpha(\{a^2-a_0^2\} / 2k)B]^2 \tag{25}$$

where

q = given in Equations 23.a and b

P_{CI} = initial critical load (not affected by fiber bridging)

ΔA = increase in fracture area, from geometry of WTDCB specimen

$$\alpha, \beta \quad = \quad \text{material constants, found to be 3270 and 0.442,}$$

$$\text{respectively, for 3-M type 1003 GFRP}$$

$$\Delta A \quad = \quad (1 / 2k)(a^2 - a_0^2)$$

$$= \quad (1 / 2k)(\Delta a^2 + 2a_0 \Delta a). \tag{26}$$

Now, the increase in crack growth resistance may be written

$$\Delta G_{RB} = G_{RB} - G_{IC} \tag{27}$$

where ΔG_{RB} and G_{RB} are defined as above, and

$$G_{IC} \quad = \quad \text{initial fracture matrix energy, not}$$

$$\text{affected by fiber bridging.}$$

Integrating Equation 24 from initial crack length a_1 to a later crack length a_2 gives [51]

$$\Delta N = N_2 - N_1 = 1 / B \int_{a_1}^{a_2} (G_{RB} / \Delta G_{RB})^n \, da. \tag{28}$$

Substituting Equations 22 and 25 into 28 gives the following fatigue life expression for the WTDCB test specimen [51]

$$\Delta N = N_2 - N_1 = 1/B \int_{a_1}^{a_2} \{[P_{CI} + \alpha((a^2 - a_0^2)/2k)^\beta]^2 / (P^2_{max} - P^2_{min})\}^n \ da. \tag{29}$$

Equation 29 can be evaluated numerically. Hwang and Han note that Equation 29 gives the same result whether the beam or the compliance method has been used to calculate the strain energy release rate [51].

A least squares fit of fatigue data for a glass fiber/epoxy composite to Equation 24 yielded [51]

$$da/dN = 3.59 \times 10^{-5} (\Delta G_I / G_{RB})^{13.5}. \tag{30}$$

2.3.4.   Fatigue life modulus concepts.

Fatigue life prediction is further explored by Hwang and Han with the introduction of a concept they call 'fatigue modulus' [51]. Experimental fatigue data and fatigue life prediction are sometimes in good agreement for models such as the S -N curve [55], the empirical Basquin's power law relation [55], and the Coffin-Manson relation [55]. However, many material characteristics such as crack length and number density, residual strength, strain, elastic modulus, compliance and size of the fiber-bridged zone change over the course of the fatigue life of the specimen. More research is necessary to understand and better predict fatigue behavior of composites.

2.3.4.a.   Hwang and Han fatigue modulus.

Hwang and Han define an overall fatigue modulus as the applied stress divided by the overall strain at 'n' fatigue cycles [55]

$$F(n,r) \ = \ \sigma_a / \varepsilon(n) \ = \ \sigma_u \left(r / \varepsilon(n) \right) \tag{31}$$

where

$F(n,r)$ = fatigue modulus at n^{th} loading cycle

$\varepsilon(n)$ = overall strain at n^{th} loading cycle

σ_a = applied stress

r = ratio of applied stress (σ_a) to ultimate strength (σ_u)

i.e. $r = \sigma_a / \sigma_u$.

Appropriate boundary conditions are

$$F(0,r) \ = \ F_0 \sim E_0 \tag{32.a}$$

where

E_0 = Young's modulus of the undamaged specimen

and $\quad F(N,r) \ = \ F_f.$ $\tag{32.b}$

According to the definition of the overall fatigue modulus, $F(N, r)$ is equal to the elastic modulus on the first cycle, and the fatigue modulus at failure (F_f) is the value at N, the number of cycles to failure (Equation 32.b) [55]. This approach requires that each period of the applied stress is maintained at a constant maximum amplitude value, therefore, the fatigue

modulus is not a function of loading stress, but of loading cycle only.

The change in fatigue modulus as the specimen's life proceeds is given by [55]

$$dF/dN = -Acn^{c-1} \tag{33}$$

where

$$A, c = \text{experimentally determined material constants}$$
$$A \text{ is on the order of Young's modulus } / 10.33,$$
$$\text{and } c \text{ is about } 0.15.$$

Integrating Equation 20 with respect to n, number of fatigue cycles, from n_1 to n_2, gives

$$\Delta F = F(n1) - F(n2) = -A(n^c_2 - n^c_1). \tag{34}$$

Inserting $n_2 = n$ and $n_1 = 0$ into Equation 34, we have [55]

$$F(n) - F(0) = -An^c. \tag{35}$$

At failure, where n = N, we have [55]

$$F_f - F_o = -AN^c. \tag{36}$$

Therefore, using the fatigue modulus concept, we can find N, the number of cycles to failure, N, is [55]

$$N = [\,B\,(1 - F_f/F_o)\,]^{1/c} \qquad (37.a)$$

where

$$B = F_o / A. \qquad (37.b)$$

Using the linear stress / strain equation [55]

$$\sigma_a = F_{f,a}\,\varepsilon_{f,a} \qquad (38)$$

where

σ_a = applied stress

$F_{f,a}$ = fatigue modulus at failure, under σ_a

$\varepsilon_{f,a}$ = strain at failure, under σ_a

it follows that

$$F_{f,a}/F_o = \sigma_a/\sigma_u = r. \qquad (39)$$

Inserting Equation 39 into Equation 37.a, we have [55]

$$N = [\,B\,(1 - r)\,]^{1/c}. \qquad (40)$$

Equation 40 now may be used to predict fatigue life as long as applied stress levels, mode of stress and the material constants are known

(Equations 37.b and 31 respectively).

Equation 40 is in much better agreement with Hwang and Han's experimental data than either (a) the S - N curve or (b) Basquin's relation, which are given by

(a) S - N curve [55]

$$r = k \log N + d \tag{41}$$

where

r = applied stress level

N = number of cycles to failure

k = slope of S - N curve in r - log N space

d = r intercept of S - N curve in r - log N space.

(b) Basquin's relation [55]

$$\sigma_a = \sigma_f (2N)^g \tag{42}$$

where

σ_a = applied stress

$2N$ = stress reversals to failure (1 cycle = 2 reversals)

σ_f = fatigue strength coefficient

g = fatigue strength exponent (Basquin's exponent [55]).

2.3.4.b.   Secant modulus concepts.

Hahn and Tsai introduced a secant (elastic) modulus [57], in which a line is drawn from the zero stress - strain point to the maximum stress - strain point (Figure 9), after 'n' load cycles. The primary loading, H(n), and secondary unloading, H'(n), secant elastic moduli are drawn for the nth loading cycle. Tangent elastic moduli are also illustrated.

Hwang and Han develop a geometric relation linking the four elastic moduli and the secant modulus [55]. Considering Figure 9, we can state the geometric relation

$$H(n) \ = \ E2(n) + t(n)[E1(n) - E2(n)] \qquad (43)$$

$$H'(n) \ = \ E'2(n) - t'(n)[E'(n) - E'2(n)] \qquad (44)$$

where

$$t(n) \ = \ AB' / AC', \quad 0 < t(n) < 1 \qquad (45)$$

$$t'(n) \ = \ D'E / C'E, \quad 0 < t'(n) < 1. \qquad (46)$$

Hwang and Han [55] describe a fatigue secant (elastic) modulus, in which the secant modulus is degraded until fracture occurs (Figure 10). Using Figure 10, the fatigue modulus may be written [55]

$$1 / F(n) = \ \Sigma \ [1 / H(k) - 1 / H'(k) + 1 / H(n) \qquad (47)$$

and

43
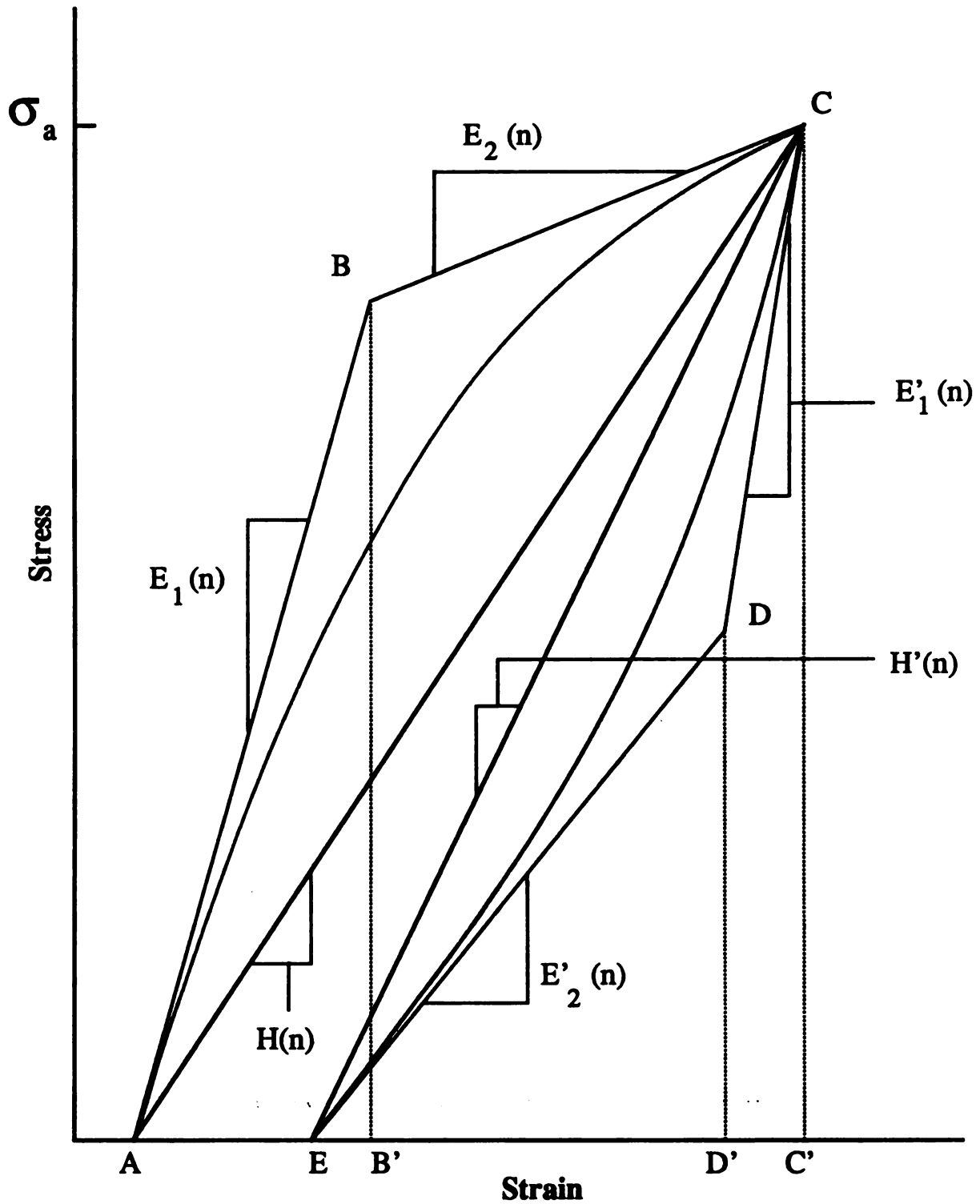
Figure 9. Schematic of Hahn and Tsai secant modulus during the nth fatigue load cycle [57].
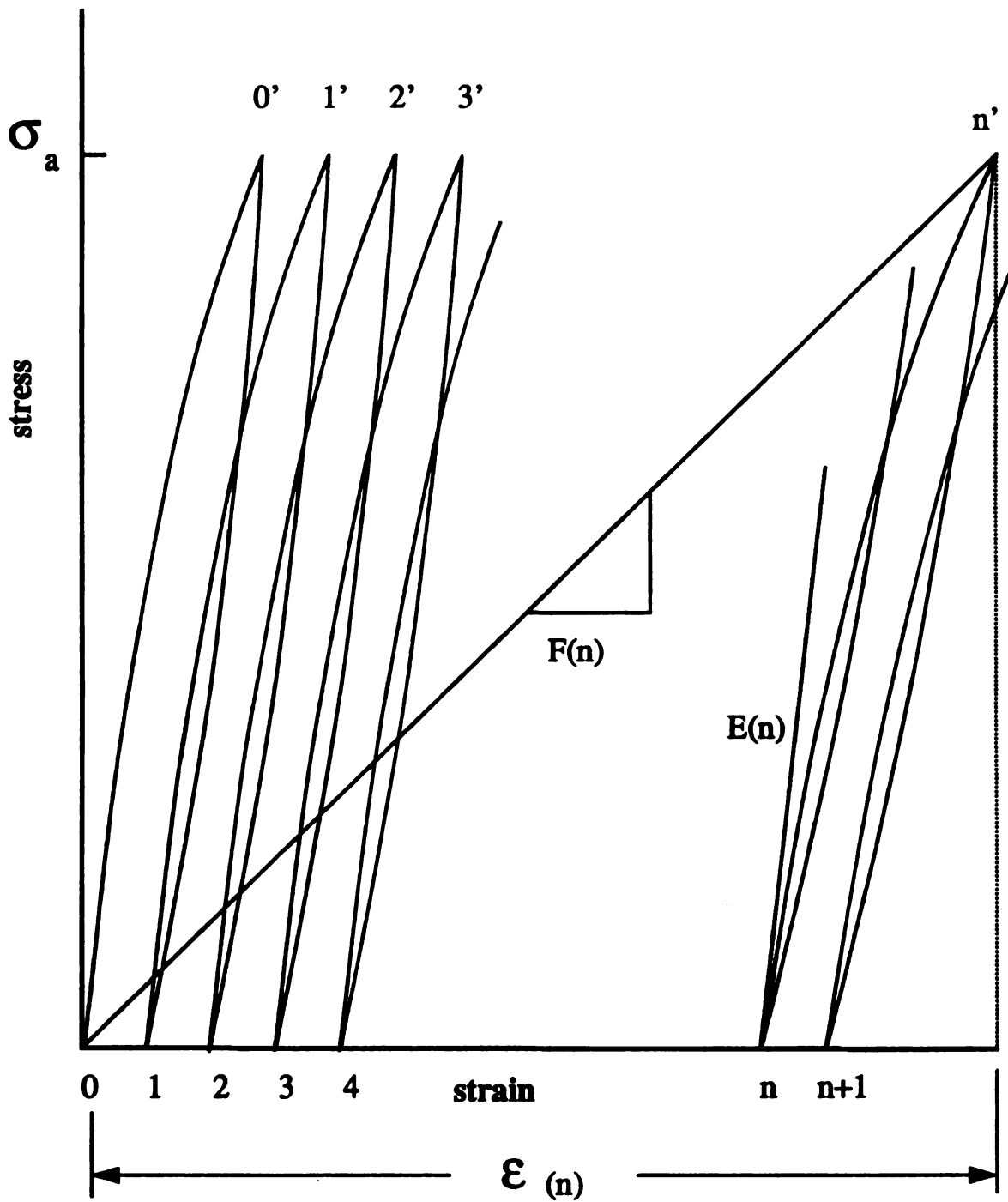
Figure 10. Hwang and Han fatigue secant modulus [55].

$$1 / F(n) - 1 / F(n - 1) = 1 / H(n) - 1 / H'(n - 1). \qquad (48)$$

The above relations for fatigue life and fatigue modulus apply to the unidirectional glass fiber reinforced epoxy matrix composite being used in this thesis.

The material used for this thesis is the same as that used by Hwang and Han [51], i.e. 3-M type 1003. See Appendix 6.A for 3-M composite type 1003 physical properties.

2.3.5. Acoustic emission in the fatigue of GFRP composites.

Fatigue induced acoustic emission in GFRP composites has been investigated by several research groups [6, 7, 59-65].

To further understand composite damage modes, it is essential to distinguish between the acoustic emissions of new damage (i.e. matrix cracking and splitting and fiber pullout and breakage) and the emission due to friction, rubbing and fretting between the newly created fracture surfaces [6, 7]. Results from other researchers [59, 60] indicate that substantial acoustic emission is generated by friction between fracture surfaces.

The methods and data presentation formats of Awerbuch et al. [59, 60] appear to be most informative. There is a similarity of equipment between Awerbuch's and MSU's MMM Department's Physical Acoustics Corporation AE analysis computer and the 3-M type 1003 GFRP test specimens. Awerbuch, with Ghaffari [59] and Eckles [60], discuss the acoustic emission fron unidirectionally reinforced graphite fiber / epoxy composites stressed in tension - tension fatigue loading, in which the ratio of minimum to maximum tensile load is 0.1 (i.e. R = 0.1). A substantial amount of acoustic emission is generated by friction between newly created internal crack surfaces, as made

evident by the continuous emission as the load is continuously increased and decreased [59, 60].

Frictionally generated acoustic emission often exceeds and masks emission due to new damage [59, 60]. Awerbuch et al. developed a methodology to discriminate friction generated emission from new damage emission by correlating AE event intensity parameters [59, 60].

The acoustic emission apparatus used by Awerbuch et al. [59, 60] consisted of a Physical Acoustics Corporation (PAC) AE computer model 3000/3004. System operating parameters were listed as: 150 KHz resonance transducers, model 1220A preamps with +40 dB fixed gain, system threshold of 0.1 volt, postamplifier gain of +20 dB and dead time of 1 msec [59].

Two transducers were used for event location determination. Post test spatial filtering analyzed only events within 20 to 80 percent of the gage length. Damage progression was also monitored by a 150X closed circuit television in real time. The specimen was X-rayed in transmission after each test sequence to determine the extent of cracking and splitting damage [59].

Awerbuch et al. [59-61] found that acoustic events that occur in the lower load range (e.g. 10 to 95 percent of σ_d) were primarily associated with interfacial crack friction. Do not confuse this with the quantitative damage measure of Q^{-1}. Events generated in the upper load range (e.g. 95 to 100 percent of σ_d) are primarily associated with new damage [59].

Although friction generated emission dominates the lower end of the load range, some new damage is occuring, albeit generally masked by the continuous frictional emission [59-61]. Conversely, at the high end of the load range, where new damage is expected to dominate, a large amount of frictional emission also occurs. The percentage of either kind of emission is difficult to estimate, due to the nature of the specimens. Some AE events can (and do) occur too rapidly for the PAC AE system to recognize and record.

However, the new damage can be indirectly observed by the increase in friction generated emission when the AE counts data from the lower load ranges is summed [59-60].

Awerbuch et al. [59-60], investigated a single damage mode, i.e. matrix splitting with very limited fiber breakage. Two distinct ranges of AE event intensities were observed. Lower intensity AE events were recorded across the entire load range. Only low intensity events were observed at the lower load ranges. With increasing load, the number of events with higher count rate and amplitude intensities increased [59-60].

Awerbuch et.al. [59-60] introduced the method of plotting AE event intensities as a function of load. Awerbuch et al. [59, 61] plotted events (ordinate) versus amplitude or duration (abscissa) as histograms, and amplitude or duration (ordinate) versus load (abscissa) as point plots. A load signal was fed to the PAC computer's parametric input as a DC voltage with a full scale range zero to +10 VDC.

The number of AE events versus amplitude histogram appeared bi-modal, implying that the lower amplitude group of events (centered at ~ 55 ± 5 dB) is primarily due to frictional emission. The higher amplitude group (centered at ~ 65 ± 5 dB) was assumed to be primarily due to new damage [59, 60].

Specific graphical filters and parameters can be applied to recorded AE data. Post test filtering can divide data on either side of a chosen threshold for any parameter felt to be helpful in descriminating new damage emission from frictional emission [59-60].

The accumulation of new damage has been shown to be a sporadic, seemingly random process [59-65], analogous to natural processes such as the initiation of corrosion sites in some metals [61]. The release of acoustic energy by the specimen also varies from cycle to cycle. A given specimen may be fatigued for several cycles without detectable AE, while large numbers of AE events may be observed during subsequent load cycles [61]. The

apparently random nature of acoustic emission indicates that the progression of damage is (macroscopically) a sporadic, random process.

As a specimen is fatigued, new damage accumulates rapidly at first. The damage tapers down to a moderate increase until the damage reaches a critical level. At the critical damage level, AE increases as catastrophic damage rapidly degrades the specimen [46, 59-61, 63]. The division of acoustic emission into three ranges (initial rapid accumulation, lower steady state accumulation and final rapid accumulation) suggests the operation of a three regime damage curve analogous to the creep damage curve in metals and some ceramics.

Damage saturation is found elsewhere in nature. Thermal shock damage in alumina saturates with thermal fatigue, with the damage measured as changes in elastic modulus and internal friction. When fatigued, certain metal alloys show a saturation of persistent slip bands of dislocations which accomodate plastic deformation induced by constant strain cycling.

Awerbuch et al. found that when sorted according to load range, AE data in the range of 0.95 to 1.0 of σ_{dmax} tends to a steady state emission rate. When the AE data, after sorting by load range, is screened off below a chosen amplitude threshold, the rate of accumulation of AE events is even lower. Awerbuch et. al terms that threshold as a 'friction emission threshold' or 'FRET' [59, 60].

In Awerbuch's experiment, the AE recorded in the lower range (below $0.95 \sigma_d$), rises quickly at the start of the fatigue test, then lessens in rate of increase only slightly as fatigue life progresses (as the number of loading cycles increases), remaining the dominant source of AE [59-61, 63]. This emission was largely attributed to frictional sources. Once frictional emission began, it accumulated continuously and at an increasing rate. Frictional emission (which encompasses crack surface rubbing, fretting, asperity contact

and debris pulverization) may be a continuous source, whereas new damage occurs only once. Awerbuch et al. [61] verified crack closure and simultaneous frictional emission during load cycling by observation in situ at 150 X magnification by closed circuit television.

Awerbuch [61] explained that the Kaiser effect [5], present during fatigue in GFRP composites, may provide insight regarding the initial rapid increase of AE events from new damage at the beginning of a test. This effect is likely due to a reduction in the rate of the creation of new damage [46].

The selection of the FRET level must consider AE event intensity parameters. Awerbuch et al. found that the intensities of events in the lower load range were generally characterized by less than 20 energy counts, less than 40 counts per event and less than 250 microseconds in duration [59]. These parameters vary with material, maximum stress applied, cycling frequency etc. and must be determined experimentally [59-61]. Elastic moduli of the constituents, volume fractions, stress intensity range, strain energy release rates and rate of deflection all affect the emission rate dN/ da (AE counts per increase in crack length or area) equations (Equations 20, 24 or 30).

The acoustic emission screening techniques [59-60] indicate a qualitative correlation between acoustic emission and crack damage initiation and progression. The link between AE and crack evolution allows the construction of derived damage curves, which are related to fatigue life [46-65].

2.3.6. Comparison of AE from three types of fiber reinforced epoxy composite materials.

Otsuka and Scarton [46] tested three fiber reinforced epoxy composites: (1) unidirectionally reinforced glass fiber epoxy, (2) chopped glass fiber mat epoxy and (3) unidirectional carbon fiber epoxy. A screw driven 'Shimazu'

general purpose testing machine was used, with the assumption that machine noise was 'inherently small'. Specimens were tested in two methods: three point bending and cantilever beam with a transverse saw cut at the depth of one lamina. Otsuka and Scarton plot amplitude versus number of AE events for all three specimens under each test combination. Although no clearly defined ranges appear in the amplitude distribution, the authors assume matrix crazing occurs at amplitudes up to about 33 dB, and that delamination and fiber breakage occurs with amplitudes greater than 33 dB [46]. The justification for this choice of threshold is the interpretation of a different test on the unidirectionally reinforced glass fiber epoxy composite, in which a local minimum of AE events appears at about 33 dB. Local peaks at about 24, 35 and 43 dB are assumed to result from the damage modes of matrix crazing, interply delamination and fiber breakage respectively.

A Kaiser effect experiment was performed by Otsuka and Scarton using carbon fiber-epoxy under three point bending. The specimen was loaded and relaxed, with loads of 245, 390, 490, 590 and 685 N. Virtually no AE was observed during the load relaxation, but there was an exponential increase in acoustic events during load-up, after the load exceeded the previous highest load. The result of their Kaiser effect test was used to justify the 24 dB peak's responsibility for matrix crazing, and not being a manifestation of machine noise.

2.4.   Mechanical fatigue in glass-ceramic composites.

Qualitative models exist for fatigue mechanisms for mechanical and thermomechanical fatigue in both monolithic ceramics and ceramic matrix composites [1, 6-8, 65-69]. The failure of brittle ceramics under cyclically varying compressive loads is of interest in a diverse number of engineering

applications [8, 65, 67, 70-85]. The driving force for the large-scale engineering research effort in fatigue is the improvement in mechanical properties and especially the reliability of ceramic structures. Reasonably accurate qualitative predictions of lifetimes, strengths, wear resistance and damage tolerance are said to be beyond the capabilities of current 'state of the art' research [65, 67, 74]. Production quality and repeatability for ceramic composite components must be significantly improved before accurate predictions of mechanical properties can be made [65, 67, 74]. Nonetheless, qualitative predictions are of great importance for making choices of materials with superior physical properties.

Before about 1985, mechanical fatigue in ceramics had been detected and acknowledged [9, 66] for only a few materials. Before 1985, mechanical fatigue effects were labeled as fatigue-like, and were usually attributed to environmentally assisted slow crack growth, also called stress corrosion cracking [6-9, 66, 67, 69, 71, 73, 75, 80]. Molecular water (atmospheric humidity) was named as the activating species for polycrystalline monolithic silicon nitride, soda-lime glass and electrical porcelain containing ~20 micron diameter dispersed quartz particles [7, 8-10].

Ewart and Suresh, in 1986, reported mechanical fatigue fracture at room temperature in chevron notched compression specimens of single phase polycrystalline alumina subjected to fully compressive loads [8]. Mode I fatigue crack growth occured without significant macroplasticity [8].

2.4.1.   Mechanical fatigue damage in ceramics.

Several researchers [1, 2, 4-7] suggest that the materials which exhibit the largest thermal-shock fatigue effect are those in which substantial preexistent or stress-induced microcracking is found [1, 2, 6, 7]. Kim et al. [3] and Case [81] however found that thermal shock fatigue occurs in polycrystalline

alumina, Macor, and other ceramic oxides. Their specimens were prepared and annealed to purposely minimize the number of preexistent microcracks.

A correlation between thermal-shock fatigue and microcracking exists and suggests the operation of microcrack based mechanisms. However, since thermal stress is a body force, and mechanical stress is externally applied, it is not clear how separate or separable are the roles of thermal [1, 2, 4, 6, 7, 11], mechanical [1, 2, 4, 6, 7] and environmental [6 , 71, 78] stresses. The separation of purely mechanical from thermomechanical fatigue effects is a basic step toward defining any certain mechanism for thermal-shock or mechanical fatigue [6, 7].

In the case of thermal shock fatigue, internal (body) stress is created during the quenching and heating of the specimen due to macroscopic thermal gradients imposed on the specimen. This situation arises due to thermal strains which are set up by the thermal gradient.

The thermal expansion relation,

$$\Delta L = \alpha\, L_0\, \Delta T \qquad (49)$$

describes the dilatational behavior of a material under a thermal gradient. The thermal expansion coefficient, of course, depends on direction within the material. Equation 49 applies to macroscopic stresses as well as microscopic stresses. Thus, thermomechanical fatigue may have additional mechanisms at work, beyond the macroscopic stresses of purely mechanical fatigue created by the thermal expansion gradient. However, thermal expansion mismatch and thermal expansion anisotropy are not necessary requirements for thermal shock fatigue [3, 81].

True fatigue crack propagation has been attributed to microcracking due to residual stresses arising from several sources. These sources include grain boundary misfit, crack wake asperity contact and other toughening

mechanisms such as crack tip interactions, crack bowing, phase transformations and crack deflection [8, 65, 68, 80, 81, 85].

Crack front extension can be arrested, restricted or diverted by various toughening mechanisms. These mechanisms include crack tip shielding and crack process zone micro-plasticity in some monolithic ceramics. For composites add the toughening mechanisims of matrix cracking, fiber debonding and fiber pullout and crack diversion around hard second phases or inclusions [6, 7, 74, 76, 78, 80, 81].

2.4.2.   Ceramic fatigue theory.

The macroscopic fatigue effect results from micro-scale mechanisms activated under cyclic loading [65-79]. For ceramics, the ultimate compressive fracture stress is often up to ten times that of the tensile ultimate fracture stress [8, 65, 70]. Ceramics still fail in time at loads substantially lower than their rated ultimate load bearing capabilities [8].

Many ceramic fatigue theories or models utilize two important aspects: (1) residual micro-stresses [6, 7, 68, 74, 76, 78] and (2) a mechanism to enable damage and microstructural changes to occur during the unloading part of the flexure cycle [6, 7, 9, 67, 80].

Significant residual stresses typically arise from grain orientation thermal expansion anisotropy. For ceramic composites, interphase thermal expansion mismatch is also present.

Lewis and Rice report that residual stresses may range as high as 1 to 2 GPa in alumina, and up to about 3 GPa in BN-containing particulate composites [6, 7]. However, Lewis and Rice [6, 7] do not specify how they measure the residual stresses. A propagating crack may interact with grain-size scale residual (built-in) stresses [6, 7, 65]. Grain boundary microcracking is frequently enabled by residual tensile stresses and low

fracture energy along grain boundaries [8, 65, 81].

Fatigue crack growth occurs during the load reversal transition from tension to compression and especially from compression to tension. During load reversal, the fracture mode changes from mode II or III during compression to mode I in tension [6, 7, 9, 68, 69, 71, 74, 78].

Lewis and Rice proposed that progressive slow crack growth occurs on each load cycle [6, 7]. Lewis and Rice examined Lucalox alumina, a glass-ceramic Pyroceram code number 9606 (Corning Glass Works, Corning N.Y.), and alumina- and mullite- BN composites.

Lewis and Rice's model [6, 7] requires: (1) the pre-existence of residual stresses and (2) a mechanism to allow damage to occur during both loading and unloading. Far-field stresses take advantage of the residual stresses to overcome the local fracture strength of grains or their boundaries. Incremental fracture of single grain boundaries leads to grain relaxation and misfit between adjacent and nearby grains during the flexural fatigue cycle. The microcracking thus relaxes and redistributes the stresses on the nearby grains and their boundaries. Lewis and Rice's [6, 7] self-feeding model describes a plausible mechanism for true cyclic fatigue damage during successive load cycles.

2.4.3. Fatigue models for ceramics and ceramic composites.

2.4.3.a. Microcracking model for polycrystalline ceramics.

A plausible tension-tension fatigue fracture process includes preexistent residual stresses that enable an applied far-field stress to advance a crack through a monolithic polycrystalline matrix (Figure 11) [6, 7]. Evans et al. describe a similar scenario [9, 65, 66], in which a polycrystalline ceramic accumulates microcrack damage during cyclic loading.
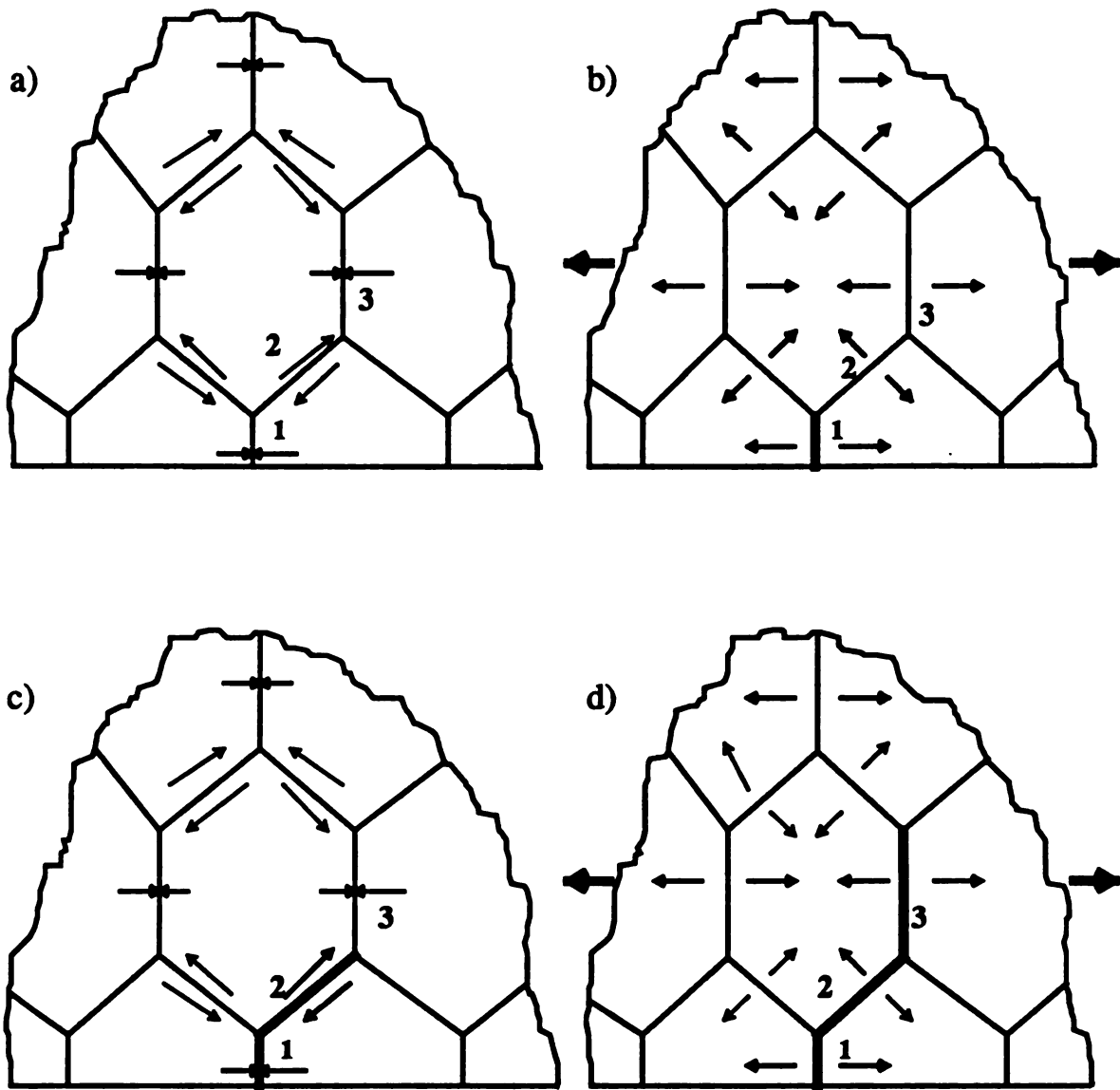
Figure 11. Schematic of fatigue in polycrystalline ceramic under tension-tension loading [6]. a) before loading, grain boundary one has residual compressive and shear stresses, grain boundary two has small residual tensile and large residual shear stress, b) on the first tensile load, grain boundary one is fractured, c) unloading increases shear stress on grain boundary two, fracturing it, d) reloading in tension extends fracture through grain boundary three by Mode I opening.

To model this cooperative grain boundary cracking process, a thought experiment is developed. Grain boundary 1 is initially assumed to have a residual compressive stress, and grain boundary 3 initially has small residual tension and a large residual shear stress (Figure 11.a). This scenario may be typical of a hypothetical polycrystalline ceramic material.

A far-field tensile stress (Figure 11.b) may produce a net tensile stress which fractures grain boundary 1. Propagation of the crack along grain boundary 2 may be suppressed due to the orientation of the boundary, superimposing little additional tensile stress while reducing the shear stress. Unloading then increases the shear stress at grain boundary 2 (Figure 11.c). The crack may then extend in Mode II opening (include Mode III opening for three dimensions). Reloading in tension subsequently extends the crack in Mode I along the next favorably oriented grain boundary (grain boundary 3 in Figure 11.d).

Subcritical crack growth due to grain-misfit-induced tensile stress occurs on each cycle until the crack grows to a critical length [6, 7]. When the crack tip stress intensity exceeds the local critical value, the crack then extends catastrophically on the next and last loading cycle [6-9, 65, 66, 69, 71, 80].

During a load cycle of compression-tension or compression-compression, a similar combination of residual and applied stresses can be envisioned (Figure 12). Here, grain boundary one has a residual compressive stress and grain boundaries two and three have small residual tensile and shear stresses (Figure 12.a). On the first compression cycle (Figure 12.b), the compressive stress on grain boundary one increases, causing no harm to that grain boundary. Grain boundaries two and three pop open by Mode II loading due to high shear stress, but do not propagate due to high compressive stresses at grain boundaries one, four and five. Upon unloading, the redistributed stress allows crack propagation along grain boundaries one and four or five by Mode I (tensile) loading (Figure 12.c).

a)
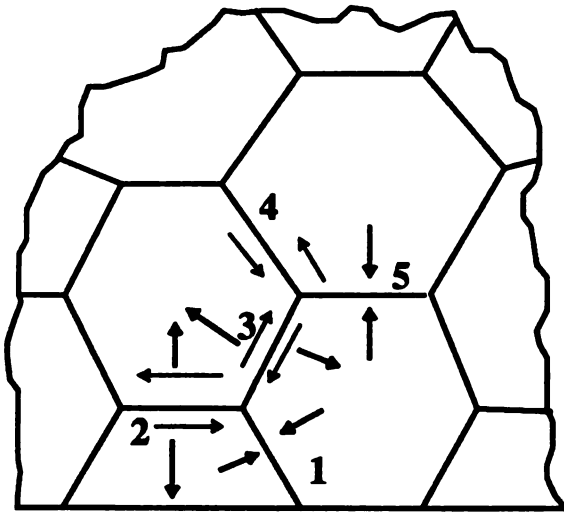
b)
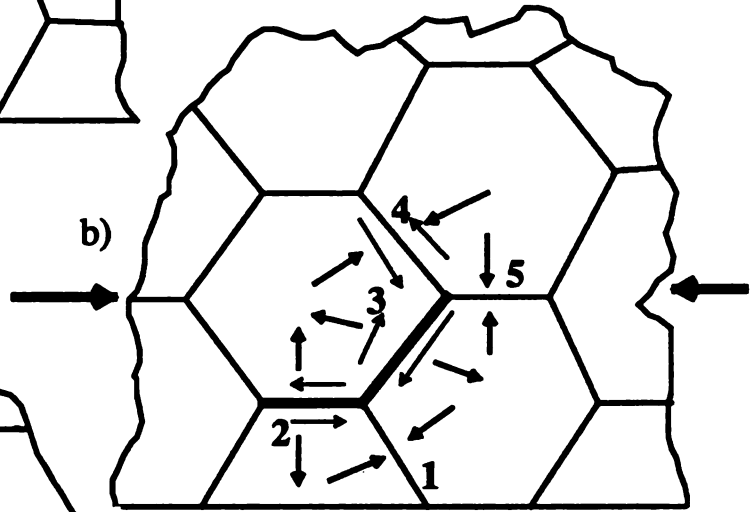
c)
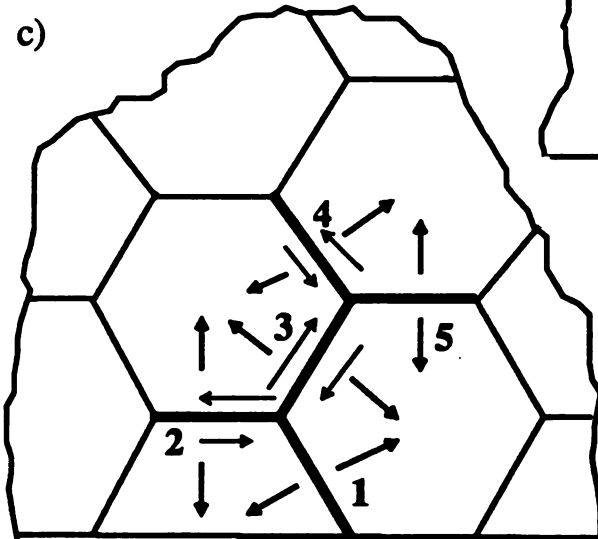
Figure 12. Schematic of fatigue in polycrystalline ceramic under
compression loading [7]. a) before loading, grain boundary one has a
residual compressive stress, and grain boundaries two and three both have
small residual tensile and shear stresses, b) on the first compressive load
cycle, grain boundaries two and three fracture in Mode II and are arrested
at grain boundaries one, four and five due to high compressive stresses on
those boundaries, c) on unloading, grain boundaries one, four and five pop
open under local tension.

The grains around the cracks now relax, assuming a position and shape that minimizes their own strain energy. This new condition of stress relaxation and shape change causes a local misfit of grains and induces additional 'residual' stresses upon nearby grain boundaries. With successive compression- relaxation or compression-tension cycles, the fatigue cracking proceeds until catastrophic failure occurs [6-9, 69, 71, 80].

2.4.3.b.   Fiber buckling model for ceramic composites.

For whisker and fiber reinforced ceramic matrix composites, residual stresses between the fibers and the matrix, while substantial, do not play a significant role in the fatigue of these materials [6, 7]. Lewis and Rice [6, 7] argue that these residual stresses are relatively minor when compared to other processes which occur in the fiber composite that can lead to fatigue. For example, a ten volume percent randomly oriented SiC fiber reinforced mullite-BN composite does not have a longer fatigue life than an unreinforced mullite-BN composite [7], although the SiC fiber reinforced composite is tougher.

The primary toughening mechanisms in reinforced ceramic fiber composites are matrix cracking, fiber debonding and fiber pullout [6, 7, 65, 80, 81]. The highest toughness possible requires fiber-matrix bond strength to be optimized as neither too strong, nor too weak, and with minimal compressive residual stresses on the fibers. Highest toughness may require crack branching, fiber pullout and crack diversion around fibers. High toughness implies the absorbtion of a large amount of energy during fracture with less loss of material, thus leading to a higher margin of damage tolerance. CMC's, in which the physical or chemical bond strength of the fiber to the matrix is high, typically have toughness values similar to that of the ceramic matrix [65]. Lewis and Rice's fiber pullout fatigue model depends heavily on

the non-reversibility of the matrix-cracking and fiber pullout, rather than on residual stress effects. For moderate stress levels, fiber damage during pullout may be a fatigue mechanism in itself [6, 7]. Fiber abrasion during pullout leads to weakening and eventual fiber fracture. As the fibers continue to fracture into smaller lengths, the lengths of the fibers still embedded in the matrix becomes less than the critical length for effective load transfer. The load bearing ability of the composite decreases as the length of the fibers is reduced to less than the critical length. The result is static fatigue, since the remaining fibers are stressed to higher levels [6, 7, 65, 80, 81].

Extensive matrix cracking and fiber pullout may lead to fiber buckling when the load is relaxed and the crack attempts to close (Figure 13) [7, 48, 79]. As the matrix cracks close, the pulled-out fibers are forced back into their respective holes in the matrix. Forcing the fiber back into its hole requires stresses higher than for pullout, since the relaxation of the fiber-matrix interfacial stresses create a substantial interference fit to overcome. In addition to the interference fit, debris in the fiber's hole and asperities along the fiber-matrix contact area substantially add to the force necessary to push the fiber back into its hole [6, 7]. If the pulled out length of a given fiber exceeds the critical length for buckling, given the particular stress geometries, the fiber will buckle and fracture.

A computer simulation by Lewis and Rice indicates that a 90 μm pullout length for a 25 μm diameter SiC fiber can be buckled by a crack closure force of 500 MPa [7]. Fiber buckling likely produces more damage than incremental grain boundary cracking with cyclic loading [7]. Rapid degredation at high stress levels in tension-tension cycling of ceramic-fiber / ceramic-matrix composites, can occur. Once broken, the fiber can no longer bear load [7, 48, 79].

The accumulated microcracking and fiber buckling fatigue models [6, 7,
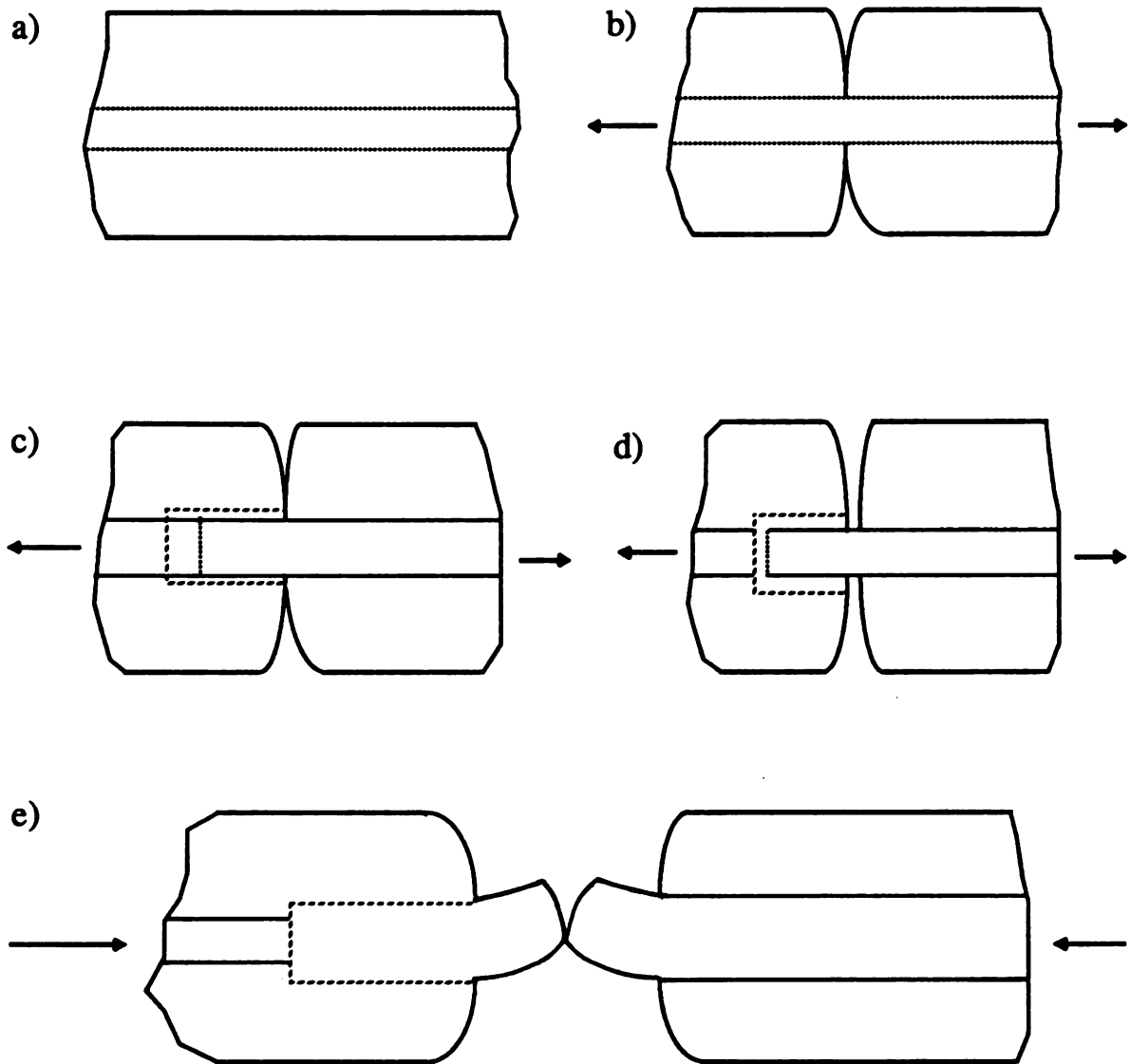
Figure 13. Schematic for fiber pullout fatigue mechanism in a fiber reinforced ceramic composite [7]. a) unbroken fiber in unloaded matrix, b) matrix cracks under moderate tensile stress, c) at higher load, fiber fails and debonds at weak point, d) at higher load, fiber is pulled out of matrix, suffering some damage from abrasion, e) as the composite is unloaded, if the fiber has been pulled out a sufficient distance, the fiber will buckle and fracture, instead of being forced back into its matrix hole. Broken fiber cannot bear any load, therefore the matrix crack advances, and the remaining fibers must carry the load.

48, 79] qualitatively explain fatigue mechanisms, but quantitative equations for fatigue life predictions are still developing.

The fiber buckling fatigue-model suggests that for reasonable reliability, design stresses must be kept below the level at which fiber pullout occurs, or at least below that in which fiber pullout exceeds a critical buckling length. Lewis and Rice liken such a stress level to the true fatigue limit in ductile metals [6, 7].

3.   Experimental procedure.

3.1.   Materials.

Low cycle flexural fatigue loading was performed on two commercially available composite materials. A unidirectionally reinforced glass fiber epoxy composite, 3-M Company type 1003, was prepared and provided by Dr. D. Liu of M.S.U. The second material, Macor (Corning code number 9658), a machinable glass-ceramic composite, was purchased from Astro Met Associates, Cincinnati Ohio, a licensed vendor of Corning Glass Works, Corning N.Y. Macor is a mica-glass ceramic composite in which small (2 by 50 microns or less) platelet-shaped fluorophlogopite crystals are nucleated and grown in a fluorine-containing parent glass [76, 77, 79]. See Appendix 6.A for the material properties of Macor and Appendix 6.B for 3-M 1003 GFRP.

3.2.   Specimen preparation.

Glass-epoxy test specimens were cut from a single parent plate, 7.5 cm wide by 20 cm long by 0.2 cm thick, using a Beuhler low speed 150 diamond grit saw, lubricated by Buehler cutting oil. The cutting direction was parallel to the reinforcing fibers. After cutting, the width dimension was equalized

end to end by sanding the edges along their length by hand with 600 grit wet-dry paper, laid on a flat surface. The corners of the specimens were kept as square as possible. No further treatment was applied, leaving the surfaces in the 'as received' condition.

The Macor specimens were cut from a single parent plate, 7.5 cm by 7.5 cm, using the same low speed 150 grit diamond saw. The widths were equalized end to end as for the GFRP specimens. The cut edges were slightly rounded (radius approximately 0.05 cm) with worn 600 grit SiC wet-dry paper (water flushed). The final specimen dimensions were 7.5 cm long, approximately 1.0 cm wide and 0.2 cm thick (as received). The Macor specimen bars were then annealed in air, in an electric resistance 'Lindberg' brand furnace. Specimens were placed on an alumina setter plate, with about a 0.5 cm spacing between specimens. The setter plate was made of 'Coors' brand AD96 alumina, 15 cm by 15 cm by 0.3 cm thick. The setter plate was then set on several scrap pieces of AD96 on the furnace brick in the center of the furnace. The anneal heat treatment began with a warm-up in the furnace to 200 °C for one hour, the temperature was then raised to 300 °C for one hour. The temperature was then raised to 500 °C, and the specimens were left to soak for fifteen hours. The furnace was then turned down and cooled to 300 °C over five hours, held for one hour, then cooled to 200 °C over three hours and held at 200 °C for four hours. The furnace power was then turned off. The specimens were allowed to freely cool to room temperature without opening the furnace for approximately twenty hours.

3.3.   Overview of experimental procedure.

Prismatic rectangular specimen bars, approximately one centimeter ± one millimeter wide, seven centimeters long and two millimeters thick (as recieved), were loaded in four point bending. Load cycling limits were

dependent on maximum and minimum load, rather than crosshead extension, which is a necessary procedure for brittle materials. The maximum load was set at a preselected percentage of the calculated rupture strength (Equation 17). The absolute maximum load varied from specimen to specimen due to slight variations in specimen width. The minimum load was set to zero. Crosshead speed was determined to be one half inch per minute by manually timing its displacement.

Load cycling was periodically interrupted after a predetermined number of cycles, in order to measure the specimen's internal friction and Young's modulus. A logarithmic scale for measurement was chosen with frequent interruptions early during the test, assuming that damage would occur rapidly at first, then increase less rapidly as fatigue progressed.

As Macor specimens fractured, the locations and conditions of fracture were noted. The fracture surfaces were cut off for examination under a scanning electron microscope.

Acoustic emission was detected from the specimen with parametric scaling by load for experiments using the glass-epoxy specimens. The acoustic emission analysis computer's parametric input eventually malfunctioned and temporarily did not respond to the load scaled parametric input. Acoustic emission was however recorded for several Macor specimens without load scaling. Subsequently, the load scaling capability was recovered.

The accumulated damage was estimated using the number of counts of acoustic emission given off during the loading process, as well as by changes in internal friction and Young's modulus. The acoustic emission was sorted into load ranges and summed up to the points at which load cycling was interrupted for sonic resonace measurements. Ultimately, the fatigue damage was measured by the change in the measured physical properties and the acoustic emission was related to those changes to determine the loads at which

the damage occured.

3.4.   Four point bending technique.

3.4.1.   Equipment and fixture.

The work was performed on an Instron Table Model low capacity screw driven tension/compression testing machine, circa 1965.

The semiarticulating four point bending fixture was designed by the author, based in part, on designs used by the Naval Research Laboratory [66], and following the recommendations of ASTM standards [23, 24, 25] (Figure 14). The fixture was built by machinists at the Physics Machine Shop of M.S.U. The fixture consists of a pair of load platens, machined from O-1 type steel. The load pin support bars were bolted to the platens. The upper load platen was bolted to the moving crosshead of the Instron. The lower load platen was designed to rotate to accomodate misalignment between the upper and lower load pins as they came in contact with the specimen.

The lower half of the swivel bearing was also machined from type O-1 steel. The bearing seat in both halves was 45°, conically drilled and polished. A one inch diameter, commercially available steel ball bearing enabled rotation of the fixture. All O-1 steel parts were heat treated after machining. After heat treating, the bearing seats were re-polished and mounting surfaces for the load pin bars were flat-ground.

After receipt of the fixture, it was decided that further flexibility in the choice of location for the acoustic emission transducer was desired. The author then redesigned the load pin support bars to allow adequate clearance to mount the AE transducer above or below the specimen, and machined them himself in the machine shop at Department of Engineering Research on the
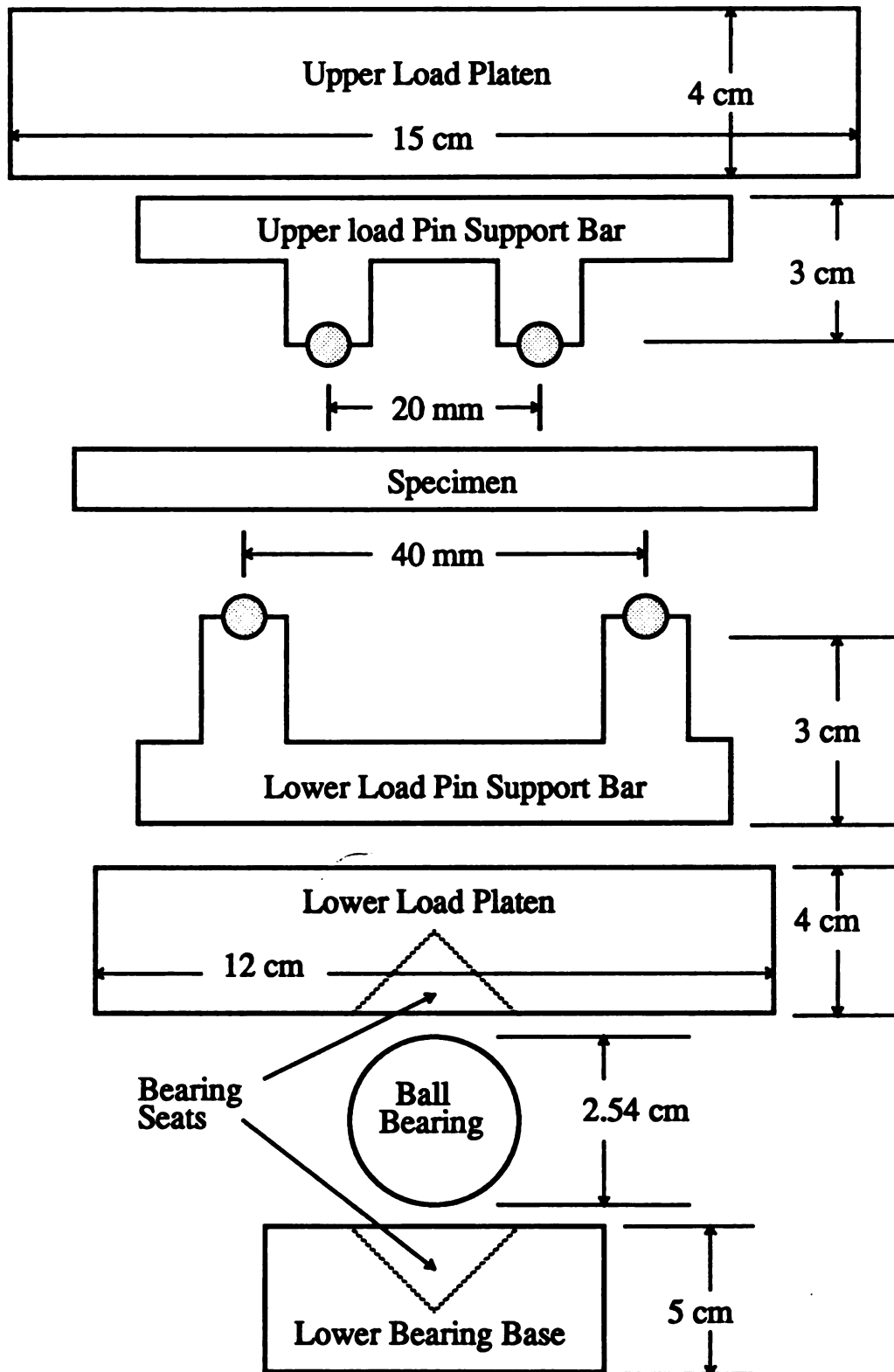
Figure 14. Schematic of four point bending fixture used for experiment. Dimensions not to scale.

M.S.U. campus. The material used for the load pin support bars was 1018 carbon steel. The upper load pin support bar was machined with a pin span of 20 mm. The lower load pin support bar had a pin span of 40 mm. Load pin grooves (in the support bars) were machined with a 4.7 mm (3/16") diameter and 1.5 mm depth to allow for some rotation during loading. The load pins were cut from a rod of commercially available 'die ejector pin' stock, with length 3 cm and diameter 3.2 mm (1/8"). Die ejector pin stock was chosen for its high hardness, strength, highly polished finish and availability.

The load pins were secured to the support bars by rubber bands ($\approx$1 inch free diameter). The rubber bands looped around the ends of the pins and ran under the support bar through a 3 mm deep relief groove cut into the load platen.

3.4.2.   Mechanical fatigue method.

Four point bending stress (R = -1, where R denotes the ratio of maximum to minimum stress, with the negative sign indicating compression) was applied to the specimen bar at room temperature, about 25 °C. Laboratory humidity varied between 50 to 70 percent relative humidity during the experimental procedure.

The glass-epoxy bars were fatigue cycled under four point loading at 25, 50 and 75 percent, respectively, of their static rupture strength of approximately 36 MPa [51].   Cyclic frequency was approximately 0.67 cycles per second, based on a crosshead loading rate of one-half inch per minute.

The Macor specimen bars were fatigue cycled in a similar manner, at 20, 30, 40, 50, 65 and 75 percent of its rupture strength of 100 MPa [69]. Maximum loads of 90, 85 and 80 percent of the theoretical rupture strength of 100 MPa were attempted, but every specimen fractured on the first or second

load cycle.

Once a particular fatigue testing run was started for the Macor and glass-epoxy specimens, the maximum load and loading rate was held constant. Effects of overloading, load changes or indentation crack growth are left for a subsequent study.

3.5.   Acoustic emission technique.

3.5.1.   Acoustic emission detection.

Acoustic emission was detected and analyzed using equipment manufactured by the Physical Acoustics Corporation, based in New Jersey. The 'PAC' Model 3000/3004 AE computer/analyzer was used with PAC 1220A preamps and PAC 300 KHz resonance transducers (Figure 15.a).

Background noise was examined by initially setting the analog section of the AE computer for absolute maximum sensitivity. Sensitivity was then decreased by raising the voltage threshold by two detent steps and lowering the overall amplification one detent step, so that random electrical noise no longer triggered the AE detection system. The voltage threshold setting was maintained at 0.3 x 10 volts. A sensitivity setting of 60 dB fixed gain on the preamp and 18 + 20 dB gain on the 3004 analog unit gave an overall system gain of 98 dB. The maximized sensitivity settings were maintained throughout the experiment after it was determined that background noise could confidently be avoided. Running the unit for up to thirty minutes in an idle state gave no AE events.

Acoustic emission was detected via a transducer mounted directly on the specimen's tensile side of flexure, in the center of the constant moment area. The transducer, also a PAC product, measured 8 mm in diameter, 10 mm in height and had an active 'Teflon pad' region of 6 mm diameter. The

69

Figure 15.a. Photograph of fatigue - AE experimental station.
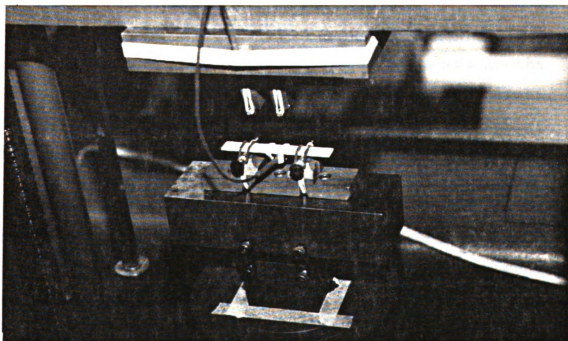
Figure 15.b. Closeup photograph of the four point bending fixture used for the experiment.

transducer was rated at a resonance frequency (highest response) of 300 KHz (Figure 7).

Consistent bonding of the transducer to the specimen was accomplished by using a thin layer of Dow Corning brand 'High Vacuum' silicone grease intended for glass to rubber vacuum fittings. The transducer was secured to the specimen with a doubled rubber band, with the 'X' of the crossover point across the back of the transducer. Common office type rubber bands were used, with a free diameter of about 3 cm and a band width of about 0.5 cm. The higher aspect ratio of width to thickness seats better on the back of the transducer, exhibiting less slippage. Bonding and debonding the transducer by a cement was considered impractical, as it would tend to degrade the specimen and the transducer, and would interfere with the sonic resonance measurements.

3.5.2.   Machine noise quantification.

Machine noise also must be examined, quantified and determined to be isolatable from the specimen's acoustic emission. Machine noise must be known as accurately as possible, in order to qualify and give credibility to other experimental results. Machine noise is considered part of the background noise which is at least 50 dB below the threshold set for the response of the AE system software. Typically, screw driven crosshead machines are much quieter than the servo-hydraulic type [61, 64]. Machine noise is also typically in the low kilohertz range, while ceramic cracking acoustic emission is typically in the high kilohertz range, with components in the megahertz range (Figure 7, page 23) [31]. The difference between frequency ranges of acoustic signals allows for the electronic exclusion of the machine noise by proper choice of transducer response ranges and signal processor settings.

Three distinctly separate experiments were performed to show machine noise under various operational conditions. For this series of tests, two channels of AE aquisition were used, with identical control settings, along with two nominally identical AE transducers. One transducer was mounted to the specimen's tensile face and the other transducer was mounted on the center of the front face of the upper load platen (the platen mounted to the crosshead) (Figure 15.b).

To test for machine noise at the points of load reversal, a previously undamaged glass-epoxy specimen (GE-5) was load cycled at a relatively low load (22.27 N). 22.27 N (5 lb.) was approximately 1.7 percent of the rupture modulus. Very little fatigue damage was expected to occur at that low load. The test was interrupted every 100 cycles to check for changes in Young's modulus or internal friction, by using the sonic resonance system. A maximum of 500 load cycles were run. An initially undamaged specimen was used.

Two tests for machine noise as a function of load were performed. In one, the specimen was load cycled at a low load initially for 100 cycles, then the load was increased for another 100 cycles. The fatigue load was stepped up to the maximum of 222.5 N (50 lb.) used for the actual experiment. At each stage of the test, the acoustic activity detected by both transducers was compared to the AE observed in the prior stages. If machine noise was a function of load, then the AE detected by the transducer located on the load platen would increase proportionally with load, if not, only the AE detected by the specimen mounted transducer should show an increase with load.

Isolation between the two transducers was also investigated. If the specimen mounted transducer detected an AE event immediately after the load platen mounted transducer did (or vice versa), then some degree of communication between them would be indicated. The degree of communication may be measured in terms of the relative differencs detected

between event amplitude or number of counts.

A third test combined elements of the first two tests. Load was applied
to the specimen, then released, in increasing load steps, with one application
of each given load. The procedure also explored the Kaiser effect of the
GFRP material, in particular, the number of acoustic events is expected to
increase only after the current load exceeded the highest previous load, and
there is no machine or system noise transferring into the specimen.

3.6.   Sonic resonance technique.

The sonic resonance technique was used, to determine internal friction
(Equation 5), and Young's modulus (Equation 7). ASTM standard
procedures were followed [15-17].

The procedure used for the determination of internal friction consisted
of suspending the specimen by ordinary white cotton sewing thread from two
identical piezo-electric transducers (monaural phonogragh cartridges,
'ASTATIC' brand, part number 62-1, needle type N27-1). One transducer
was driven at the specimen's flexural fundamental resonant frequency
(ASTATIC cartridge maximum input = 3.0 V_{RMS}). The RMS voltage output
of the pickup transducer was then measured, after bandpass filtering (set at
one half and twice the resonant frequency) and amplification. The signal to
the driver was then cut off with a 'bounceless contact' type switch. The
number of times the voltage amplitude of the 'ring down' of the specimen
exceeds a preset reference level (V_2, Equation 5) was counted using a
universal digital pulse counter. The threshold or reference level (V_2) was set
by the experimenter to a level below the peak driven output voltage. This
level obtained a number of counts (N, Equation 5) in a range from 100 to 500.
The reference level was restricted to a minimum value at least 20 percent

above the peak noise level i.e. {1.20 (1.414 V_{RMS})} (Figure 16).

Wachtman and Tefft's nonlinear least squares curve fitting program was used to subtract the effect of suspension fixtures from the specimen's actual internal friction [86]. For an acceptable correlation coefficient, at least five data pairs (of ft = N and the point of suspension's normalized distance from the free ends of the bar) must be read from the specimen. Data pairs were read starting at about 2 mm from the free ends of the specimen, and continued by stepping inward two to five mm per step. At least two data pairs were read from inside the fundamental flexural node. For each position at which a data pair was read, a minimum of ten 'free decay' values were taken. At least ten readings were necessary, due to scatter in the number of times the output voltage crossed the reference.

3.7. Preparation for scanning electron microscope fractography.

Macor specimens that fractured after 500 to 2500 fatigue cycles were prepared for scanning electron microscope (S.E.M.) observation by cutting off the fracture surfaces at about one centimeter from the fracture. The same low speed saw used for initial specimen preparation was used for this operation.

The shear crack in the GFRP specimens was of great interest, due to its suspected influence on Young's modulus and internal friction. The existence of a fiber bridged zone between the crack faces was investigated by cutting GFRP specimen GE-4 in half across the width. One of the half pieces was cut in half again lengthwise to expose both midsections (transverse and longitudinal) of the bar. One of the quarter pieces of GFRP specimen GE-4 was partialy split open from the short midsection, approximately five millimeters, to provide a look into the fiber bridged zone.
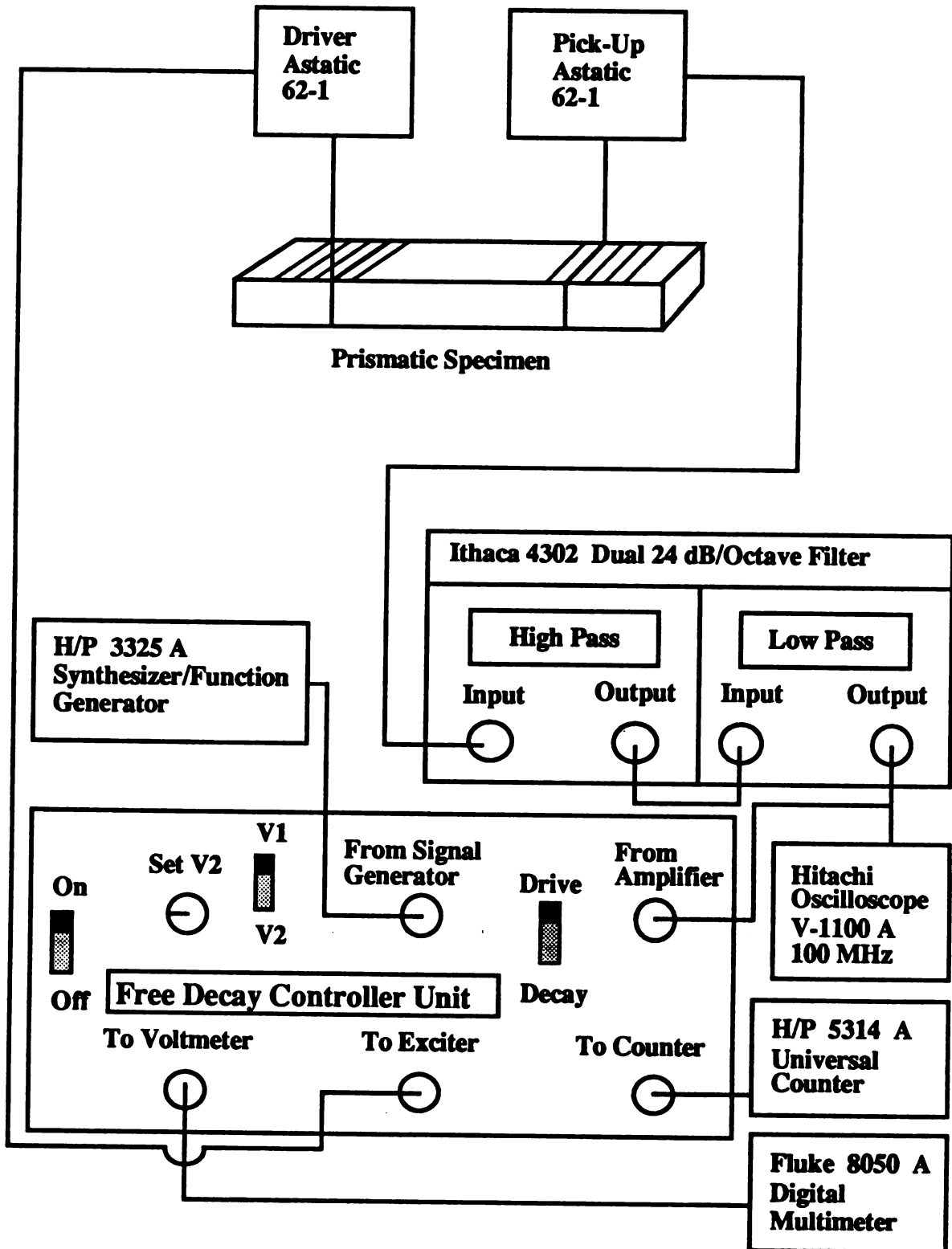
Figure 16. Block diagram of sonic resonance system.

All specimens and mounting stubs were cleaned using methanol in an ultrasound cleaner for 20 to 30 minutes. Both fracture surfaces (each side of the fracture) from each specimen were mounted on the same stub, with fracture surfaces oriented normal to the electron beam for good depth and field of focus.

The mounting stubs used were prepared from 1018 carbon steel. Stub dimensions were 1/2 inch in height and 5/8 inch diameter, to fit the receiver in the stage of the S.E.M. Clean fractured specimen sections were glued to the stub with 'DUCO' brand 'household cement' (Devon Company, Wood Dale, IL 60191). The glued-up specimens were dried for at least 20 minutes under two 150 watt light bulbs in close proximity.

The nonconductive specimens were sputter coated with gold to allow the electron beam to be conducted away from the surface of the specimen without spot charging on the surface. Sputter coating was accomplished at the Center for Electron Optics, located in the Pesticide Research building, on the M.S.U. campus. The sputter coating device used was an Emscope Sputter Coater, Model SC 500, manufacturedby Emscope Company, Wotton Road, Ashford, Kent, U.K.

The sputtering procedure began with setting the prepared specimens into the sputtering chamber. The chamber was evacuated to approximately 0.06 Torr. The chamber was then purged with argon gas and pressure was maintained at approximately 0.1 Torr. The coating parameter of 20 ma current gave a coating rate of about 7 nanometers per minute, per recommendation in the Emscope's operation manual. Exposure times of 30 seconds (Macor) and 90 seconds (GFRP) gave a coating thickness of 3 to 4 nm (Macor) and 10 to 12 nm (GFRP). The chamber was then flooded with argon and pressure was equalized to atmospheric pressure. The cover of the chamber was then raised, and the specimens were removed. After sputter coating, the specimens were kept in a small, covered plastic box to prevent contamination by handling and dust from the environment.

# 4.	Results and discussion.

## 4.1.	Thought experiment model for acoustic emission during monotonic increasing flexure in a GFRP composite.

Using a thought experiment, based on the literature [6, 7, 50-65], one can envision the 'noise generating' mechanisms that are operative during the loading of the unidirectionally reinforced GFRP composite in four point bending. Upon initial loading, on the tensile face of curvature, the epoxy matrix begins to crack transversely to the fibers. The crack spacing is roughly proportional to both the maximum stress and the volume fraction of fibers [52]. Matrix cracking likely produces acoustic emission events of relatively high intensity, i.e. amplitudes of about 60 to 70 dB, high numbers of counts per event (20 to 100), temporal durations of 200 to 300 microseconds, and short to medium rise times of about 50 to 100 microseconds [59-63].

As the unidirectionally reinforced matrix fails, the reinforcing fibers begin to break and pull out of their holes in the matrix, bridging the crack wake [56]. As pullout and bridging occurs, an initial 'snap' may occur as the fiber breaks and the interface breaks loose due to the high elastic modulus of the fiber, followed by frictional AE as the fiber is dragged out of its hole [56, 59]. The level of frictional AE from pullout is likely quite low, however, in view of the sheer number of fibers participating in pullout, we may detect this emission as a general low level 'tail' following a high intensity burst as the matrix cracks.

As an aside, for a randomly oriented fiber or whisker distribution, few fibers will be oriented normal to the crack surfaces. Many fibers will break immediately due to the bending moment imposed by geometry. The majority of fiber breakage likely occurs simultaneously with the opening of the matrix

crack. Therefore, AE activity from fiber breakage and matrix cracking may be recorded together, causing a larger number of counts per event to be detected per AE burst. The combination of fiber breakage and matrix cracking is not seen as a completely adverse situation because, although inseparable, both sources contribute to 'new damage' emission.

With higher loading, the unidirectional GFRP composite's bridging fibers begin to break and further matrix cracking, fiber pullout and shear cracking or interply splitting (due to fiber-matrix debonding) may occur. At this point, the dominant acoustic source is likely the shear crack, due to the large surface area of its faces in frictional contact with each other [59, 60]. The magnitude of the frictional AE generated by the shear crack may likely overshadow or mask any other acoustic mechanism in operation.

Determining the active acoustic emission mechanisms is a matter of some subjectivity and philosophy, based on one's understanding (or lack of understanding) of the damage modes and their progression during fatigue failure.

4.2. Determination of uncertainty of internal friction and Young's modulus measurements made on the sonic resonance system.

A series of measurements was performed on the sonic resonance system, to determine the uncertainty or error margin for readings made during the course of the experiment. Measurements were made at two different suspension points on the specimens, to check for any difference in data scatter due to the relative positions on the bar. One set of readings was made at 0.12 normalized distance (n.d.) from the free end of the bar, and another set of readings was made at 0.32 n.d. The fundamental flexural node was located at approximately 0.223 n.d. from the free ends of the bar, thus the suspension

positions were equidistant on either side of the node.

The working standard specimens for each material were used for this exercise. Both working standard specimens were cut from the same parent plates for each material. The dimensions of the working standard specimens were kept as close as possible to the average dimensions of the specimens actually used for the experiment (width being the only dimension in control; length and thickness remained as received).

To determine the error in Young's modulus, twenty individual determinations of the fundamental flexural resonant frequency were made. Since Young's modulus is related to the square of the resonant frequency (Equation 5, Section 2.4.1), the values for F_r were converted into values of Youngs' modulus, then statistically analyzed for the mean and standard deviation.

The uncertainty in internal friction was determined by making eight groups of ten readings. Each group, consisting of ten individual readings of V_1, V_2 and N (Equation 6, Section 2.4.2) were converted into a group mean, and a standard deviation as the measure of scatter.

For all readings or groups of readings, the specimen was either completely removed from the hanging threads and then rehung, or the threads were loosened and moved about, simulating removal and then repositioned.

Table 2 lists uncertainty data for both Young's modulus and internal friction, sorted by specimen material and suspension location. For the GFRP material, uncertainty (one standard deviation) in Young's modulus at 0.12 n.d. is about 0.027 percent, and at 0.32 n.d. is about 0.048 percent. The error in measurement of internal friction at 0.12 n.d. is about 2.3 percent and at 0.32 n.d. is about 3.4 percent, which indicates the readings made at 0.12 n.d., i.e. outside the flexural node, may be more accurate by up to forty five percent for Young's modulus and up to thirty percent more accurate for internal friction.

79

Table 2.   Uncertainty data for sonic resonance measurements of Young's modulus and internal friction.

Specimen	Normalized Hanging Position *	Mean ** Young's Modulus	Std. Dev. **	Mean Q^{-1} ***	Std. Dev. ***
GE-2 (GFRP)	0.12 (8 mm)	43.694 (GPa)	0.0119 (GPa)	2.789×10^{-3}	0.0645×10^{-3}
	0.32 (24 mm)	43.653	0.0209	2.762×10^{-3}	0.0935×10^{-3}
MA-16 (Macor)	0.12 (9 mm)	62.148	0.0088	5.594×10^{-4}	0.136×10^{-4}
	0.32 (24 mm)	62.084	0.0049	3.851×10^{-4}	0.071×10^{-4}

*   The nodal position for the fundamental flexural vibrational mode is located at a normalized distance of 0.223 from the free ends of the bar. The normalized distances listed here are also measured from the free ends of the bar.

**   The mean and standard deviation for the measurements of Young's modulus were based on twenty measurements per suspension position per specimen.

*** The mean and standard deviation for the measurements of internal friction (Q^{-1}) were based on eight groups of ten readings per suspension position per specimen.

For Macor, the uncertainty in the measurements of Young's modulus at 0.12 n.d.was about 0.014 percent, and at 0.32 n.d. about 0.008 percent. The error in internal friction measured at 0.12 n.d. was about 2.43 percent and at 0.32 n.d. was about 1.84 percent. This error indicates that the readings at 0.32 n.d. may be more accurate by about 43 percent for Young' modulus and 24 percent for internal friction.

No judgement or explanation can be made regarding the observation of less data scatter at the measurement positions inside the flexural node for the GFRP specimen and outside the flexural node for Macor. However, the differences in absolute values of the two physical properties and the differing types of reinforcement may have some influence.

Small errors are largely a function of the experience and ability of the operator. In order to minimize error, great care must be taken to ensure the accurate positioning of the specimen suspension threads. It is essential to develop a consistent procedure for finding the resonant frequency for Young's modulus, and the setting of a threshold voltage for a similar number of 'N' counts for internal friction. By showing experimental uncertainty to be self-consistent and of a relatively small magnitude, the accuracy and reliability of other measurements, as the detection of fine degrees of change, can be realistically interpreted.

To account for the possibility of transducer drift in the response of the sonic resonance system, periodic measurements (made over five months), using the GFRP working standard specimen, showed that the difference in values for Youngs' modulus varied by approximately ± 0.010 GPa (0.023 percent, approximately the same as the measurement scatter). The minor variation indicated negligible change in the response of the transducers over the time of the study. The average modulus of the GFRP control specimen was 43.808 GPa.

Statistically, if a measured 'change' of Young's modulus or internal

friction falls within the standard deviation for measurement , it is less
likely that there will be a real difference in actual values. A measured
difference of two standard deviations implies a 68 percent probability that
actual change has occured. A difference of four or more standard deviations
implies that the measured change is of high probability to be real.

4.3.   Machine noise qualifications.

Three separate tests were run to determine the effect of machine or
system noise on the acoustic emission detected from the specimen during
fatigue.

It is reasoned that, during mechanical fatigue, the quietest possible
specimen will be the most free from extraneous noise. Machine functions,
such as gears and chains reversing direction and electrical relays clicking, are
potential sources of noise, as well as the action of physically fatiguing the
specimen, where the loading fixture contacts the specimen.

4.3.1.   22.3 Newton maximum load fatigue test.

A fatigue test of one thousand load cycles was run on GFRP specimen
GE-5, with a 22.27 N (five pounds) maximum load. This test provided two
important results for interpreting the data from the higher load fatigue tests of
the GFRP composite and the Macor composite.

Acoustic emission transducers were placed on the front face of the upper
load platen and on the middle of the tensile face of the specimen. Two of the
four channels available with the P.A.C. acoustic emission computer were used
for signal processing. A load scaled voltage signal was connected to the
parametric input of the AE computer to allow sorting of AE by load. Both
channels would occasionally go for several load cycles without detecting any

acoustic events, indicating that machine noise, along with damage noise, is an inconsistent source.

The AE observed during the 22.3 Newton maximum load test of GFRP specimen GE-5 included substantial AE events at both ends of the load range (Figure 17). Very little or no damage was expected to occur with the low maximum load of 22.3 N. However, as indicated by changes in internal friction and Young's modulus (Tables 3.a and c), some damage probably occured. A maximum change in Young's modulus of 0.07 GPa was measured at 0.12 n.d., which is 0.17 percent of the mean value. Experimental uncertainty (Table 2, page 80) of 0.012 GPa (smaller than the measured change in Young's modulus by a factor of 5.8), measured at the same suspension location, indicates that a real change has occured. This also implyies that some amount of real damage has also occured. The implication of damage is supported by a change of internal friction of 2.23×10^{-3}, measured at 0.12 n.d. (Table 3.a). Experimental uncertainty in the measurement of internal friction, determined to be approximately 0.065×10^{-3} (Table 2), also measured at 0.12 n. d., indicated that the change was larger than the uncertainty by a factor of 34 times (Table 3.c).

If no damage had been indicated, then the accumulation of AE events at the ends of the load range would suggest that machine noise is a function of the number of loading cycles. Evidence of damage suggests that a percentage of the AE events detected at the ends of the load range may be due to real damage in the specimen.

A second result of the 22.3 N fatigue test indicates that machine noise does not transfer to the specimen. Events of high relative amplitude and over one hundred counts were detected by the load platen transducer, but in the next few events recorded, no event was detected by the transducer located on the specimen, or several seconds would elapse before the next event was detected at either the specimen or load platen.
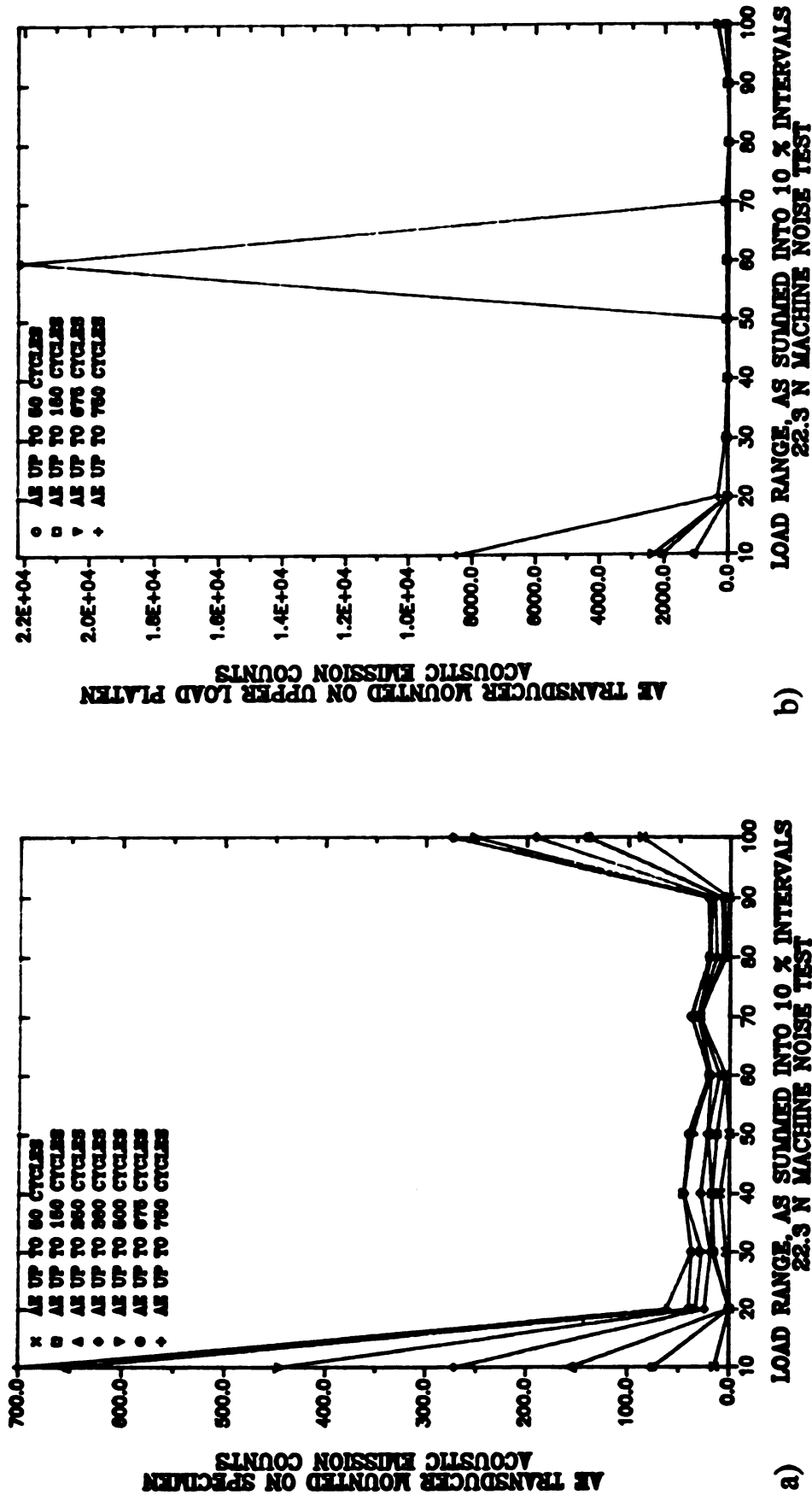
Figure 17. Acoustic emission counts per load range for GFRP 22.3 N machine noise test. a) AE transducer mounted on specimen, b) AE transducer mounted on upper load platen.

Table 3.a. Maximum changes of Young's modulus and internal friction for GFRP fatigue specimens, measured at 0.12 normalized distance from end of specimen bar. Data for working standard is provided for comparison of measurement scatter to actual measured change in property.

Specimen (max load) [# cycles]	Young's Modulus (GPa)				Internal Friction			
	Max [# cycles]	Min [# cycles]	Δ	Pct. change	Max [# cycles]	Min [# cycles]	Δ	Pct. change
GE-5 (22.3 N) [1000]	41.240 [0]	41.170 [500]	0.07	0.170	4.95 $(\times 10^{-3})$ [500]	2.72 $(\times 10^{-3})$ [150]	2.23	58.15
GE-1 (111.3 N) [10 K]	41.643 [20]	41.486 [50]	0.157	0.378	4.98 $(\times 10^{-3})$ [100]	2.35 $(\times 10^{-3})$ [250]	2.36	64.40
GE-3 (155.8 N) [10 K]	41.822 [0]	41.713 [250]	0.109	0.261	4.54 $(\times 10^{-3})$ [10]	3.00 $(\times 10^{-3})$ [500]	1.54	40.85
GE-4 (200 N) [10 K]	43.776 [0]	43.653 [150]	0.123	0.281	4.00 $(\times 10^{-3})$ [350]	3.05 $(\times 10^{-3})$ [3]	0.95	13.77
Error in msmt of GE-2	Mean = 43.695 (GPa) (Working Std.)		Std. Dev. .01191	C.O.V. * .027%	Mean = 2.789 $(\times 10^{-3})$ (Working Std.)		Std. Dev. .064	C.O.V. * 2.3%

* C.O.V. is the coefficient of variation, defined as the standard deviation divided by the mean.

Table 3.b. Maximum changes of Young's modulus and internal friction for Macor fatigue specimens, measured at 0.075 normalized distance from end of specimen bar. Data for working standard is provided for comparison of measurement scatter to actual measured change in property.

Specimen (max load) [# cycles]	Young's Modulus (GPa)				Internal Friction			
	Max [# cycles]	Min [# cycles]	Δ	Pct. change	Max [# cycles]	Min [# cycles]	Δ	Pct. change
MA-12 (.75 MOR) [5000]	62.67 [0]	62.51 [250]	0.16	0.256	15.80 $(x10^{-4})$ [500]	11.90 $(x10^{-4})$ [50]	3.90	28.16
MA-11 (.65 MOR) [5000]	64.09 [1000]	63.98 [0]	0.11	0.172	15.30 $(x10^{-4})$ [0]	12.40 $(x10^{-4})$ [1000]	2.90	20.94
MA-9 (.50 MOR) [2500]	62.34 [0]	62.26 [500]	0.08	0.128	14.70 $(x10^{-4})$ [100]	12.40 $(x10^{-4})$ [500]	2.30	16.97
MA-7 (.40 MOR) [5000]	62.31 [500]	62.28 [100]	0.03	0.048	11.65 $(x10^{-4})$ [0]	10.55 $(x10^{-4})$ [1000]	1.10	9.91
MA-6 (.40 MOR) [1000]	62.02 [100]	61.98 [500]	0.04	0.064	13.60 $(x10^{-4})$ [0]	17.60 $(x10^{-4})$ [500]	4.00	25.65
MA-4 (.30 MOR) [5000]	62.13 [500]	62.04 [0]	0.09	0.145	10.725 $(x10^{-4})$ [5000]	8.454 $(x10^{-4})$ [0]	2.271	23.68
MA-2 (.20 MOR) [500]	63.58 [3]	63.52 [250]	0.06	0.094	10.70 $(x10^{-4})$ [250]	5.60 $(x10^{-4})$ [0]	5.10	62.58
Error in msmt of MA-16	Mean = 62.148 (GPa) (Working Std.)		Std. Dev. .0088	C.O.V. .015%	Mean = 5.594 $(x10^{-4})$ (Working Std.)		Std. Dev. .136	C.O.V. 2.43%

Table 3.c. Maximum changes of Young's modulus and internal friction for GFRP fatigue specimens, measured at 0.32 normalized distance from end of specimen bar. Data for working standard is provided for comparison of measurement scatter to actual measured change in property.

Specimen (max load) [# cycles]	Young's Modulus (GPa)				Internal Friction			
	Max [# cycles]	Min [# cycles]	Δ	Pct. change	Max [# cycles]	Min [# cycles]	Δ	Pct. change
GE-5 (22.3 N) [1000]	41.190 [50]	41.180 [0]	0.01	0.024	4.70 ($x10^{-3}$) [50]	3.28 ($x10^{-3}$) [150]	1.42	35.59
GE-1 (111.3 N) [10 K]	41.530 [20]	N/A *	N/A	N/A	N/A	2.02 ($x10^{-3}$) [250]	N/A	N/A
GE-3 (155.8 N) [10 K]	41.720 [0]	41.618 [2000]	0.102	0.245	4.00 ($x10^{-3}$) [50]	2.43 ($x10^{-3}$) [2000]	1.57	48.83
GE-4 (200 N) [10 K]	43.651 [0]	43.577 [150]	0.074	0.170	6.05 ($x10^{-3}$) [400]	2.45 ($x10^{-3}$) [3]	3.60	84.7
Error in msmt of GE-2	Mean = 43.653 (GPa) (Working Std.)		Std. Dev. .021	C.O.V. .048%	Mean = 2.762 ($x10^{-3}$) (Working Std.)		Std. Dev. .094	C.O.V. 3.38%

* N/A = not applicable, due to impossibility of taking a reading at that position, at that time.

87

Table 3.d. Maximum changes of Young's modulus and internal friction for Macor fatigue specimens, measured at 0.32 normalized distance from end of specimen bar. Data for working standard is provided for comparison of measurement scatter to actual measured change in property.

Specimen (max load) [# cycles]	Young's Modulus (GPa)				Internal Friction			
	Max [# cycles]	Min [# cycles]	Δ	Pct. change	Max [# cycles]	Min [# cycles]	Δ	Pct. change
MA-12 (.75 MOR) [5000]	62.393 [0]	62.343 [2500]	0.05	0.080	5.369 ($x10^{-4}$) [500]	4.396 ($x10^{-4}$) [100]	0.973	19.94
MA-11 (.65 MOR) [5000]	63.826 [0]	63.794 [2500]	0.032	0.050	4.655 ($x10^{-4}$) [500]	3.892 ($x10^{-4}$) [0]	0.763	17.85
MA-9 (.50 MOR) [2500]	62.123 [0]	62.088 [1000]	0.035	0.056	5.434 ($x10^{-4}$) [2500]	4.708 ($x10^{-4}$) [1000]	0.726	14.32
MA-7 (.40 MOR) [5000]	62.152 [0]	62.127 [2500]	0.035	0.056	5.311 ($x10^{-4}$) [2500]	4.309 ($x10^{-4}$) [0]	1.002	20.83
MA-6 (.40 MOR) [1000]	61.850 [0]	61.833 [1000]	0.017	0.027	5.433 ($x10^{-4}$) [500]	4.340 ($x10^{-4}$) [0]	1.093	22.37
MA-4 (.30 MOR) [5000]	61.934 [500]	61.903 [5000]	0.031	0.050	5.386 ($x10^{-4}$) [100]	3.986 ($x10^{-4}$) [0]	1.400	29.88
MA-2 (.20 MOR) [500]	63.413 [3]	63.380 [500]	0.033	0.052	4.523 ($x10^{-4}$) [500]	3.059 ($x10^{-4}$) [0]	1.464	38.62
Error in msmt of MA-16	Mean = 62.084 (GPa) (Working Std.)		Std. Dev. .0049	C.O.V. .008%	Mean = 3.851 ($x10^{-4}$) (Working Std.)		Std. Dev. .136	C.O.V. 2.43%

To determine the source of the high numbers of events at the ends of the load range, two other runs of this experiment were performed, with slight hardware differences. One thousand load cycles were performed in each run.

In one test, a 122 Newton weight was placed on the crosshead to prevent rocking of the crosshead during load reversals. The accumulation of AE events at the high end of the load range was substantially reduced to a level even with the midstroke AE , while the number of AE events at the low end of the load range was reduced by a factor of about three (from about 750 down to about 260).

The addition of a weight to the crosshead implies that the majority of AE events at the high end of the load range are likely to be due to the crosshead rocking slightly during the load reversal from increasing to decreasing load. At the low end of the load range, there was a significant addition of extraneous AE by crosshead motion at load reversal. Therefore, the results of further fatigue tests must be interpreted on that basis.

A second variation of the 22.3 N maximum load fatigue test involved the same 122 N weight on the crosshead as before, but with the addition of plastic sleeves to the load pins, and a thin coat of lubricant (the same silicone vacuum grease used to couple the AE transducer to the specimen) between the specimen and the sleeved load pins. Plastic sleeves two centimeters long were made from the smooth insulation casing of a length of scrap electrical wire. The casing had a slightly smaller inside diameter size than the load pin, and was forced over and centered on the pin. Again, the specimen-mounted transducer showed that the high end of the load range showed no more AE events occuring than during the mid-range of loading (the same result as the high end of the 'crosshead weight only' test). A substantial increase in the AE events detected at the low end load reversal was noted, with a total accumulation, during 1000 load cycles, of about 6200 counts. The addition of lubricated plastic sleeves to the load pins evidently caused a detrimental

increase in the number of AE events at the low end load reversal. The increase was possibly due to a 'squeaking' action of the specimen moving against the sleeved load pins at that point.

The best of the test conditions indicated by the results of the three 22.3 Newton fatigue tests are: (1) add the weight to the crosshead, which prevents its rocking, thereby quieting down the load reversals - especially the high end load reversal, (2) do not add plastic sleeves to the load pins, which significantly raised the number of AE events at the low end load reversal.

The interpretation of AE-fatigue data acquired with no weight on the crosshead or sleeves on the load pins must acknowledge that the primary source of AE at the points of load reversals is likely due to crosshead motion relative to the specimen. AE detected during midstroke is likely due to specimen damage.

There appears to be evidence supporting the possibility that all AE detected at the ends of the load range is not due to the fatiguing system. At this point, it is uncertain what fraction of the AE is attributable to either the specimen or to the system. It is not justifiable to subtract some fraction of AE events or counts from those detected at the end ranges of load for other specimens involving higher loads and more fatigue cycles. Therefore, we do not place undue emphasis on the reliability of the AE detected at either the high or low load ranges where load reversal occurs.

4.3.2. Stepped maximum load fatigue test.

An undamaged GFRP specimen was load cycled for one hundred cycles at each of five load levels. Load levels started at 44.5 Newtons (ten pounds), and increased by 44.5 N each change up, to a maximum of 222.5 N (fifty pounds). Three experimental sets of conditions were tested. The first set of test conditions used no weight on the crosshead and no plastic sleeves or

lubrication on the load pins. This setup is exactly the same as that used during the actual fatigue runs of the GFRP and Macor specimens. The second set of conditions was to add only the 122 N steel weight to the crosshead to prevent its rocking. The third set of conditions used the crosshead weight and added the same plastic sleeves to the load pins as described in Section 4.3.1. Acoustic emission transducers were placed on the middle of the specimen's tensile face and on the front face of the upper load platen.

Under the first set of conditions, acoustic emission detected on the specimen at the low end of the load range increased with each increase in applied load, to a total of about 165 counts. At the high end of the load range, accumulation of AE occured slightly faster than in the middle of the load range, but at a much lower rate than at the low end, totaling only about 50 counts.

AE detected by the transducer mounted on the load platen was significantly higher across the entire load range. About 3300 counts were observed at the low end of the load range, about equal in number from each increasing load. About 1200 counts were observed at the high end of the load range, decreasing in number of counts with each increasing step in load.

Under the second set of conditions, the transducer on the specimen detected far fewer acoustic events at the high end of the load range, rising only slightly from the level of AE detected throughout the middle of the load range. At the low end of the load range, the specimen mounted transducer detected about 50 counts during each step of load increase. In the middle of the load range, the distribution of acoustic counts was quite smooth.

The AE transducer mounted on the load platen detected about 100 more events at the high end than at the low end of the load range. The middle of the load range exhibited several high intensity events in each step of increased load, but at no consistent absolute load.

Under the third set of conditions, the AE detected by the transducer

mounted on the specimen was very similar throughout the load range from the middle to the high end of the load range. AE detected at the low end of the load range totaled 2715 counts with about 100 counts detected up through the second load step, and about 1200 in the third step, 900 counts in the fourth step and finally about 400 counts in the last (highest load) step.

AE detected at the upper load platen was higher at the high end of the load range, totaling about 1100 counts, with about 80 counts observed in each of the first four load steps, and about 800 counts detected during the highest (222.5 N) load step.

The result of the series of stepped load fatigue tests is that: (1) acoustic emission detected at the high end of the load range (under experimental conditions of no crosshead weight or sleeves on the load pins) is largely due to crosshead movement during load reversal (from increasing load to decreasing load), and (2) there is little or no evidence of communication of acoustic energy from the crosshead to the specimen.

4.3.3.   Kaiser effect test.

An increasing series of loads was applied to GFRP specimen GE-7, starting with 45.5 N, stepping up each time by 44.5 N, up to 222.5 N with one application of each load level. Test conditions were the same as for the first set in section 4.3.2., i.e. no weight on the crosshead and no sleeves on the load pins. AE was detected with one transducer, mounted on the specimen.

AE accumulated during the application of every load. Only during the removal of the first (44.5 N) load was AE detected during load relaxation. According to Awerbuch et al. [60], the lack of acoustic events (from the specimen) at the low load condition implies that machine noise is undetectable or not present.

The Kaiser effect test indicates that essentially no AE was detected during load release, possibly implying low or no machine noise entering the system through the specimen.

4.3.4. Comparison of AE from load pin and specimen.

As stated in Section 2.5, the use of the load pins of the four point bend fixture as AE wave guides was investigated.

Adjustment of amplifier gain and threshold settings on the P.A.C. amplifier, set to detect approximately the same number of AE events, indicated that an amplitude difference of approximately -50 to -65 dB existed between mounting the transducer on the lower span load pin and directly on the middle of the tensile face of the specimen. The lower span load pin sits in the part of the fixture that sits on the load cell, which in turn is bolted to the frame of the Instron (Figure 14). The use of the load pin in the upper part of the fixture was ruled out due to the results of tests involving mounting the transducer on the upper load platen (see dicussion in Sections 4.3.1 and 4.3.2).

For the same number of events, the AE events/load distribution profile taken from the load pin was drastically different from that taken directly from the middle of the tensile face of the specimen. The distribution profile taken from the loading pins showed a nearly flat profile with a few apparently random spikes. The AE events/load distribution profile from the specimen-mounted transducer showed apparently good response with lower sensitivity settings, eliminating background noise, indicating a consistently poor acoustic coupling between the load pin and the specimen. Thus, the load pin cannot be used as an AE guide path since the pins attenuate AE signals by about 60 dB.

The poor acoustic coupling between the specimen and the load pins also works to an advantage in reducing machine noise by 50 to 65 dB.

4.3.5.   Results of machine noise tests.

The effect of mechanical fatigue loading on the AE detected from the specimen is to inflate the number of events detected at the high end of the load range, based on the reductions in AE seen when the crosshead is weighted. The AE detected during the middle of the load stroke appears to be largely due to the specimen. At the low end of the load range, where load reversal from decreasing to increasing load occurs, no reduction in the number of AE events detected could be made. Adding sleeves to the load pins significantly increased the number of AE events detected, implying that the AE detected at the low end of the load range may be actually generated by the specimen.

4.4.   Results of fractography.

4.4.1.   GFRP fractography.

A midplane shear crack (interply delamination) grew throughout all fatigue loaded GFRP specimens, except specimens GE-5 which experienced a fatigue load of only 22.3 N, and specimens GE-6 and GE-7, which were used for the stepped-load machine noise tests and saw only limited fatigue loading.

Examination of the thickness side of the fatigue loaded GFRP specimens in a 10 to 250 X inverted stage optical metallographic microscope did not reveal the shear crack length at any magnification. The specimen was also viewed in a 10 to 150 X stereomicroscope, and again no crack was visible under any lighting condition or magnification. It seemed implausible that the shear crack did not intersect the side surface of the specimen, especially when the unaided eye could obviously and clearly see the crack demarked by lighter and darker halves of the specimen separated by the crack, when viewed near a strong incandescent or fluorescent light. The only explanation for the

93

invisibility of the crack at the suface may be a tightly tied 'fiber bridged zone' between crack faces, holding them together with the nearly perfect mating and closure of the crack faces.

A scanning electron micrograph of the thickness side of the GFRP specimen GE-4 (where the midplane crack was believed to intersect the surface), confirms the intersection of the crack with the surface of the specimen (Figure 18). The crack opening displacement is estimated at about 6.5 microns. The extensive tied zone is visible at a magnification of 250 X (Figure 19). The ease at which the quarter piece of the GFRP specimen GE-4 was opened indicates that interply delamination had previously occured.

4.4.2.   Macor fractography.

During fatigue cycling, Macor specimens typically fractured upon the initial contact of a load pin on the first cycle in a new loading sequence. Breakage always occured at a short span load pin, and initiated at the edge on the tensile side of flexure, along a polishing or grinding mark in the 'as-recieved' surface. These fractures were all due to accidental overloads.

Representative scanning electron micrographs of the fracture surface at the edge of the free surface and at about fifty microns from the tensile surface of three Macor specimens were taken. Specimen MA-2 fractured after 500 load cycles at 0.20 M.O.R. (Figures 20.a and b). Specimen MA-6 fractured after 1000 load cycles at 0.40 M.O.R. (Figures 21.a and b). The third specimen, MA-9, fractured after 2500 load cycles at 0.50 M.O.R. (Figures 22.a and b).

Edge-on micrographs at magnifications of 750 X show no recognizable evidence of fatigue cracking (Figures 20.a, 21.a, and 22.a). There is also no evidence of incremental fatigue cracking in the micrographs taken at about fifty microns from the tensile surface at 750 X (Figures 20.b, 21.b and 22.b).
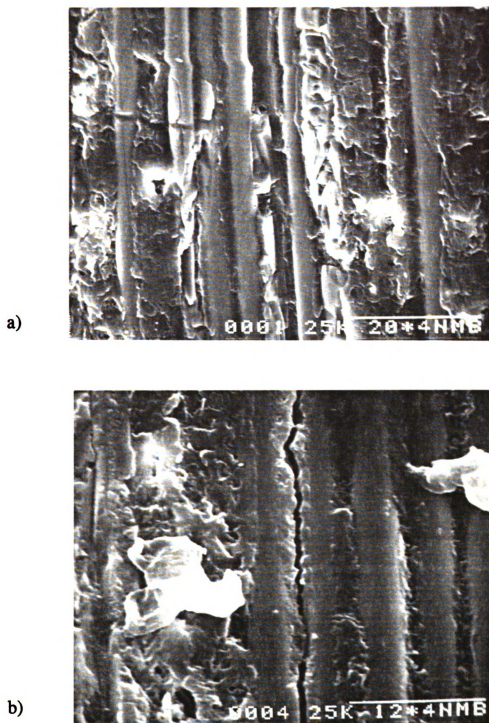
a)

b)

Figure 18. Scanning electron micrographs of the midplane shear crack (specimen GE-4) common to all GFRP fatigue specimens. a) evidence of multiple delaminations connected by transverse cracking, 185 X, b) typical shear crack, 300X.
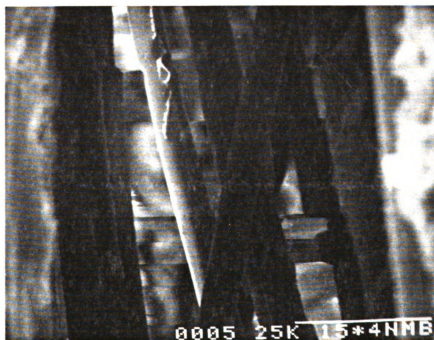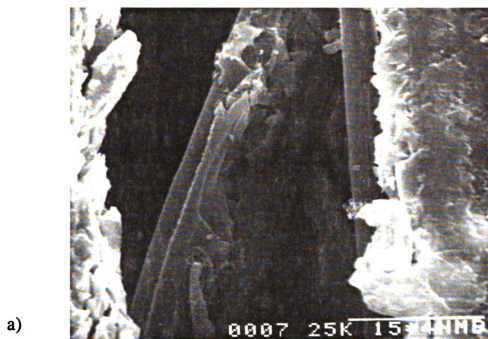
a)

b)

Figure 19. Scanning electron micrographs of the partially opened midplane crack of specimen GE-4, clearly showing the fiber bridged zone.
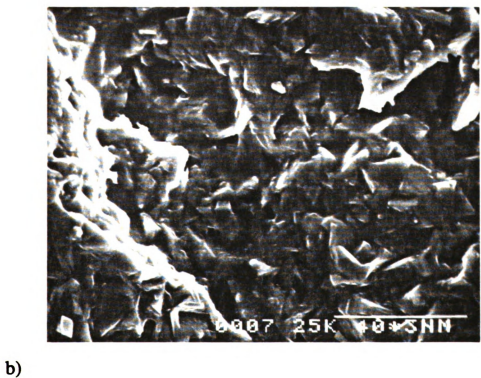Both micrographs taken as close to root of crack opening as possible.
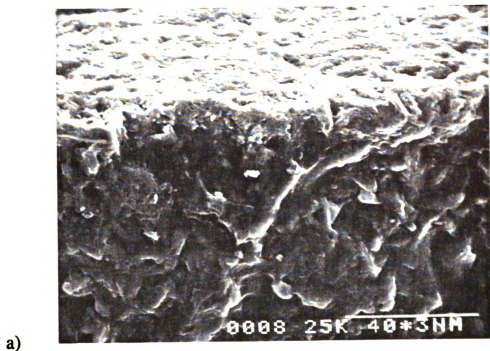
a)

b)

Figure 20. Scanning electron micrographs of the fracture surface of Macor specimen MA-2. a) view of fracture at edge of tensile face, 750 X, b) view of fracture near tensile surface, 750 X.
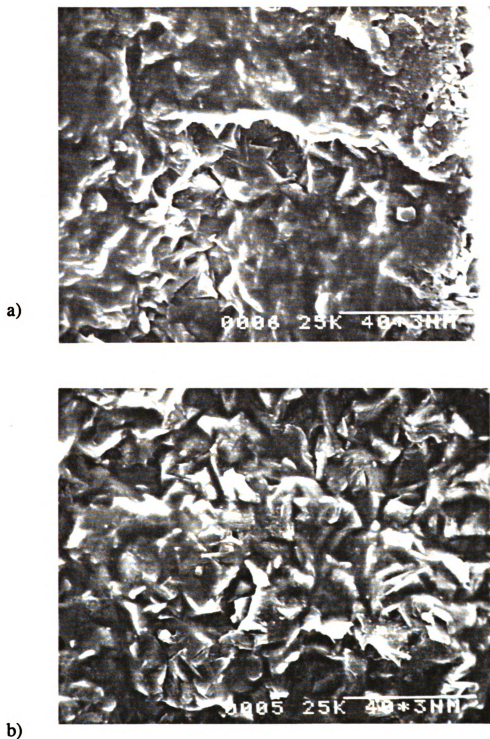
a)

b)

Figure 21. Scanning electron micrographs of the fracture surface of Macor specimen MA-6. a) view of fracture surface at edge of tensile face, 750 X, b) view of fracture near tensile surface, 750 X.
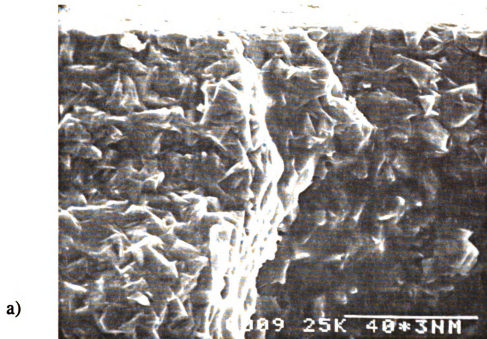
a)

b)

Figure 22. Scanning electron micrographs of the fracture surface of Macor
specimen MA-9. a) view at edge of fracture surface, 750 X,
b) view of fracture surface near tensile surface, 3000 X.

From the lowest to highest fatigue loads however, there is an increasing angularity and sharpness of mica platelet definition in the fracture surface morphology. The specimen with the lowest fatigue load appears to have the smoothest surface, indicating that fracture occured through the matrix phase of the microstructure, away from the mica platelets (Figure 20). The specimen that experienced the highest fatigue load shows sharply defined mica platelets, indicating that fracture occured along or closer to the mica platelet (Figure 22). The specimen subjected to the median fatigue load, shows fracture surfaces with an appearance less smooth as those of the specimen with the lower fatigue load, but less sharply defined as those of the specimen with the highest fatigue load Figure 21.

The trend in the appearance of the fracture surfaces (progressing from smoother to sharper morphology with increasing fatigue loads) may, however, be more a function of the maximum load applied to cause the fracture, possibly increasing the rate of fracture.

4.5.   Analysis of fatigue data.

4.5.1.   GFRP - AE analysis with and without load scaling.

4.5.1.a.   GFRP - AE analysis without load scaling.

When analyzing mechanical damage in terms of acoustic emission, one must consider and exploit all means and types of data analysis available. Without the ability to scale acoustic emission with its corresponding load, the identification of some signature of the various modes of damage would be highly valuable.

For the Macor specimen runs of MA-1 through the first 2500 cycles of MA-11, the capability to scale the AE with load was temporarily lost.

However, the intensity of the AE events as measured by counts, energy, amplitude, rise time or duration may be screened by setting a higher threshold for those parameters and analyzing the data above that threshold. Load scaling of AE was used by Lewis and Rice who also described the frictional emission level [5, 6].

By knowing the number of cycles at which the AE events occured, Lewis and Rice suggest that plotting the AE parameter of interest on the ordinate and the number of load cycles along the abscissa. This approach is fatally flawed, however, since AE bursts are broadened in their frequency distribution and attenuated with distance, as proven by Evans [35]. A distant pulse originating from crack damage may appear (to the transducer) as a pulse of lesser amplitude, but of longer duration and higher counts, etc. than an event that occurs very close to the transducer which may be due to frictional contact of existing crack surfaces. Thus, the use of a threshold is not a clear means of identifying AE sources, but only gives attention to the higher intensity events. A threshold to truncate or discriminate some AE data may perhaps be determined after understanding the damage that the specimen has experienced. This is still a somewhat subjective or emperical approach, in that the determination of a threshold is not a clearly indicated decision. However, even when looking into a thick fog, some nearby details are still visible, and to some degree represent the rest of the world shrouded in the fog. Thus, the plotting of AE counts versus load cycle is still of interest, and is described further in Section 4.5.2.1.

A reasonable description of a crack's acoustic signature must be independent of its distance from the transducer. Therefore, the parameters of energy, amplitude, counts and duration and rise time by themselves are not indicative of the acoustic event's character. The ratio of rise time to duration of an event may indicate the source's character. When a crack 'snaps' into existence, it may have an acoustic energy burst with a relatively short rise time

with respect to the duration of the ringing of the crack faces. Further, each type of damage may have a certain ratio of rise time to duration. This energy envelope profile model may lead to an 'n'-modal distribution.

Data from the Macor specimen MA-12 was analyzed for this possibility over the fatigue cycle range from zero to 100 load cycles, where most microcracking damage is expected to occur. A histogram of rise time divided by duration for each acoustic event (Figure 23) showed one possible division in the distribution of events. The occurance of acoustic events with rise time too short to measure may be indicative of cracking damage. The events with a measurable rise time appear to be normally distributed about a mean of about 0.2, and may be due to friction. This distribution did not indicate any further divisions. The characterization of an acoustic event as from cracking or friction may be made using the separate tests of 'notched beam' and 'direct pullout' respectively. The performance of these tests was beyond the scope of this study, and the search for a 'damage mode' signature was summarily abandoned.

A clear identification of an acoustic signature of specific damage modes is not possible, again supporting the analogy of the ringing of a large bell. You may hear the bell ring, but can not say with confidence what caused it to ring, from the sharp 'ping' of a clapper strike to the dull 'thud' of a person's fist.

4.5.1.b.   GFRP - AE analysis with load scaling.

Awerbuch [59-61] presented the AE analysis method of separating the acoustic emission information into narrower sections of the total load range.

During the cyclic loading of all three GFRP composite specimens, acoustic emission was detected at different rates and in different amounts in different regions of the load range. Segregation of AE data by load range
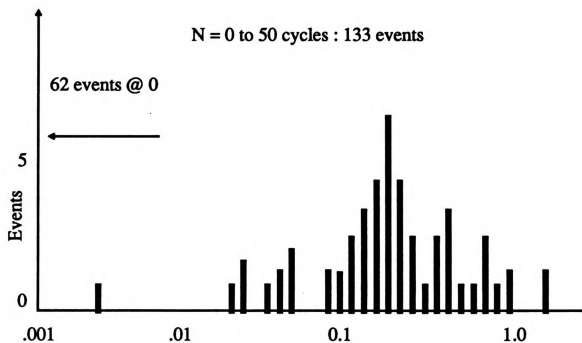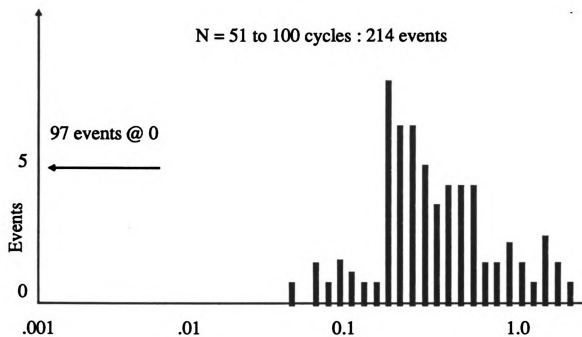
Figure 23. Histogram distribution of rise time divided by duration per acoustic event, for Macor specimen MA-12, zero to 100 fatigue cycles.

revealed several common features for all three load ranges tested. These common features will be discussed first, followed by specific differences. Acoustic emission counts from GFRP specimens GE-1 load cycled at 111.3 N (Figure 24), GE-2 load cycled at 155.8 N (Figure 25) and GE-4 load cycled at 200 N (Figure 26) are sorted by dividing the load range into ten equal parts. No other discrimination such as increased threshold was used.

4.5.1.c.   Common AE trends in GFRP composite.

4.5.1.c.1.   Load reversal effect.

For all GFRP specimens, acoustic emission counts accumulated much faster (with respect to fatigue load cycles) at the points of load reversal. Considering the results of the machine noise tests of Sections 4.3.1 and 4.3.2, the AE generated by the specimen near the point of load reversal during the regular fatigue test, must be interpreted as a mix of both specimen noise and system noise. The proportion of machine noise to specimen AE signal is not estimatable at this point, without further testing and is thus deemed beyond the scope of this study.

The load transition from increasing to decreasing was much more acoustically active than the load reversal from decreasing to increasing. As shown in Section 4.3, the proportion of machine noise and the specimen's AE signal cannot be determined, therefore only a qualitative discussion can be made. A significant amount of acoustic emission from the specimen is expected during load reversal, suggesting that the occurance of damage, whatever its mode, is more dependent on load reversal, rather than on the absolute maximum dynamic load (up to the point of catastrophic failure of the composite). The total number of counts at the load reversal points is dramatically skewed, but with no apparent trend between specimens at the
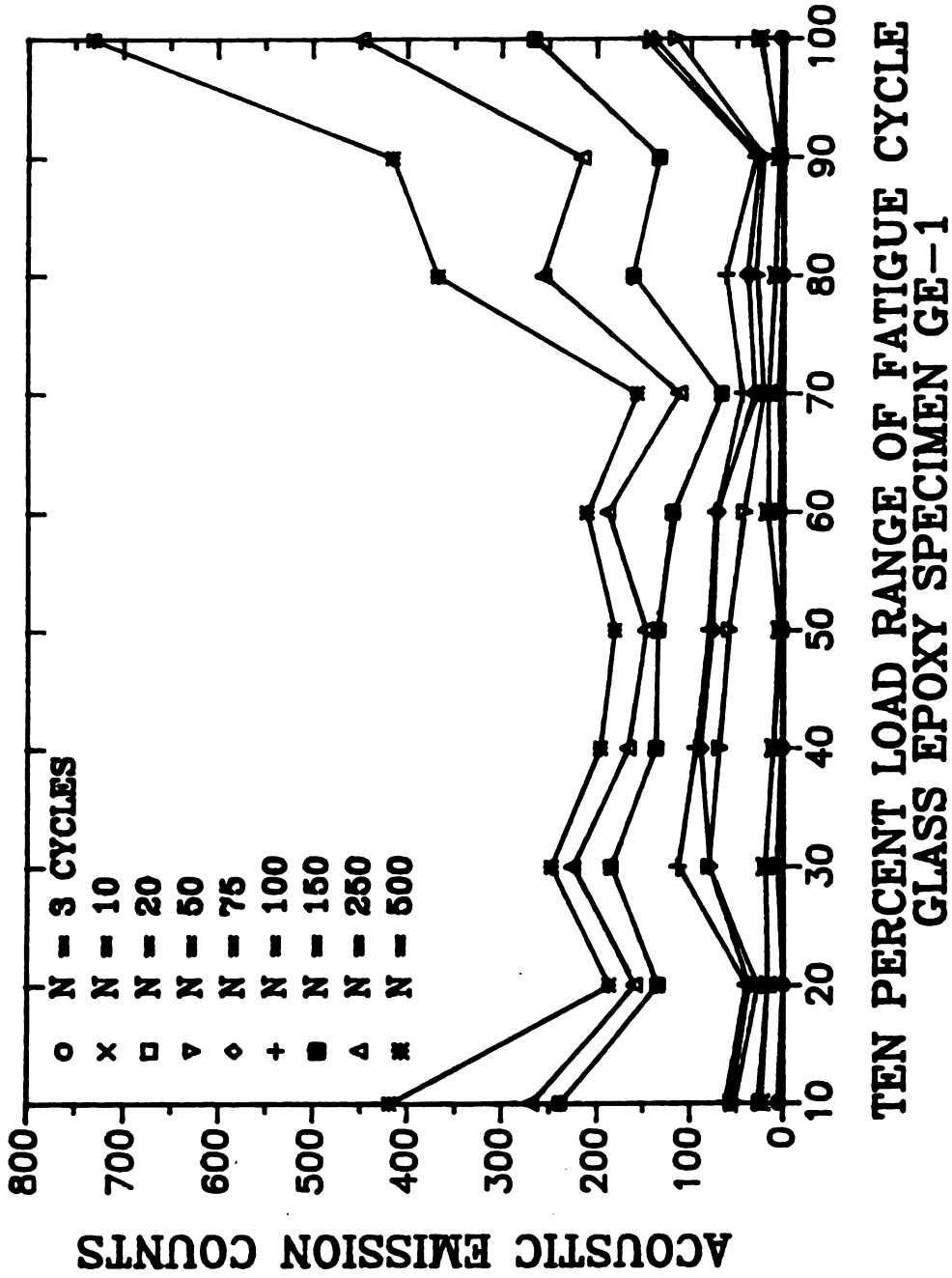
Figure 24. Acoustic emission counts sorted by load range for GFRP specimen GE-1, fatigue loaded with 111.3 N maximum dynamic load.
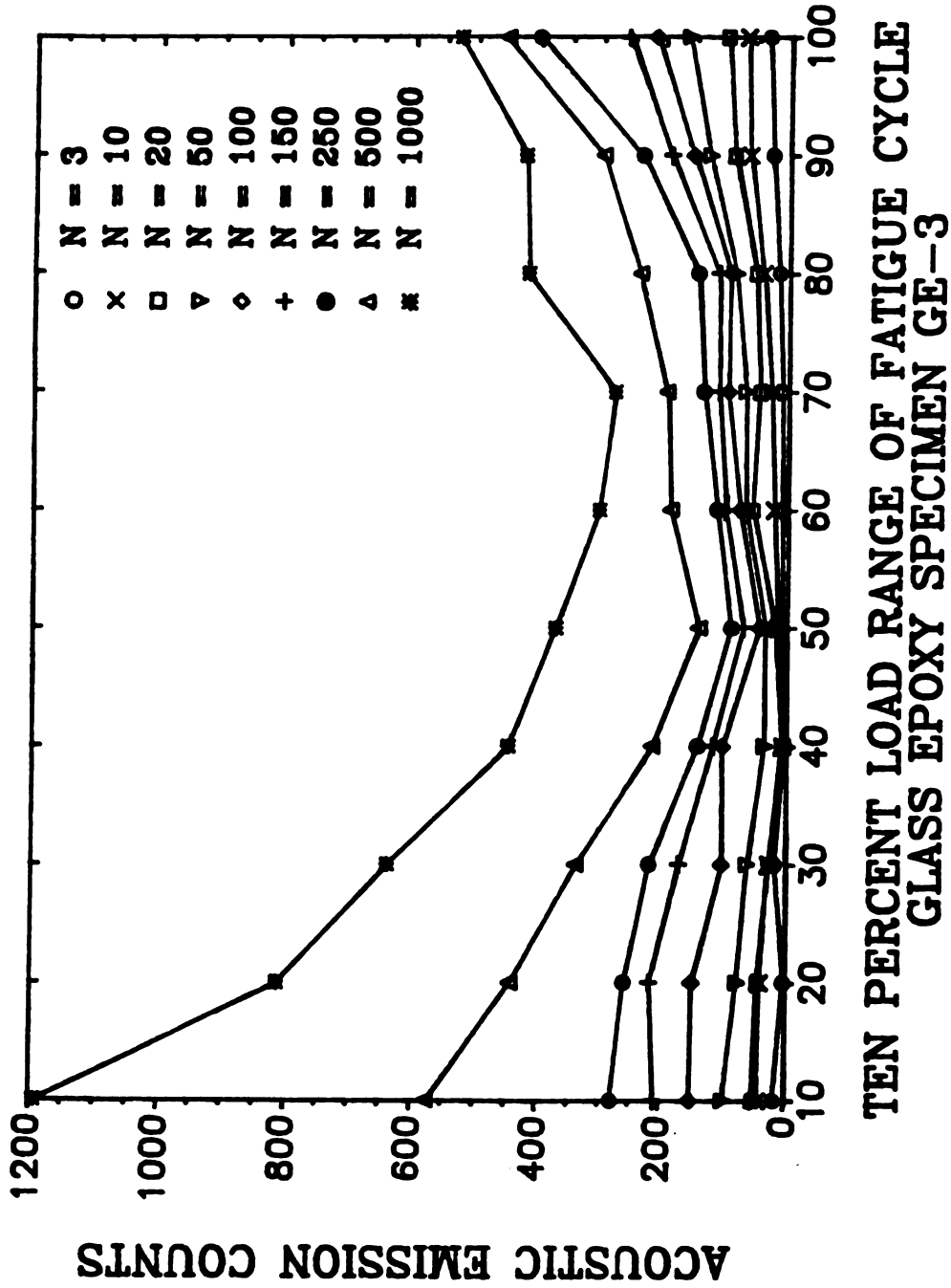
Figure 25. Acoustic emission counts sorted by load range for GFRP specimen GE-3, fatigue loaded with 155.8 N maximum dynamic load.
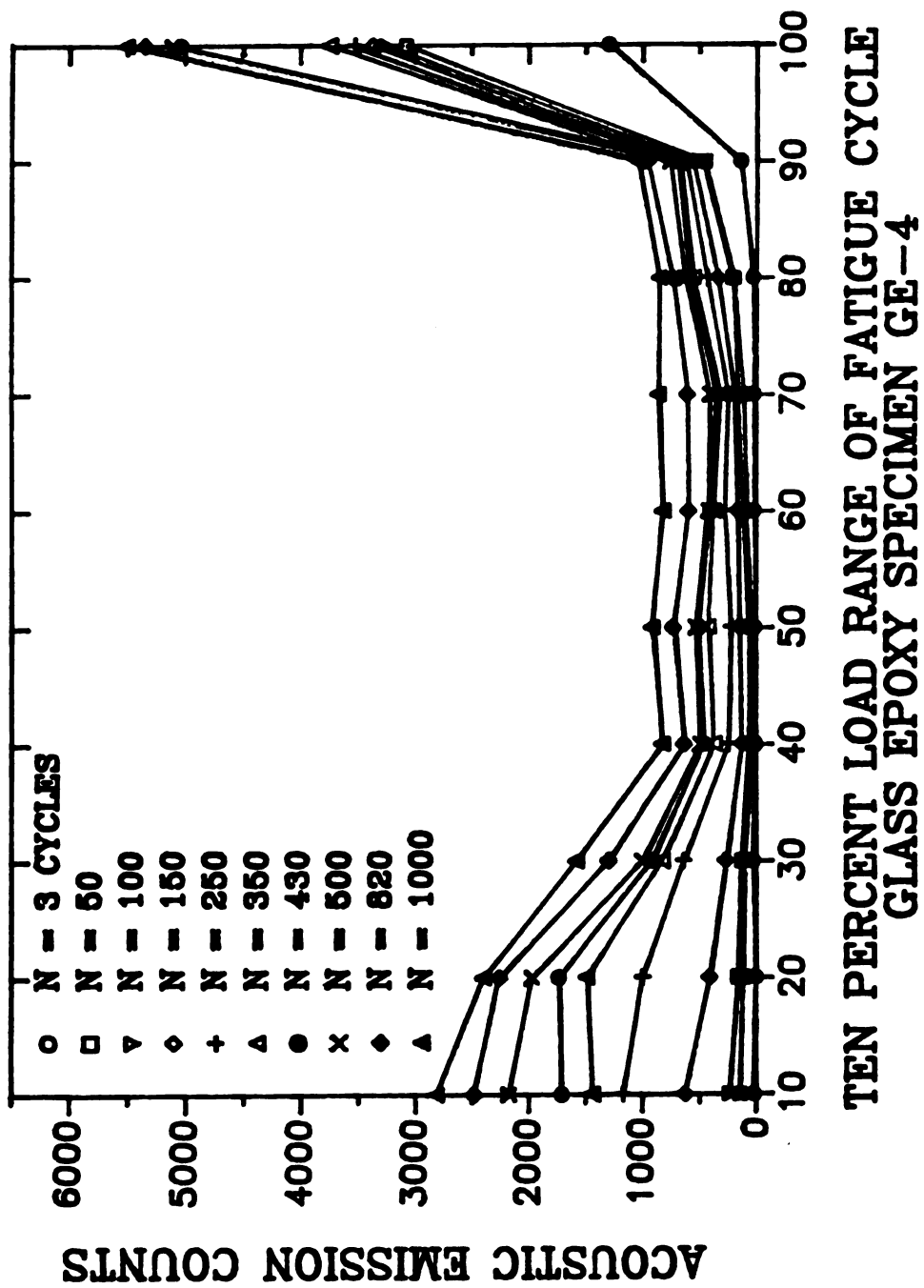
Figure 26. Acoustic emission counts sorted by load range for GFRP specimen GE-4, fatigue loaded with 200 N maximum dynamic load.

different maximum loads.

The variation in number of acoustic counts for nominally identical specimens is on the order of the square root of the number of counts [31]. Typical error bars may be estimated: for example, at 400 counts the first standard deviation is approximately 20 counts (5 percent variation), but for 5 counts, the error bar of one standard deviation must be 2.24 (45 percent variation), which is comparatively large. Therefore, at low numbers of counts or events, one cannot place a great deal of significance on any apparent trend.

The GFRP specimen with the lowest load (GE-1, at 111.3 N) showed more counts at the high end of the load range (Figure 24). At 500 load cycles approximately 730 counts accumulated. For the same number of cycles, the specimens that experienced maximum fatigue loads of 155.8 N (GE-3) and 200 N (GE-4), accumulated approximately 550 and 5500 counts respectively (Figures 25 and 26). The gross difference for the highest load specimen may be attributable to the exceeding of a strength threshold, where a larger amount of damage has occured.

4.5.1.c.2. Active zone - dead zone phenomena.

At particular load levels during the four-point bending fatigue cycle, AE events are generated with approximately the same characteristics, i.e. amplitude, counts, duration and rise time. Excluding the end regions, there are acoustically active zones where more AE is generated, and between them, acoustically quiet or 'dead' zones with very little acoustic emission generated. This behavior may imply the engagement of certain asperities in the mating faces of existing internal cracks during the load cycle. Acoustic emission during either loading or unloading may be a function of asperity geometry. A saw - tooth configuration may 'catch' on itself while loading in one direction,

but not in the other. The crack opening displacement likely also contributes to the depth of engagement, which would affect the amplitude, duration etc. of the AE burst.

At certain numbers of fatigue cycles (also described in the next few paragraphs), the dead and active zones are either more or less pronounced, suggesting a nonlinear evolution of damage with fatigue life.

In the very first few load cycles, all three GFRP specimen's AE / load range distributions appear quite similar. Three ranges of low acoustic activity (dead zones) are observed in approximately the same load ranges of 10 to 20, 30 to 40 and 80 to 90 percent of maximum load. This may suggest that the GFRP composite is similarly sensitive to the initial familiarization with load, regardless of the load's absolute value, within the limit of the material's breaking strength. At this low number of AE counts, the corresponding error bar (as the square root of the number of AE counts) is almost as large as the data and therefore this trend may be lost as more specimens are tested.

As fatigue life progresses, a large amount of AE activity is seen in varying load ranges (the active zones), as indicated by non-parallel lines on the plots of Figures 24, 25 and 26. This suggests that some limited damage occurs at various load levels and at various numbers of load cycles.

For the lowest load GFRP specimen (GE-1, Figure 24), four dead zones appear with some degree of activity between them, at 10 to 20, 40 to 50, 60 to 70 and 80 to 90 percent of maximum load. In the active zones,the evolution of AE with fatigue life is most pronounced, suggesting the occurance of damage for that part of the load range. The dead zones at 10 to 20 and 80 to 90 percent of maximum load are most prominent in this specimen, possibly lending support to the earlier evidence that machine noise is most sensitive to load reversals. In the load reversal regions, the AE count distribution appears skewed toward the high end of the load range by an end-range AE count of about 300 counts more than at the low end of the load range.

GFRP specimen GE-3 (Figure 25), fatigued at 156 N (9.5 percent M.O.R.) shows two or three dead zones that develop at different numbers of fatigue cycles. One dead zone starts at 30 to 40 percent of maximum load then shifts to the 40 to 50 percent load range at around 50 load cycles, remains there until about 500 load cycles, then shifts to the 60 to 70 percent load range in the last 500 cycles of fatigue life. A second dead zone of lesser prominence appears
between 60 to 70 and 70 to 80 percent of maximum load then also shifts to the higher load range of 70 to 80 percent at around 50 load cycles, then to the 80-90 percent range as the number of load cycles approaches 1000. The least prominent dead zone, at the 10 to 20 percent load range disappears after the first 10 load cycles. The overall AE count distribution for specimen GE-3 is skewed toward the low end of the load range by about 650 counts.

Specimen GE-4 (Figure 26), experiences significantly more damage than specimens GE-1 and GE-2, as evidenced by the high number of AE counts observed across the load range. Load reversal AE is especially skewed toward the high end by about 2700 counts, approximately double the number of AE counts observed at the low end of the load range. Since system noise detected at the specimen was shown to not increase with load (Section 4.3.2), it can be inferred that the specimen produces substantial AE (and damage) at the high end load reversal.

The absolute number of AE counts at the high end of the load range through 500 load cycles for specimen GE-4 is larger than the number of counts observed for the specimens of lower maximum loads. This difference varies by a factor of about seven for specimen GE-1 and about eleven for GE-3. This does not appear to support a trend.

For specimen GE-4, one long dead zone exists through the 40 to 90 percent load ranges (Figure 26). The lower ranges from 10 to 30 percent of maximum load increase between 150 to 350 load cycles, suggesting that

significant damage has occured in that load range during those load cycles.

Acoustically dead and active zones may result from the frictional contact of asperities during flexure. During the experiment, it was frequently observed that for several to 20 or 30 consecutive load cycles, acoustic events were consistently observed either on load up or down, but rarely both. The numerical data often showed that successive events occured at approximately the same load (to within a few tenths of a volt on the main parametric scale, which represented the load signal from the Instron).

A second mechanism for acoustically dead and active zones varying with maximum load may be an arrest and progression sequence of damage that occurs periodically during loading. At higher maximum loads, with the specimen being taken directly to the higher maximum load, there is certainly more bending deflection. The larger deflection likely causes a larger amount of damage and possibly reduces any ability of the material to arrest and release the crack front. Factors which may affect such a mechanism may include: (1) sensitivity to strain energy release rates, (2) changes in stress intensity, (3) initial loading history or (4) a critical load which, when exceeded, reduces the damage tolerance of the material.

4.5.2.   Macor fatigue analysis.

4.5.2.a.   Macor AE analysis with load scaling.

Analysis parallel to that done with the GFRP specimens was performed on the data obtained from tests with the Macor specimens. Similar trends appeared in the Macor data, but with subtle differences.

4.5.2.1.a.   Macor specimen MA-12.

Macor specimen MA-12 was fatigued to 5000 load cycles without failure.   AE data was scaled with load.   Fatigue loading was run at the highest percentage of breaking strength, at which the Macor would survive flexure.

Three quarters breaking strength (0.75 σ_f) worked out to an absolute maximum load of 86.2 N.

The AE counts accumulated over 5000 load cycles were divided into ten equal load ranges (Figure 27).   With respect to the evidence of system noise, from Sections 4.3.1 and 4.3.2, there is a very large amount of AE at the point of load reversal from decreasing to increasing load.   The distribution of AE counts is markedly skewed toward the low end of the load range. About 7300 counts accumulated in the zero to 10 percent range after 5000 load cycles, while about 2200 counts were observed in the highest load range of 90 to 100 percent maximum load.   This is a difference of a factor of about 2.5. The fact that the AE distribution is skewed toward one end of the load range does not indicate the presence of a trend.

The most variation in AE counts between load ranges was observed during the first few load cycles.   From then onward, the end regions, where load reversal occured, were the dominant AE production ranges.   A relatively major amount of damage occured in the range of 60 to 70 percent of maximum load.   The parallel lines about the small peak at the 60 to 70 percent range indicate that the load range became less active after the initial fifty load cycles. Where one load range produces more AE than another, the result is seen graphically as a further displacement in the AE count direction.

The minor AE peak at the load range of 60 to 70 percent, occurs at an absolute load of about 55.8 N.   The 60 to 70 percent load range in MA-11 showed no hint of the same level of emission, nor did MA-11's level of
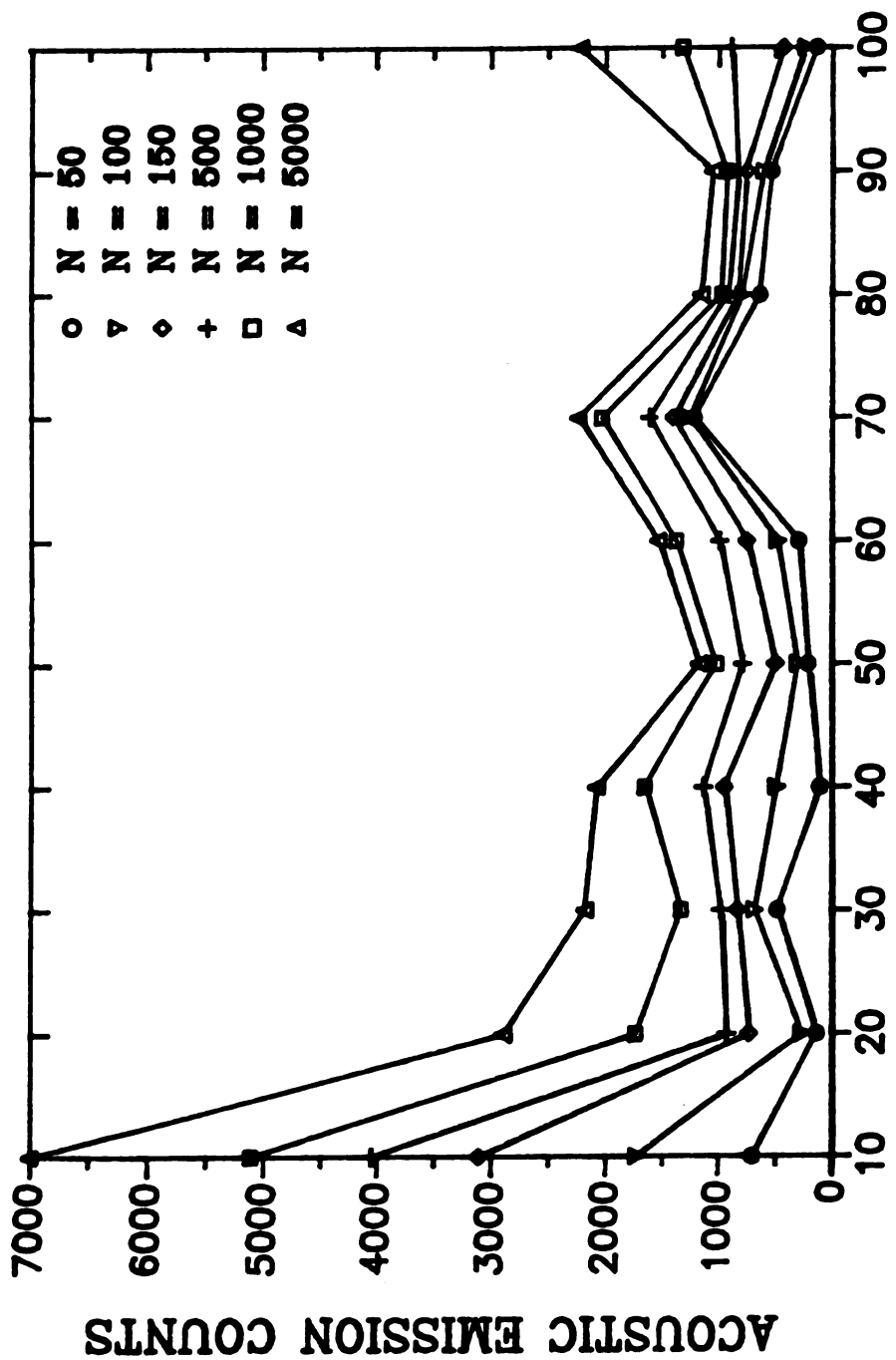
Figure 27. Acoustic emission counts sorted by load range for Macor specimen MA-12, fatigue loaded with maximum dynamic load of 86.2 N, 0.75 modulus of rupture.

emission at maximum load appear at the same absolute point in MA-12. Therefore, the exceeding of a strength threshold is not suspected. This evidence supports the significance of the load reversal as the principle source of damage generated acoustic emission.

4.5.2.1.b.   Macor specimen MA-11.

This specimen was cyclically loaded to 0.65 σ_f (an absolute maximum load of 88.6 N). Lacking the acoustic history prior to the 1000 load cycle mark, it is still observed that the AE from 1000 to 5000 load cycles is as markedly skewed to the low end of the load range as was specimen MA-12. In the lowest load range, from 1000 to 5000 load cycles, specimen MA-12 produced about 2000 AE counts, while in the same range, MA-11 produced nearly 7000 AE counts. This difference is in apparent contradiction to the intuitive expectation of more counts for a higher maximum stress (as a higher percentage of rupture modulus). At the high end of the load range, both specimens produced approximately 2000 AE counts.

4.6.   Internal friction and Young's modulus change over fatigue life.

The standard procedure for the determination of internal friction (Section 2.1.1.a.), had to be slightly modified in order to continue analysis of the GFRP composite. Damage to the unidirectionally reinforced GFRP composite became increasingly inhomogeneous as the fatigue experiment progressed. The inhomogeneous damage made the use of Wachtmann and Tefft's nonlinear least squares curve fitting routine impossible, with correlation coefficients less than 0.95 (actually sometimes down to around

0.4). Therefore, internal friction readings were taken at only two locations, at 0.11 and at 0.33 normalized distance (n.d.) from the end of the bar. The reading at 0.11 n.d. lies outside the flexural node and out of the regions of flexural stress and shear stress imposed by the fatigue loading. Two locations were chosen to monitor the relative changes in Young's modulus and internal friction, and assumes that the effects of fixturing remain constant.

An unexpected shear crack developed in the midplane of each GFRP specimen, initiating in the short load span (constant moment) area, and progressed throughout the entire specimen. The shear crack may account for the large differences in internal friction, measured at the two locations.

The estimation of the extent of crack progression could not be more accurately measured beyond using an unaided eye, and a metric caliper. Transmission X-ray or ultrasonic methods such as C-scan would have been much more accurate, and possibly could have provided a good correlation of crack length or area with the changes in internal friction and Young's modulus.

4.6.1.   Internal friction and Young's modulus versus load cycles for GFRP specimen GE-1.

Internal friction versus fatigue load cycles for GFRP specimen GE-1 (Figure 28) shows a large peak at about 100 cycles, as measured at 0.12 n.d. from end of bar. The corresponding data for 0.32 n.d. was estimated between 75 to 150 load cycles, based on the similar plots for specimens GE-3 and GE-4.

Comparing Figures 28 and 29 (specimen GE-1's variation of internal friction and Young's modulus respectively, with fatigue load cycling), there is generally an inverse correspondence with changes of Young's modulus and internal friction. Initially, from zero to 3 load cycles, there is an inverse response between Young's modulus and internal friction, then as modulus
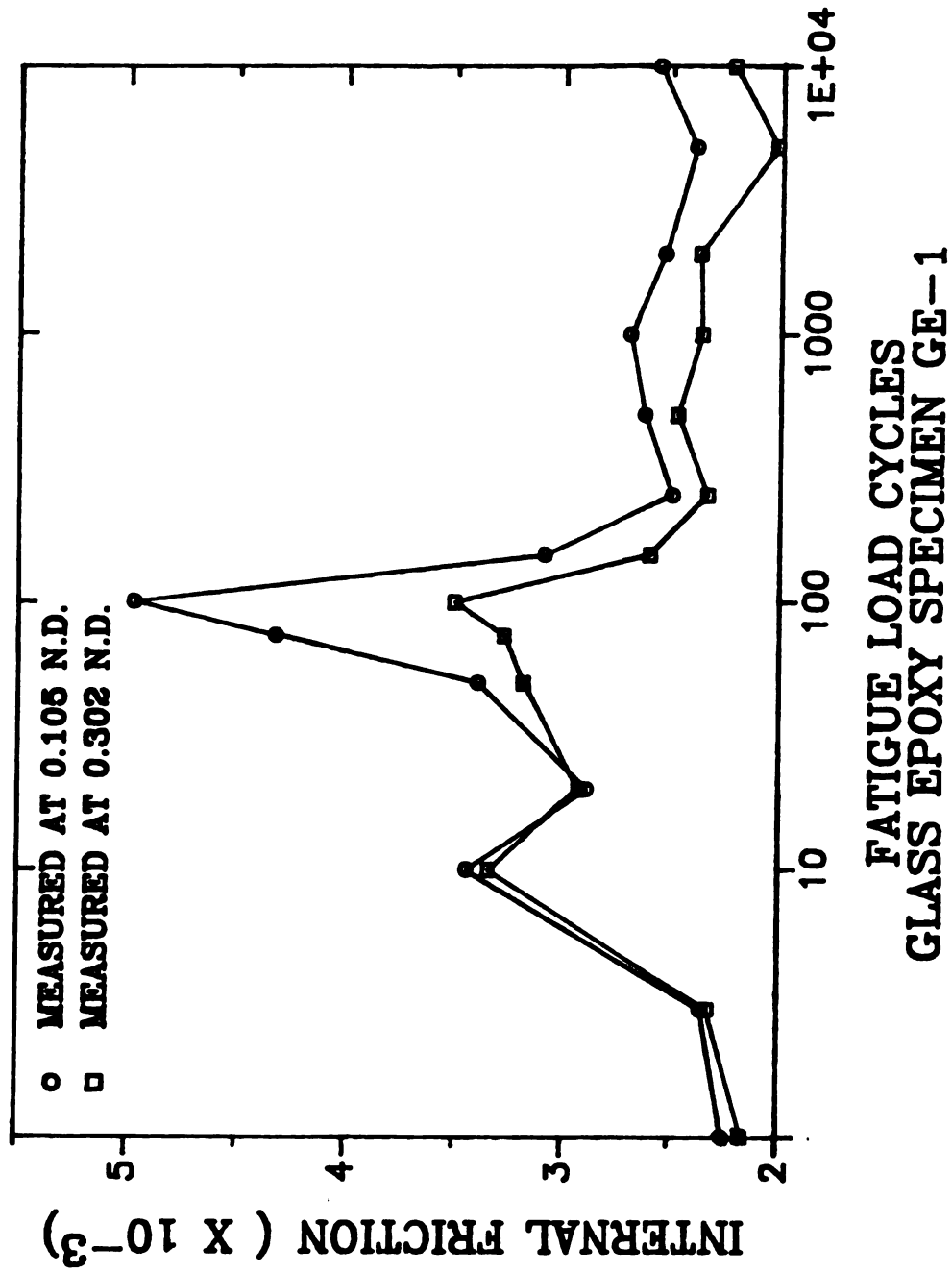
Figure 28. Internal friction versus fatigue load cycles for GFRP specimen GE-1, maximum dynamic load of 111.3 N. Values on the internal friction axis represent the specimen's undamaged state.
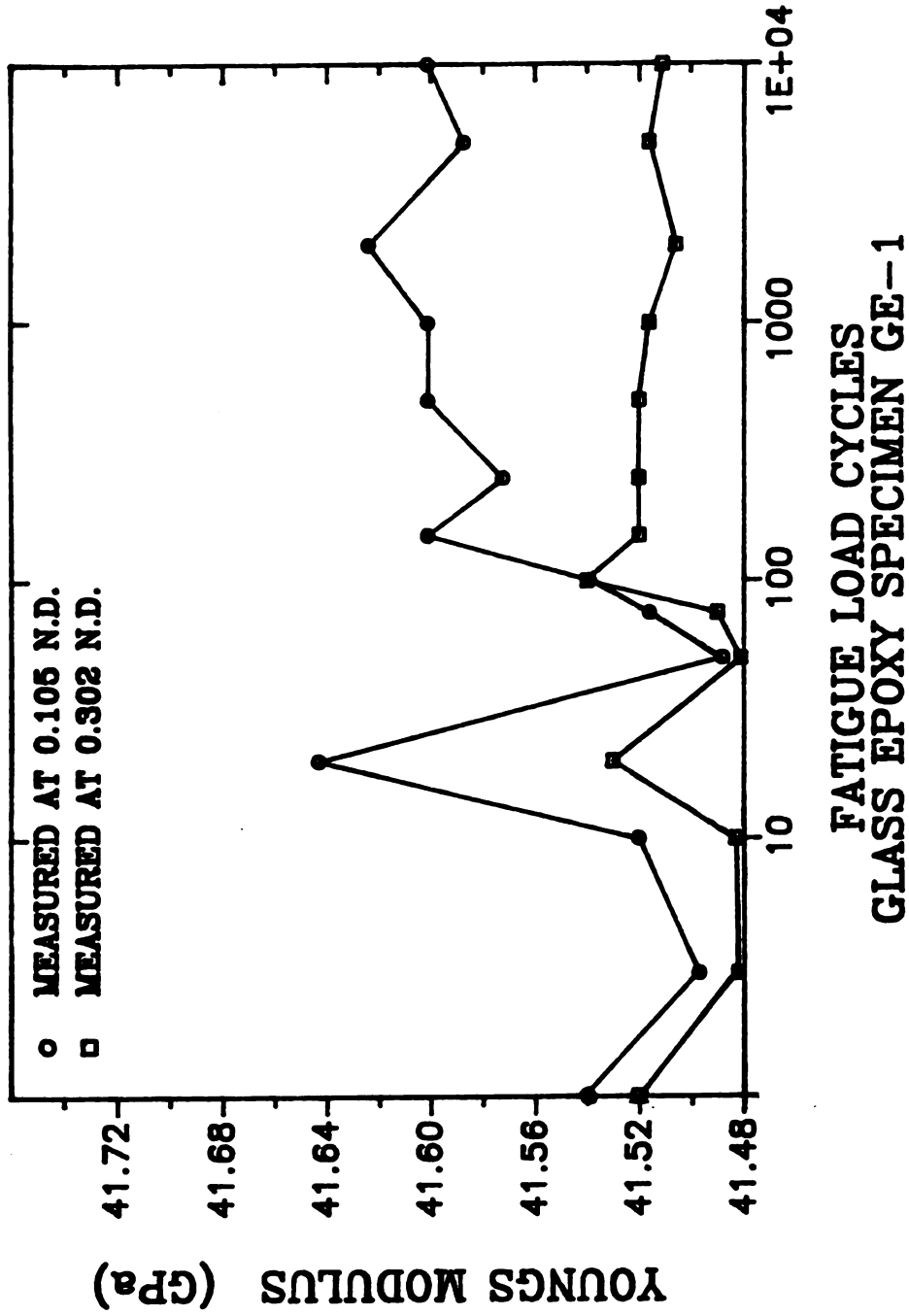
Figure 29. Young's modulus versus fatigue load cycles for GFRP specimen GE-1, maximum dynamic load of 111.3 N. Values on the Young's modulus axis represent the specimen's undamaged state.

increases between 3 and 20 load cycles, internal friction goes through a local maximum. A maxima in Young's modulus (Figure 29) occurs at about 20 load cycles, accompanied by a significant local minimum on the internal friction (Figure 29) at the same number of load cycles. As the major peak of internal friction blooms and fades from the minimum at 20 cycles through its maximum at 100 cycles then back down to its next local minimum at 250 cycles, the correspondence of Young's modulus goes through first a minimum at 50 cycles then a maximum at 150 cycles then back to another minimum at 250 cycles. From 250 load cycles onward, there appears to be an approximately direct correspondence between the two plots. However, the changes in Young's modulus measured after 250 load cycles do not vary by much more than the measurement uncertainty, thus precluding much strength to this particular observation.

The relative correspondence between internal friction and Young's modulus suggests a three regime damage activation process. The progression of correspondence appears to be from somewhat proportional, through an inversely proportional regime with some deviations, then back to approximately proportional. This three regime behavior suggests a correspondence with: (1) initial damage of matrix cracking transversely to the fibers, (2) between 3 and 10 cycles, the shear crack initiates, and from 10 through 250 cycles the shear crack grows to the ends of the specimen and (3) with further load cycling, continued matrix cracking and fiber pullout and breakage may occur. Rough measurements indicate that the shear crack passed the measurement suspension points between 50 to 200 cycles.

From the data and the specimen configuration, it is interesting to note that in both Figures 28 and 29, there are five local minima and maxima, and also five points of interest on the specimen. As the shear crack grows, it first passes the short span load pins, then the suspension points at 0.32 n.d., the long span load pins, then very closely comes the fundamental flexural nodes,

the suspension points at 0.12 n.d, then finally the free ends of the specimen. The close proximity of the fundamental flexural node and the long span load pin was not planned, but may have had a strong influence on the sonic resonance response. The passage of the shear crack across the long span load pin and the flexural node probably occured during load cycles from 20 to 150. This observation is based on rough measurements and the slope reversals of the plots in that span of load cycles and suggests some influence of the shear crack on the measured values of internal friction and Young's modulus.

4.6.2. Internal friction and Young's modulus versus load cycles for specimen GE-3.

The most prominent feature in internal friction and Young's modulus for GFRP specimen GE-3 (with maximum dynamic load of 15.88 kilograms) is the large peak centered at about 260 load cycles (Figures 30 and 31 respectively). Sonic resonance readings were possible for both suspension locations on this specimen, at the number of fatigue cycles in the range of the peak, but were not possible early in the fatigue life of the specimen for reasons unknown. The value read at the nearest usable position to 0.32 n.d. is plotted for the sake of comparison in the low cycle range. Note that both internal friction peaks are centered at about 260 cycles. Both curves tend to rise monotonically after bottoming out after the large peak. This response may be attributable to uniformly increasing damage (no further major events) with further load cycling after the shear crack has run out to the ends of the bar.
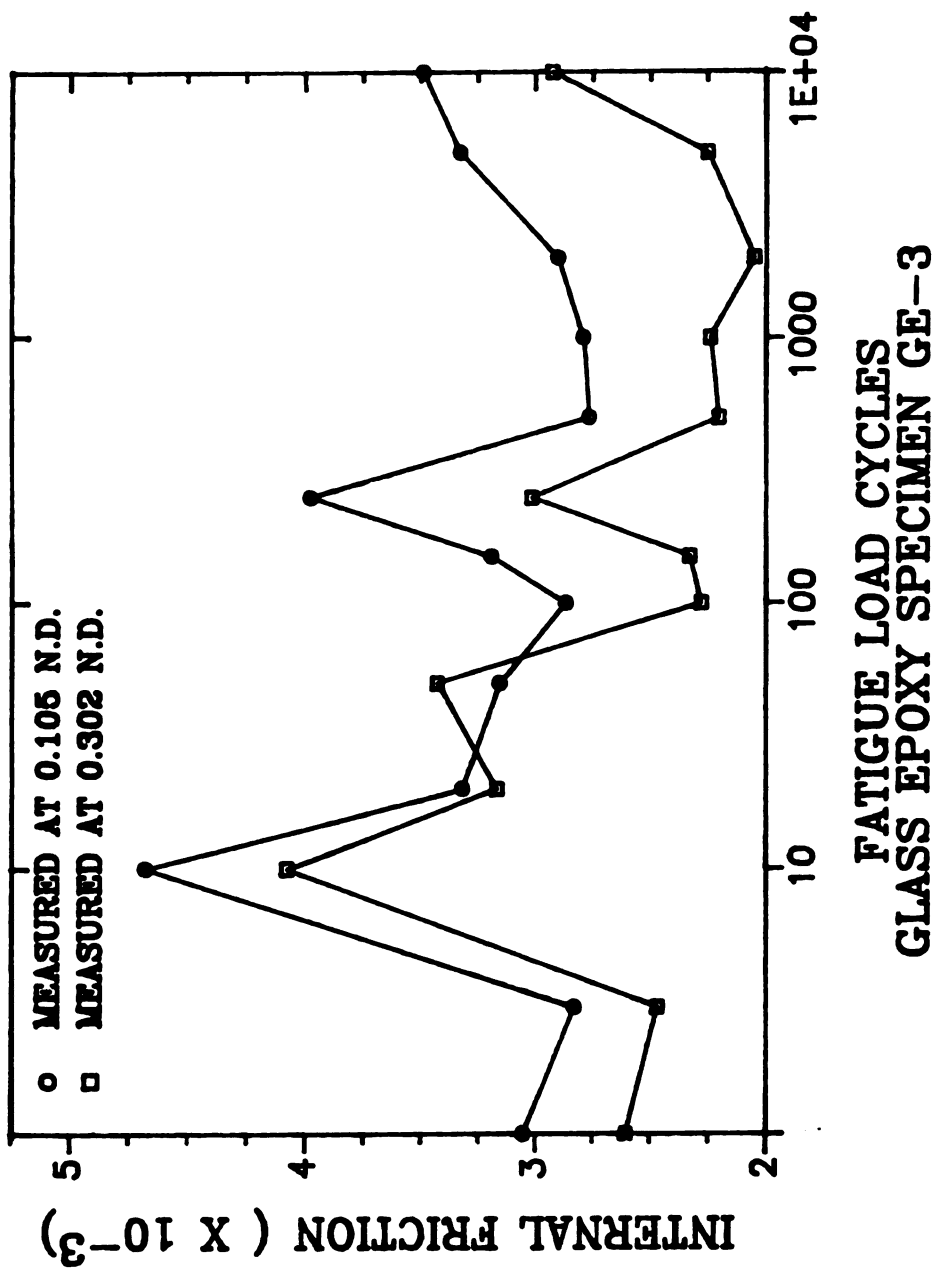
Figure 30. Internal friction versus fatigue load cycles for GFRP specimen GE-3, maximum dynamic load of 155.8 N. Values on the internal friction axis represent the specimen's undamaged state.
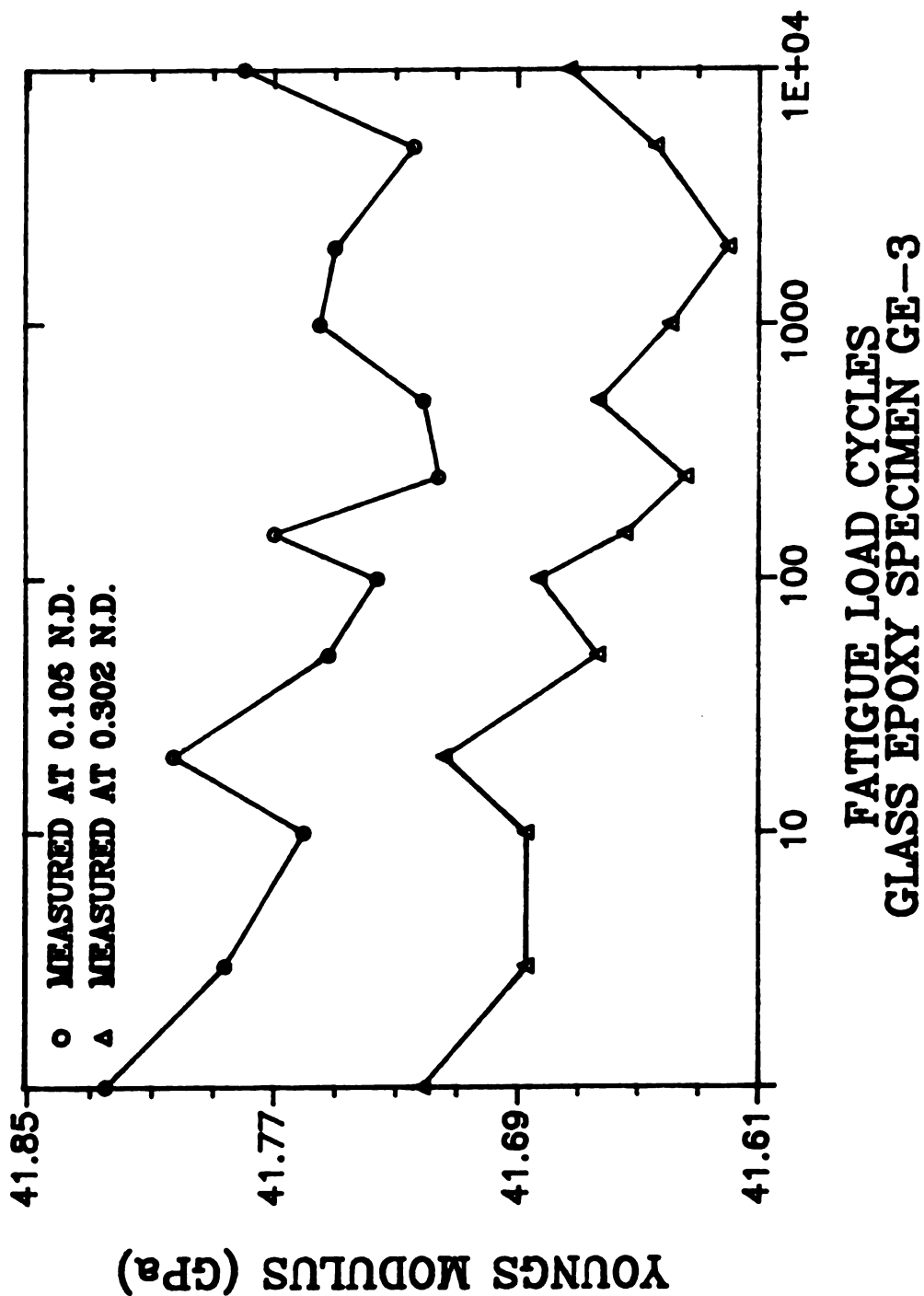
Figure 31. Young's modulus versus fatigue load cycles for GFRP specimen GE-3, maximum dynamic load of 155.8 N. Values on the Young's modulus axis represent the specimen's undamaged state.

4.6.3. Internal friction and Young's modulus versus load cycles for specimen GE-4.

Internal friction versus the number of fatigue load cycles for GFRP specimen GE-4 (maximum dynamic load of 200 N), shows a large peak, centered at about 380 load cycles (Figure 32). In this specimen, the peak measured at 0.32 n.d. rises high above that measured at 0.12 n.d. This may indicate that the two peaks trade places based on maximum fatigue load. Further experimentation with other values of maximum load may clarify the possibility.

Young's modulus versus load cycles for GFRP specimen GE-4 (Figure 33), shows a similar variation as that of specimens GE-1 and GE-3. The curve for 0.012 n.d. deviates from a monotonic decrease more than the curve for 0.32 n.d. measurement position, largely due to the smaller error bars for the 0.012 curve.

4.7. Peak analysis on plots of internal friction versus number of load cycles for GFRP specimens.

The location and full width at half maximum of peak (as number of fatigue cycles) were determined for the most prominent peak from the plots of internal friction versus number of fatigue cycles for the GFRP specimens used in the experiment.

Both peak measures show a linear or nearly linear relation (Figure 34) with respect to the maximum stress used for fatiguing. This behavior suggests that the two trends may be in the nature of the material.

Linear regression analysis showed the peak location to be the most linear. The specimen that experienced the lowest load saw the peak occur soonest in its fatigue life. The specimen that experienced the highest load saw
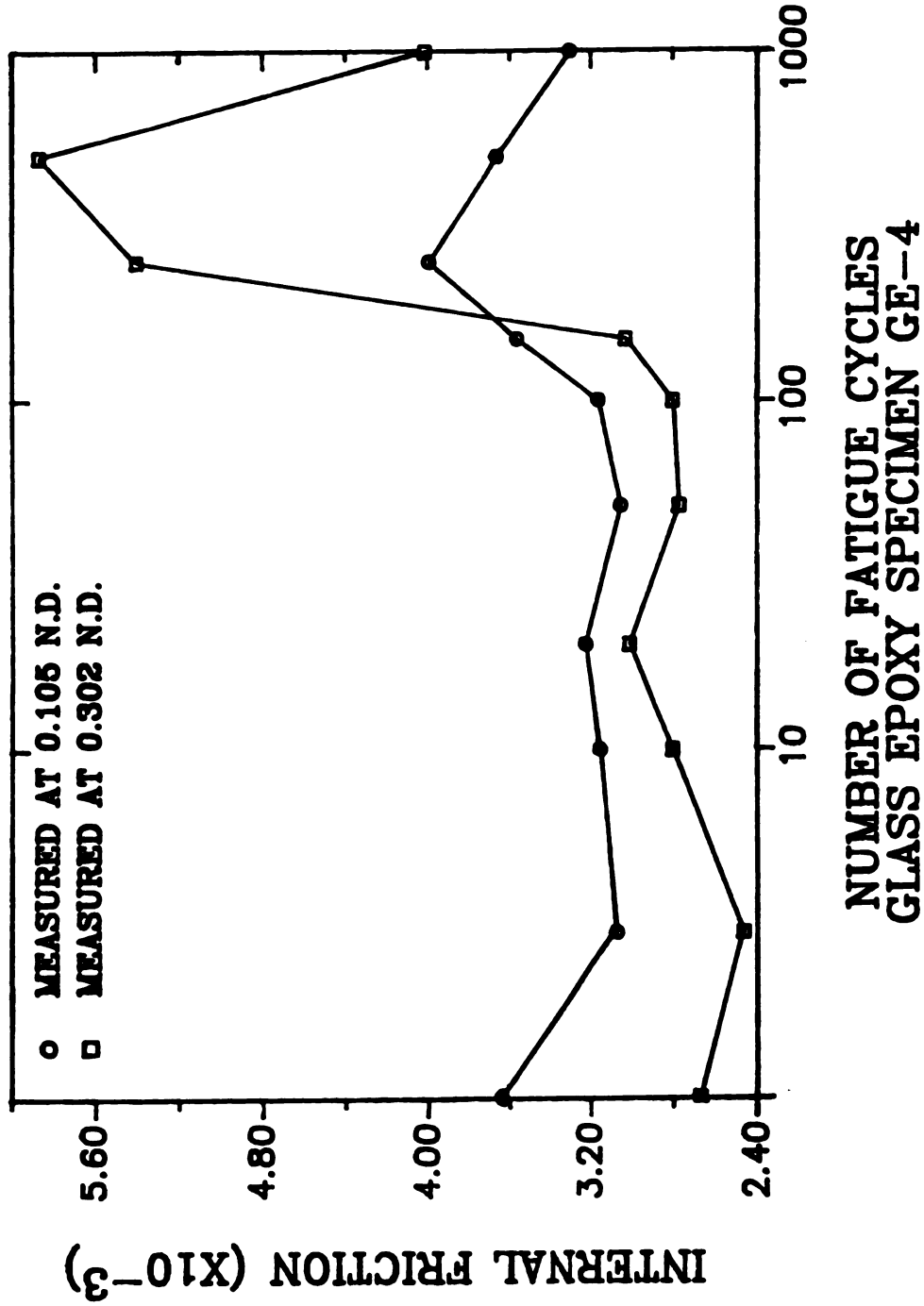
122

Figure 32. Internal friction versus load cycles for GFRP specimen GE-4, maximum dynamic load of 200 N. Values on the internal friction axis represent the specimen's undamaged state.
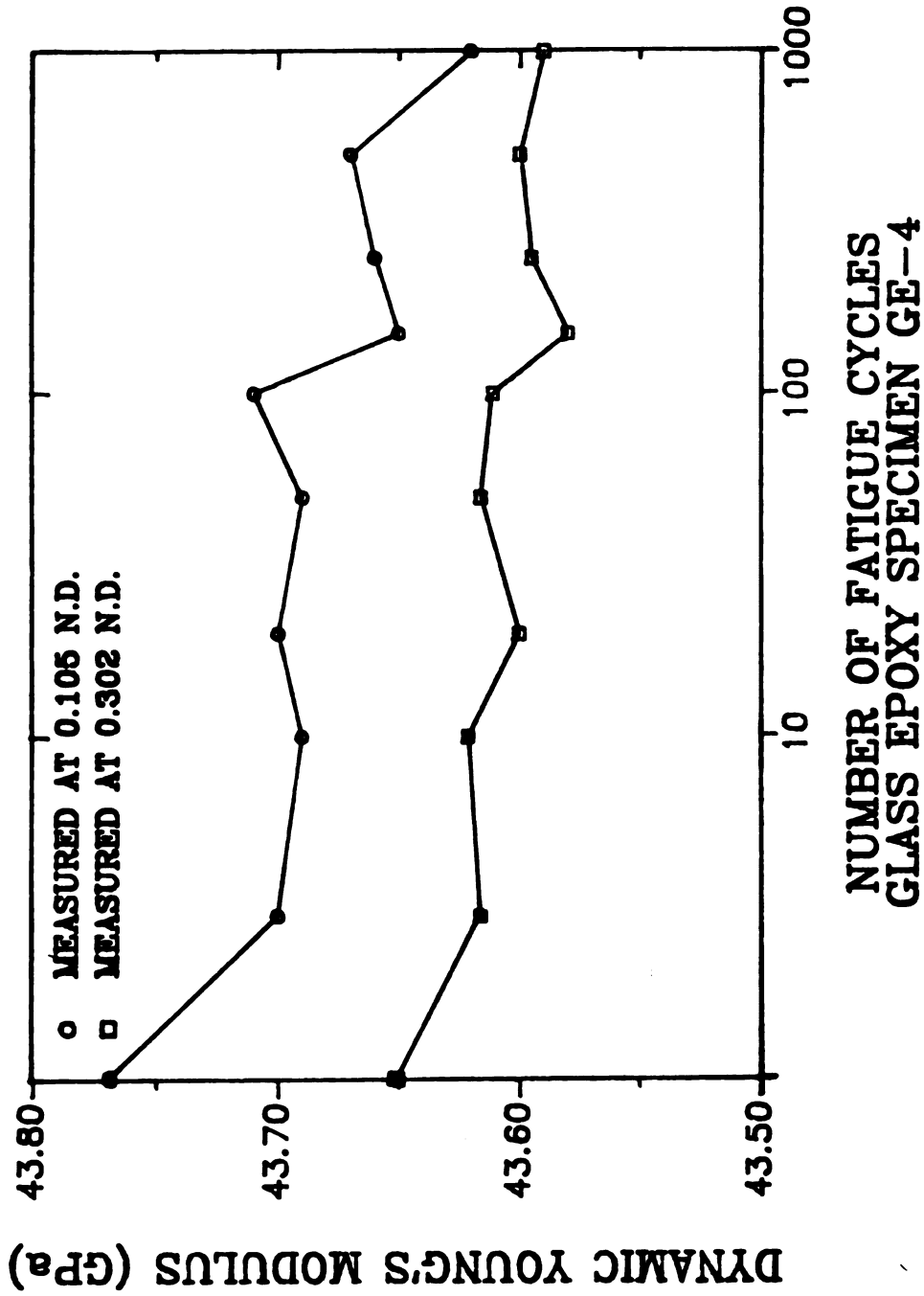
Figure 33. Young's modulus versus fatigue load cycles for GFRP specimen GE-4, maximum dynamic load of 200 N. Values on the Young's modulus axis represent the specimen's undamaged state.
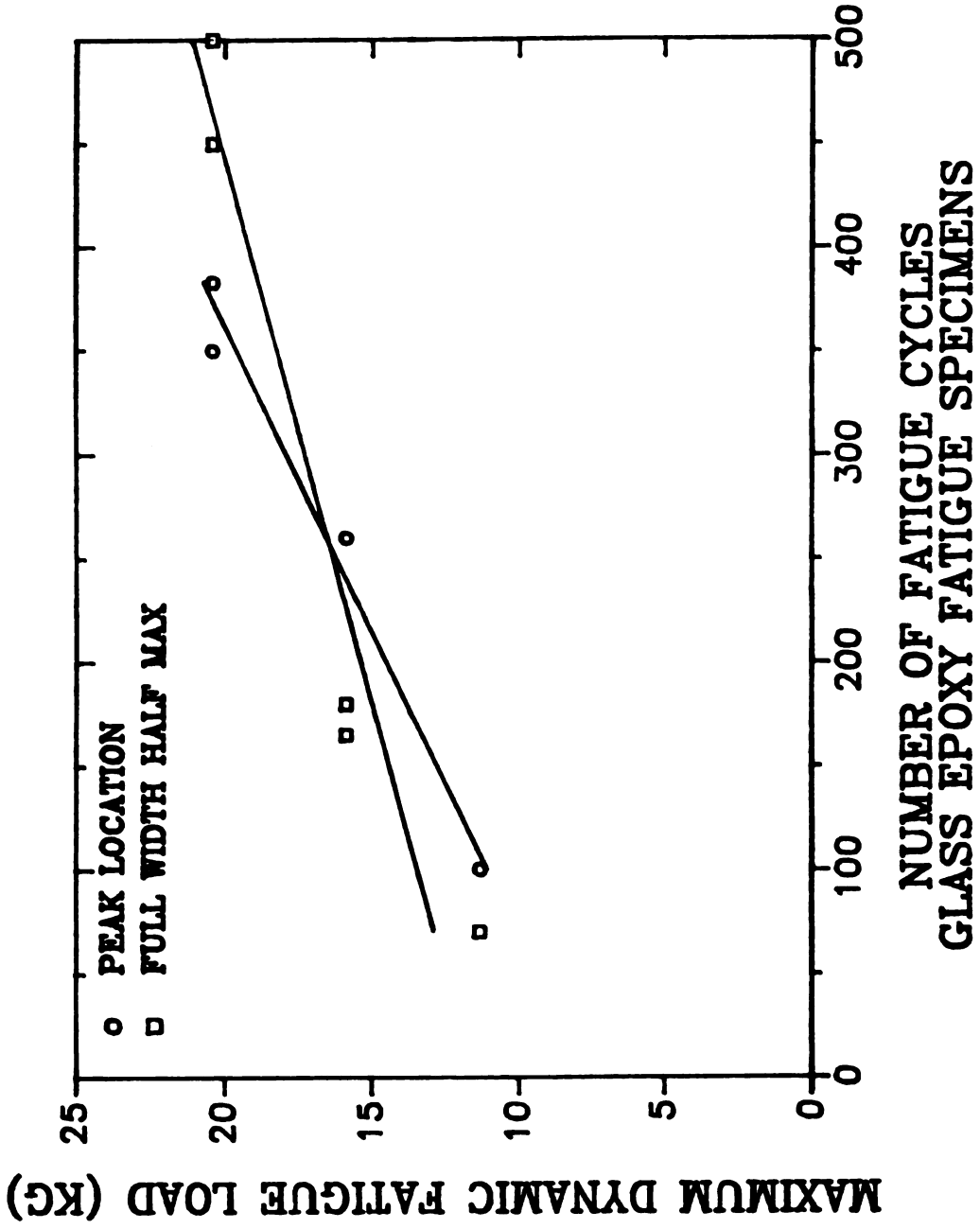
Figure 34. Data from peak analysis of major peaks in internal friction versus load cycles for glass epoxy specimens GE-1, GE-3 and GE-4.

the peak occur the latest in its fatigue life. This trend at first seemed counterintuitive, but it was compared to the effect of strain hardening in metallic alloys. This analogy certainly implies that the GFRP composite gets harder or stronger with fatigue, but the fact that the composite also appears to periodically lose strength is apparently contrary to previous work showing that GFRP composites may increase or decrease strength with strain, but not both during the same test [55-57]. The mathematical relations that describe the effect in metals may be a useful model as a starting point in further analysis of the effect in the GFRP composite. Further experimentation is necessary to determine if the properties of Young's modulus and internal friction are behaving in a clearcut trend.

The full width at half maximum also increased with maximum stress on the specimen, with the curve approaching the fatigue cycle axis at lower stresses. As the maximum dynamic load is reduced, the peak narrows, and at higher maximum loads, the peak widens.

The indication of a maximum load axis intercept suggests that below approximately 2 percent of rupture modulus (M.O.R.), there will not be a prominent peak in internal friction, which is the case for GFRP specimens fatigued at higher loads.

GFRP specimen GE-5, tested at a maximum load of 22.3 N (1.7 percent of M.O.R.), showed no evidence of a maxima of internal friction. This supports the trend of a decreasing number of load cycles for both peak location and peak width. If one makes the assumption that there is a hint of a peak in the data measured at 0.11 n.d., and that it appears to occur at about 30 to 50 load cycles, it can be suggested that the peak location curve approaches or intersects the fatigue cycle axis at lower maximum stresses.

It is reasonable to assume that for no load cycles, there will be no change in physical properties. Since the data for the higher fatigue load specimens falls into a nearly linear relation, and would indicate an intersection

with the ordinate, the existence of a 'damage nucleation' regime seems possible. This regime is where the data point for specimen GE-5 falls, further supporting the existence of the downward tail. It is further suggested that there may be a fatigue limit, where no damage occurs below a certain stress (as a fraction of M.O.R.), for any number of load cycles.

4.8. Maximum changes in Young's modulus versus load fraction of rupture strength.

Young's modulus data from all specimen runs was analyzed for the maximum overall change (Tables 3.a through d, pages 85 through 88).

It was noted that for most data, grouped by material and by physical property, a trend of increasing maximum change with increasing maximum fatigue load can be seen. The trend was most clear for the Macor specimens. Young's modulus, measured at 0.075 n.d., was plotted as maximum change in Young's modulus versus maximum load as fraction of M.O.R. (Figure 35).

Linear regression analysis, for this data set, gave the relation

$$E(Y|x) = -0.01023 + 0.002037(x) \qquad (50)$$

where

$E(Y|x)$ = expected variation in Young's modulus, given the percent M.O.R. of fatigue load

Y = Young's modulus

x = percent M.O.R. fatigue load.

For both Young's modulus and internal friction, comparison of the maximum changes (Δ and percent change columns of Tables 3) with possible
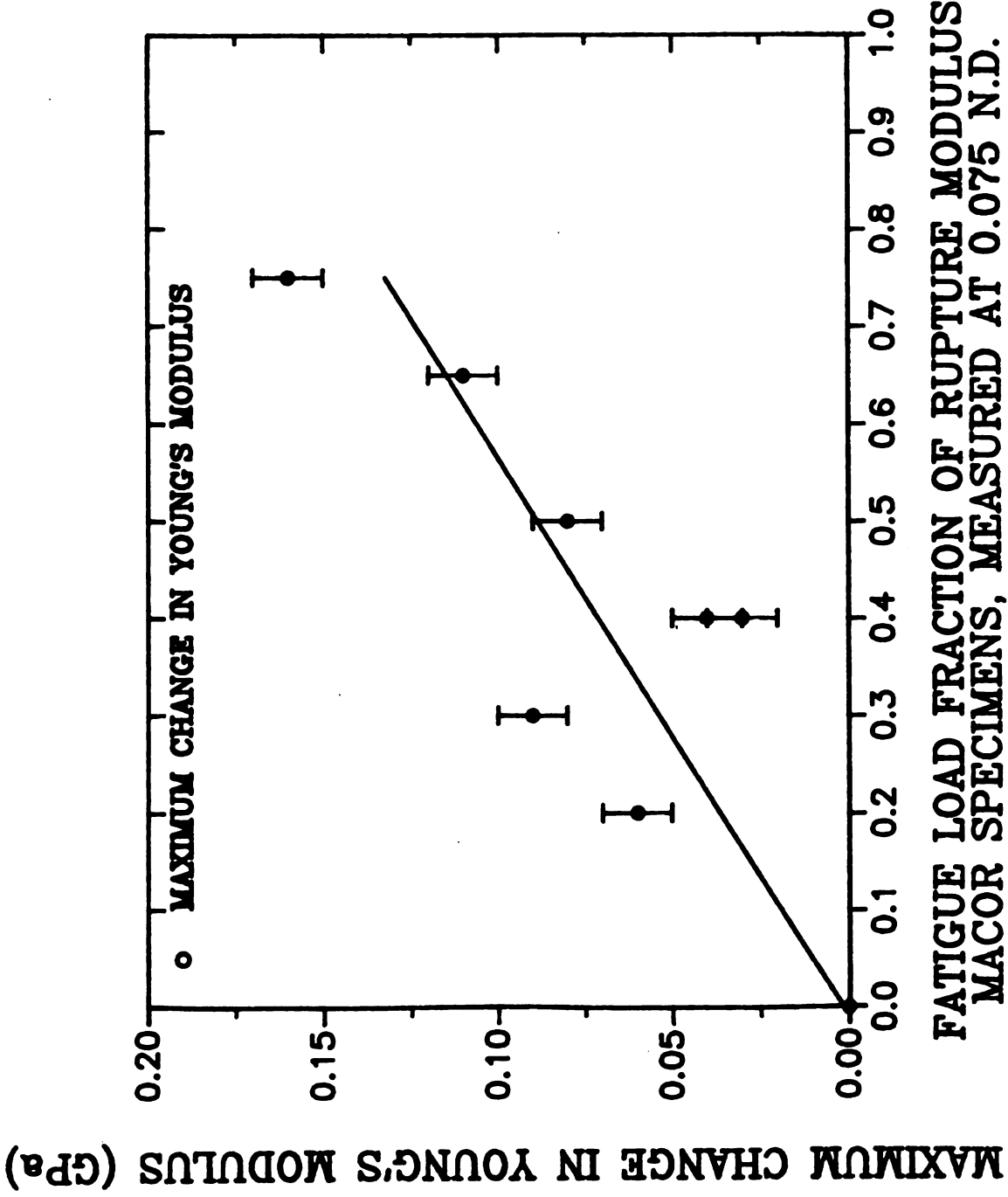
128

Figure 35. Maximum changes in Young's modulus versus fatigue load fraction of rupture strength for Macor specimens, measured at a normalized distance of 0.075 from the free ends of the bar.

error (as standard deviation or coefficient of variation respectively) for all data groups indicates that changes in properties are in general, larger than possible error by an order of magnitude or greater.

4.9   Sensitivity ratio of changes in Young's modulus and internal friction.

The relative changes of Young's modulus and internal friction can be compared using a sensitivity ratio, defined as

$$\text{Sensitivity ratio} = (\Delta Q^{-1} / Q_0^{-1}) / (\Delta E / E_0). \tag{51}$$

Sensitivity ratio computations were based on the maximum overall changes detected in Young's modulus and internal friction (Table 4). It is indicated that the sensitivity ratio is highest for fatigue specimens which experienced the lowest dynamic stresses. For the Macor, at low fatigue stresses, the measurement of internal friction is up to 920 times more sensitve than the measurement of Young's modulus. At the highest fatigue stress, the sensitivity ratio fell to about 100 to 200 times greater normalized change of internal friction than Young's modulus (Figure 36.a). For the GFRP specimens, the sensitivity ratios measured at 0.104 n.d. decreased monotonically (Figure 36.b) from about 330 to 60, but the measurements at 0.32 n.d. appeared erratic and were discounted as not informative.

At low stresses, Young's modulus is affected much less than internal friction. As maximum stresses are increased, the change in Young's modulus grows much faster than the change of internal friction. The change in sensitivity ratios may reflect a difference in the nature of the damage inflicted at the different stress levels.

Table 4. Sensitivity ratios for all fatigue specimens.

Specimen	Pct. M.O.R.	# Cycles *	Sensitivity Ratio **	
			at 0.075 n.d.	at 0.32 n.d.
MA-2	20	500	918.7	919.5
MA-4	30	5000	537.6	701.5
MA-6	40	1000	455.0	916.3
MA-7	40	5000	196.4	412.9
MA-9	50	2500	129.3	265.4
MA-11	65	5000	111.7	391.0
MA-12	75	5000	112.7	263.6
			at 0.104 n.d.	at 0.32 n.d.
GE-5	1.7	1000	328.5	1571.8
GE-1	6.3	10 K	270.3	***
GE-3	9.5	10 K	182.4	240.7
GE-4	14.2	10 K	59.1	793.1

*   Number of cycles after which the maximum change had occured.

**   Using maximum overall changes in Young's modulus and Q^{-1}.

*** No data available for minimum Young's modulus or maximum Q^{-1}.

a)

MACOR SPECIMENS MEASURED AT 0.075 N.D.

b)

GLASS-EPOXY SPECIMENS MEASURED AT 0.104 N.D.
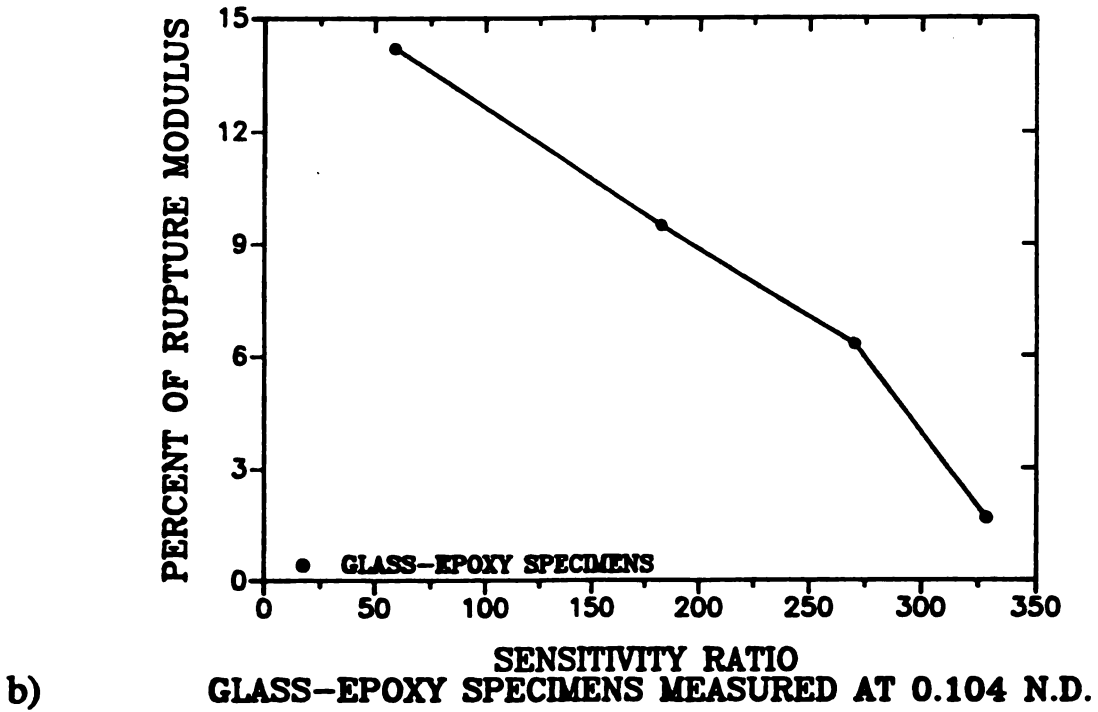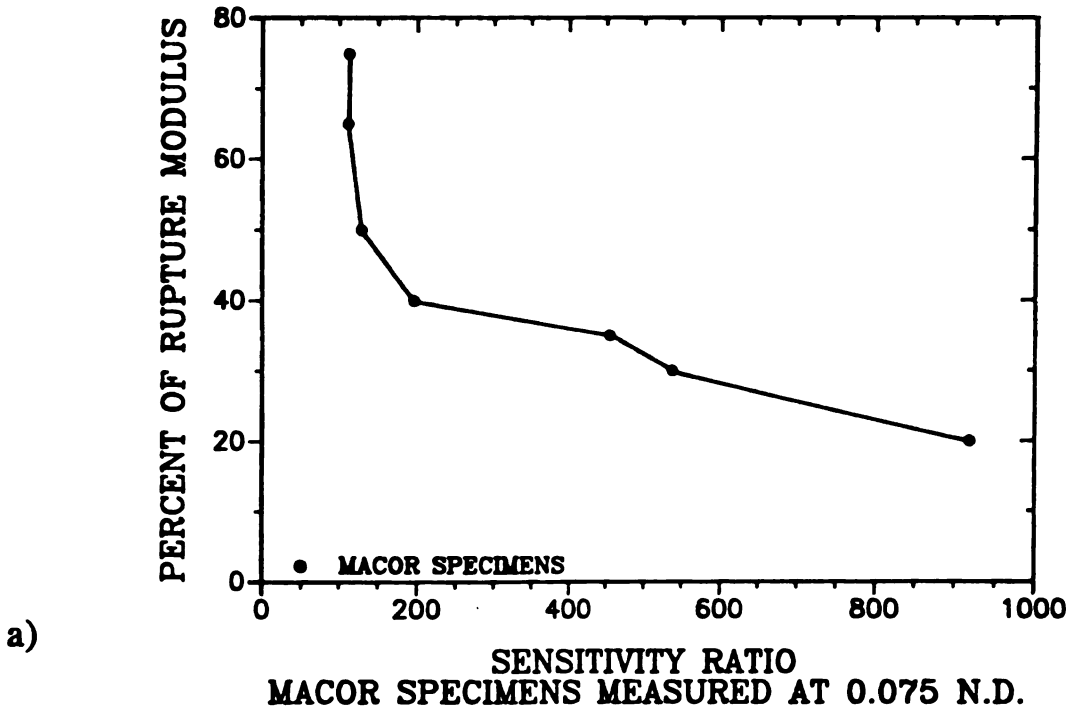
Figure 36. Sensitivity ratio versus maximum fatigue load for Macor and GFRP fatigue specimens. a) Macor specimens, b) GFRP specimens.

4.10. Possible mechanisms to account for variations in values of internal friction and Young's modulus.

4.10.1. Damage recovery mechanism.

The increases and decreases in the physical properties of both materials may result from the closure and partial healing of microcracks. Such recovery occurs in thermally shocked ceramics and mechanically loaded glasses (both inorganic and organic) [87 - 90].

Kim et al. [87] studied the effect of one thermal shock in deionized water at room temperature. Kim carefully monitored Young's modulus in room temperature laboratory air as time progressed. A time constant for recovery from thermal shock, analogous to that in capacitive and inductive electrical circuits, was established for several ceramic materials. The time constant is 30 to 100 minutes for Macor, depending on quench temperature [87]. For polycrystalline alumina , the time constant for recovery is about twenty five minutes, and for NLS glass is about 4300 minutes [87].

Stravrinidis et al. [88] showed significant compositional changes beneath the fresh surface of an NLS glass within minutes after exposure to moist laboratory air, using auger spectroscopy and progressive ion milling.

For the organic glasses, the strain energy release rate for repropagation of a crack was independent of time, from 5 minutes to 4 months [88]. This implies that all recovery occurs within the first five minutes after cracking. The energy release rate for repropagation of a crack in Araldite CT 200 epoxy, with or without HT901 phthallic anhydride hardener (both Ciba - Geigy products), was greater than for the propagation of the original crack [88].

The times involved in the fatigue tests of this study are about 1.5 seconds per load cycle, with the first major peak in the value of either physical property occuring between 100 and 350 load cycles. The peak occurs over a

132

time span of about two to eight minutes. This time span is approximately within the time determined by Stravrinidis et al. for full recovery in the Araldite epoxy glass [88].

Although one fatigue cycle (as performed for this study) takes much less time than the established time constants for Macor or the Araldite epoxy, there is a significant difference here. The difference lies in the cyclic loading of the specimen. Due to the fatigue loading, the repeated abrasion of internal microcrack surfaces is likely to be occuring. Repeated abrasion is likely to repeatedly expose a fresh, nascent surface ready to react with any atmospheric species that can work its way to the crack. The transport mechanisms of diffusion, convection and/or pressure differential may be involved in getting the reactant species to the crack surfaces.

The increase in modulus and decrease in internal friction may be explained by recovery, but the reversal of the recovery must also be addressed. The material may only recover to a certain extent, and only so many times throughout its fatigue life. For some number of load cycles, the accumulation of a restoring 'chemical glue' may be overcome by repeated damage (due to repeated load cycling) and the values of Young's modulus or internal friction may be returned to their damaged values. Further, it may be possible that, as the material periodically recovers and damages, the internal microcrack faces accumulate debris. The accumulation of debris may provide two means by which recovery is reduced: (1) to restrict or prevent further abrasion of the nascent surface and possible reaction with atmospheric species and (2) to prevent the closure of the microcrack. The accumulation of debris on the crack faces may explain the decreasing variations in Young's modulus and internal friction after the initial large change.

The apparent periodicity of the change in properties for both materials was plotted with very inconclusive results. This indicates that there is a need for more data points. To have more data points, an in situ means of

measuring both Young's modulus and internal friction are required.

4.10.2.   Damage progression mechanism.

The progression of damage in the GFRP specimen was inhomogeneous in nature, as evidenced by the growth of a midplane shear crack throughout the specimen. Microcrack damage in Macor may progress similarly. The load pin contacts on the specimen may play a role in the advancement of damage across the specimen. If the damage was arrested at the point where a load pin contacts the specimen (where normal and shear stress states change significantly), then recovery may be enhanced.

Since the variation of physical properties was similar between both materials used for this study (with respect to the inhomogeneous progression of the midplane crack in the GFRP composite), it can be argued that the progression of microcracking in Macor followed a similar schedule.

If more reliable crack length data were available for the both types of specimens, a correlation between damage and internal friction or Young's modulus may be shown to exist. Reliable means of damage characterization for the GFRP composite specimens, such as ultrasonic C-scan or transmission X-ray, may provide an accurate monitor of damage development. Microcracking in ceramics such as Macor is not yet quantifiable.

4.10.3.   Test for long term recovery of Young's modulus.

After fatigue testing, all unbroken specimens were saved for future measurements of Young's modulus and internal friction. The intitial values were compared to the values after the final fatigue cycle and values determined between 30 and 150 days later (Table 5). The latter values were determined

Table 5.   Long term values of Young's modulus. *

Specimen	# Cycles **	Young's Modulus (GPa)		
		Initial ◊	Final Fatigue ◊◊	Long Term (Days)
GE-1	10 K	41.5394	41.6007	41.5925 (151)
GE-3	10 K	41.8252	41.7792	41.7419 (120)
GE-4	1000	43.7759	42.6243	43.6966 (112)
GE-5	1000	41.24	41.22	41.2828 (27)
GE-2	***	43.820	N/A	43.797 (145)
MA-6	***	62.110	N/A	62.1030 (64)
MA-3	1000	62.256	62.251	62.265 (94)
MA-4	5000	61.957	61.970	61.9971 (92)
MA-7	5000	62.200	62.189	62.1295 (88)
MA-11	5000	63.913	63.878	63.8887 (72)
MA-12	5000	62.507	62.449	62.4925 (66)

*   =   GFRP specimens measured at 0.12 n.d. and Macor specimens
          measured at 0.075 n.d.

**   =   Number of cycles taken for min/max to occur.

◊   =   Prior to any fatigue damage.

◊◊   =   Immediately after the last fatigue load cycle.

*** =   Working standards.

N/A =   Not Applicable.

for all specimens on the same day, accounting for the different times since the final fatigue load. In the time scale of days, any real time constant for recovery must be long exceeded. Considering full recovery to require five time constants, the specimens were considered recovered to their full capability.

All Macor specimens (except MA-7, fatigued at 40 percent M.O.R.) exhibited recovery since their final fatigue load cycle. The specimens that experienced stresses up to 20 percent of M.O.R. recovered to approximately their initial values. Those specimens that saw the stresses of 30 percent of M.O.R. and higher did not recover beyond their initial values.

4.11. Internal friction and Young's modulus versus acoustic emission.

To the author's knowledge, no researcher has correlated the damage measures of acoustic emission and changes in internal friction and Young's modulus. This may be due to no one having looked into the matter, or because no one has shown a strong relation and reported it in the open literature.

4.11.1. Possible trends between AE and internal friction.

Acoustic emission counts were sorted into ten equal sections of maximum load, then plotted against internal friction (Figures 37, 38 and 39). Each plot shows how AE counts accumulated during that range of load, with respect to the change of internal friction. Again, the most prominent feature of plotting AE with internal friction is the peak which developed early in the fatigue life of all three GFRP specimens.

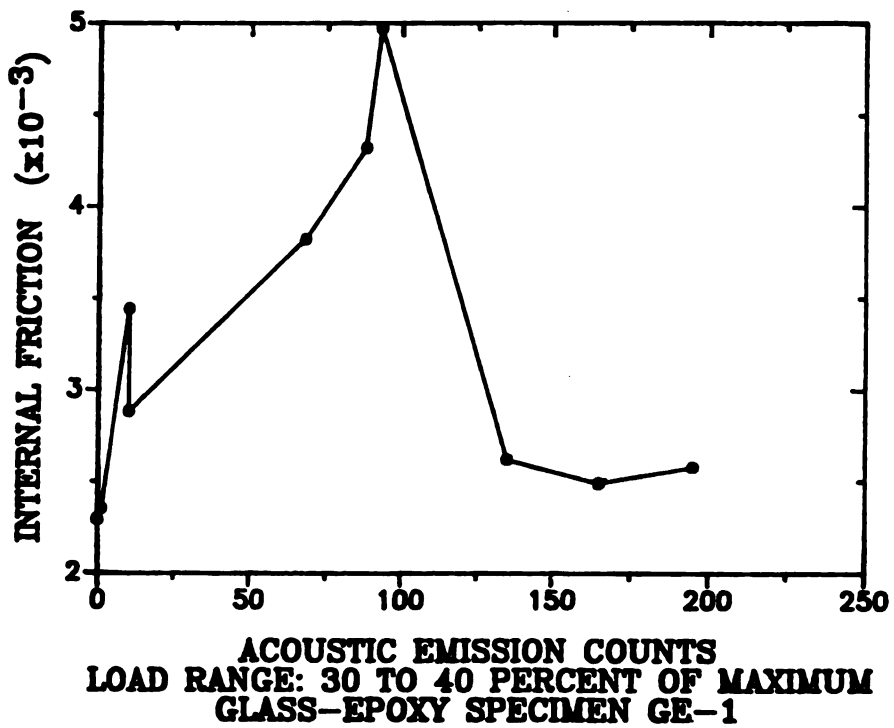Short sections of some of the plots of internal friction versus acoustic

a)
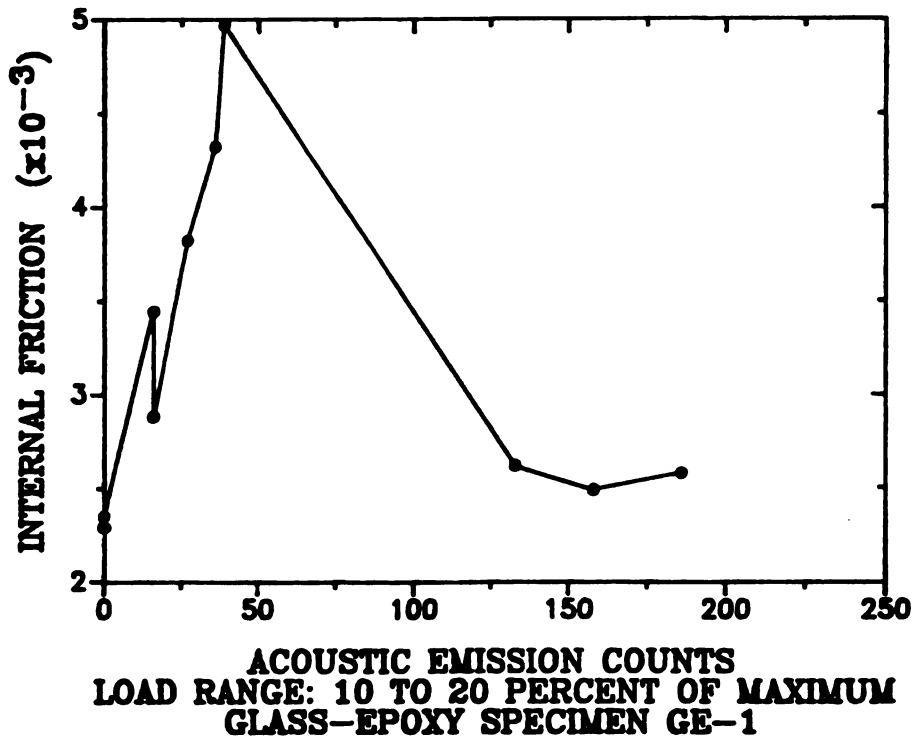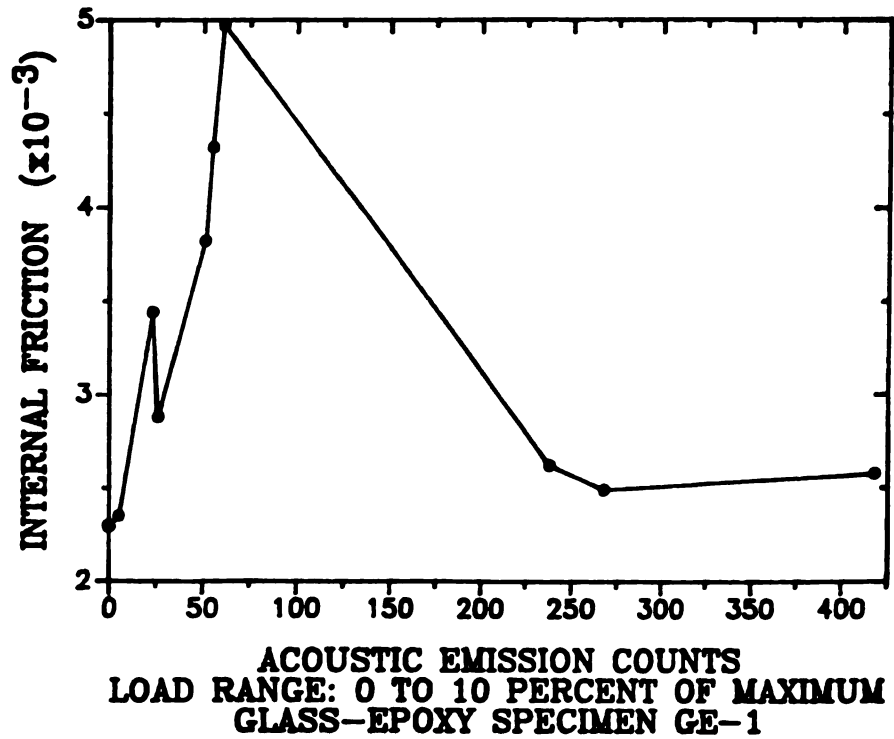
b)

Figure 37 a,b. Internal friction versus acoustic emission counts accumulated over 500 fatigue cycles, GFRP specimen GE-1. a) load range from zero to 10 percent of maximum load, b) 10 to 20 percent.
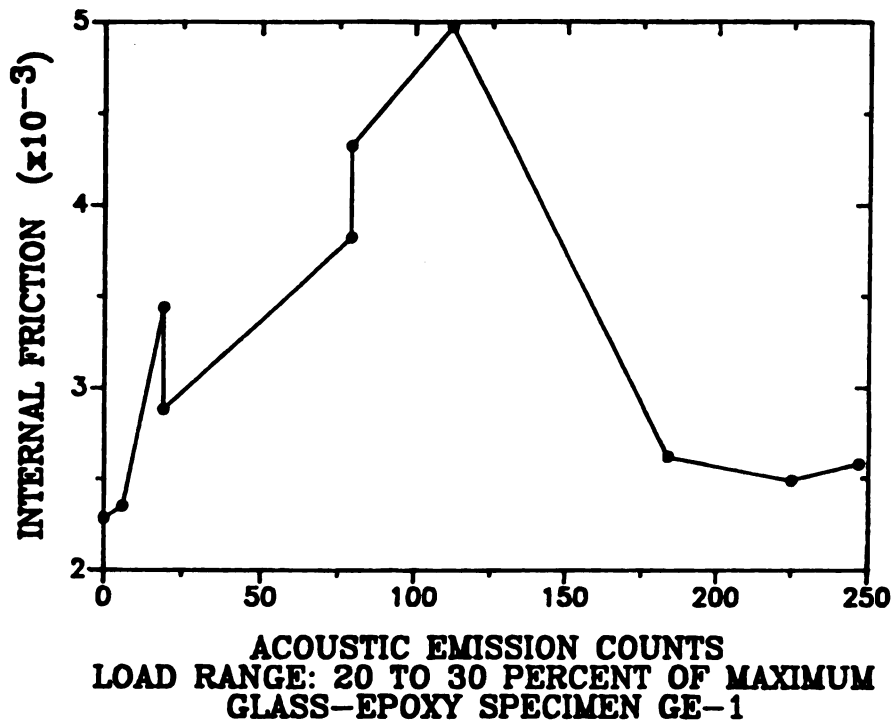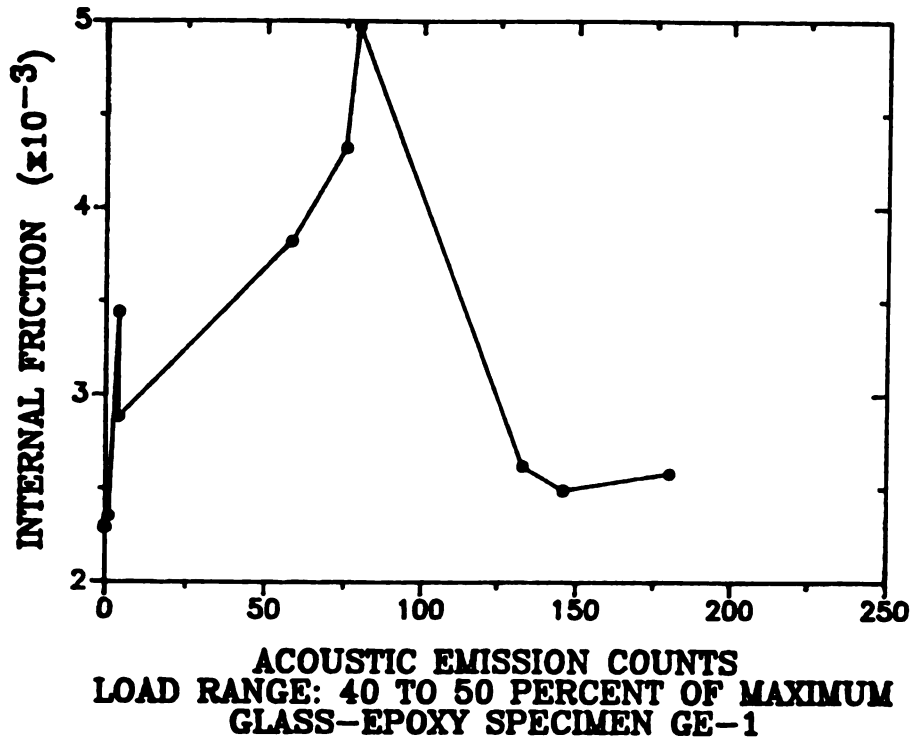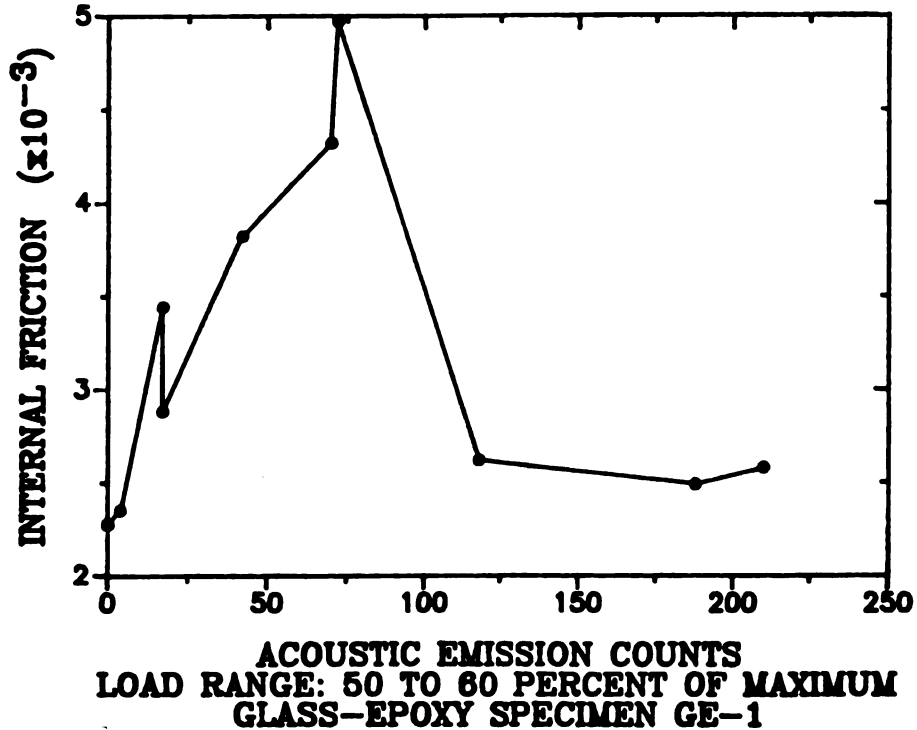
c)

d)

Figure 37 c,d.   Internal friction versus acoustic emission counts accumulated over 500 fatigue cycles, GFRP specimen GE-1.   c) load range from 20 to 30 percent of maximum load, d) 30 to 40 percent.
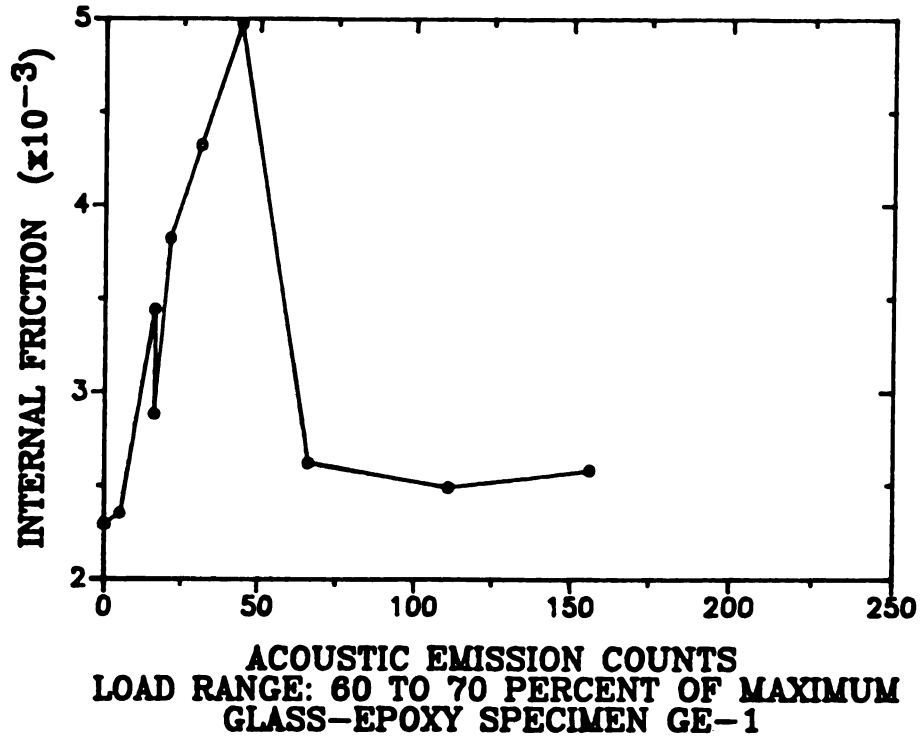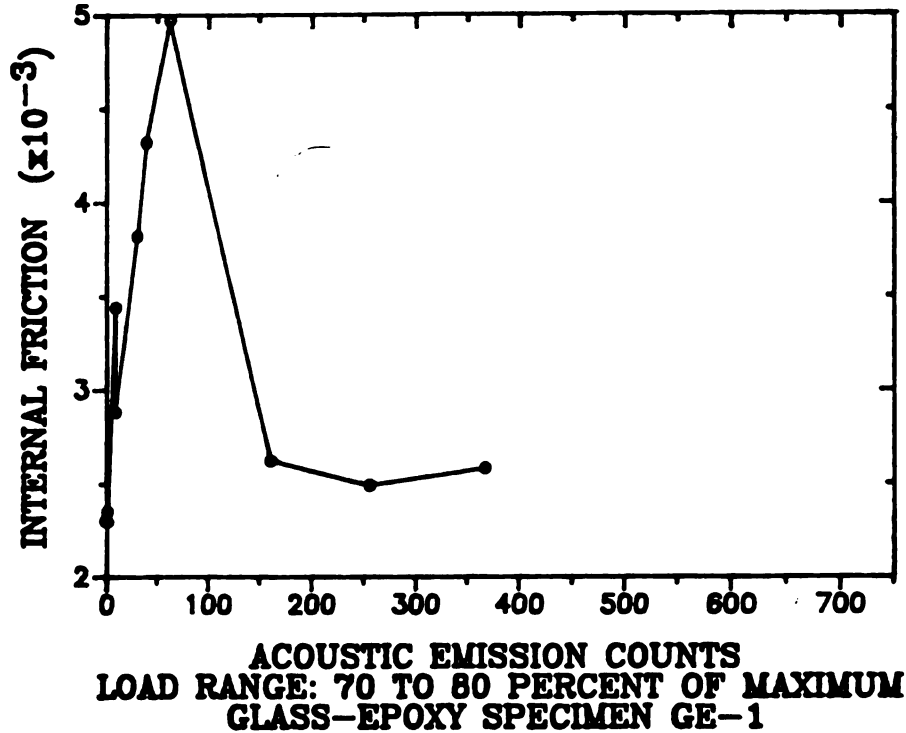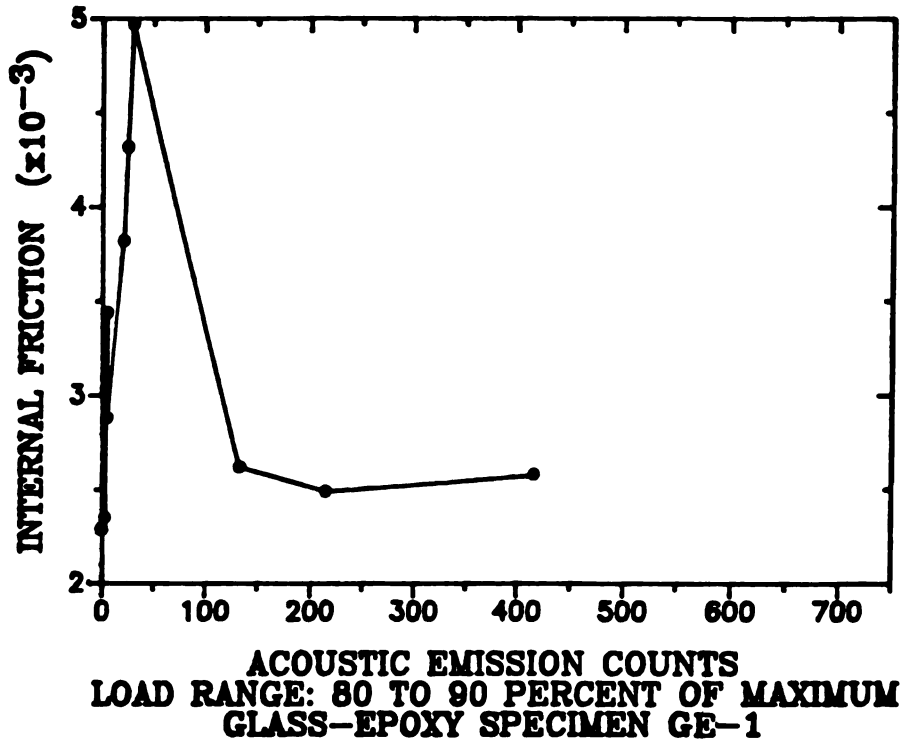
e)

f)

Figure 37 e,f.   Internal friction versus acoustic emission counts accumulated over 500 fatigue cycles, GFRP specimen GE-1.   e) load range from 40 to 50 percent of maximum load, f) 50 to 60 percent.
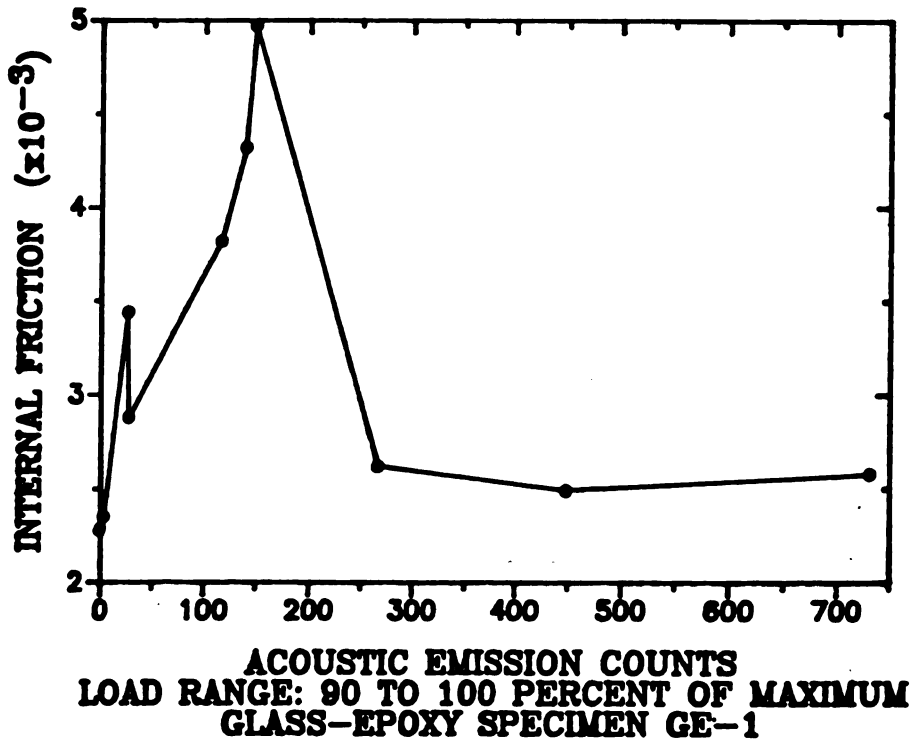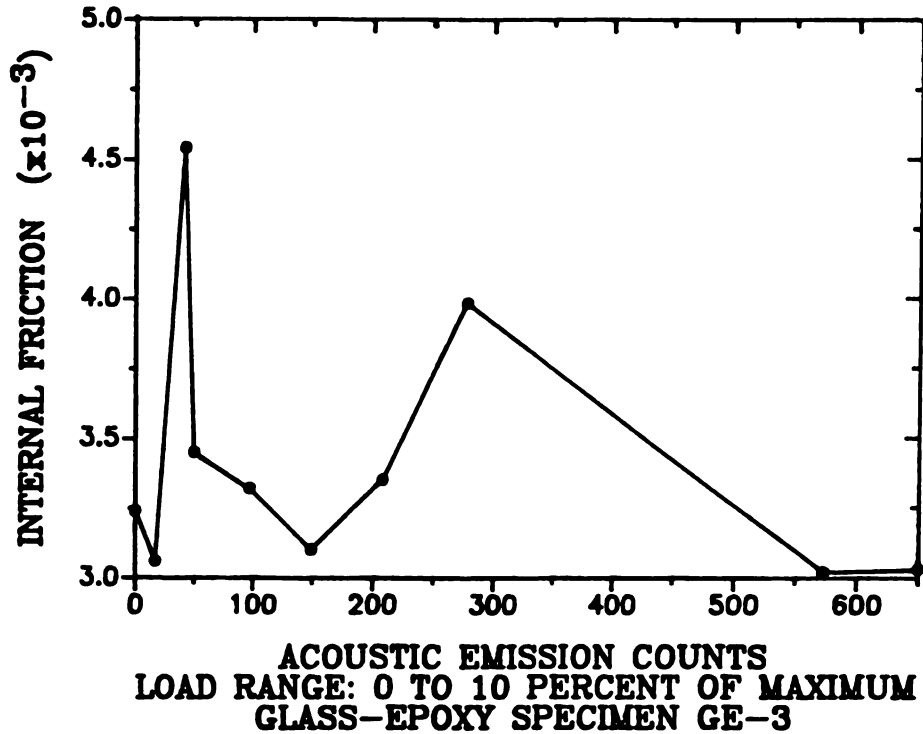
g)

h)

Figure 37 g,h.   Internal friction versus acoustic emission counts accumulated over 500 fatigue cycles, GFRP specimen GE-1.   g) load range from 60 to 70 percent of maximum load, h) 70 to 80 percent.
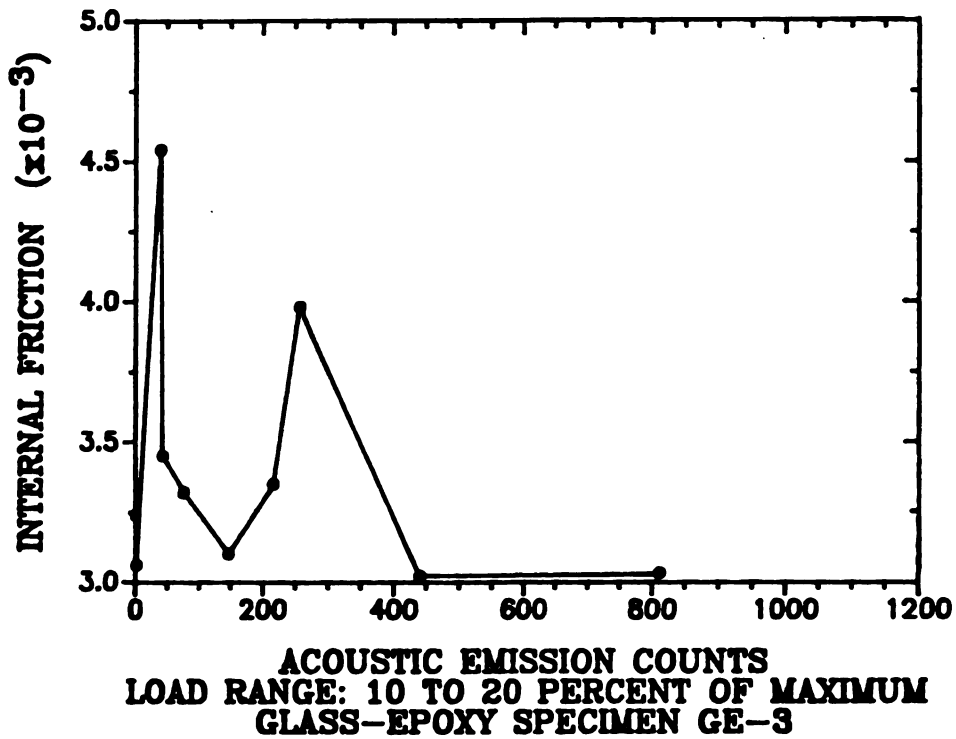
i)

j)

Figure 37 i,j.   Internal friction versus acoustic emission counts accumulated over 500 fatigue cycles, GFRP specimen GE-1.   i) load range from 80 to 90 percent of maximum load, j) 90 to 100 percent.
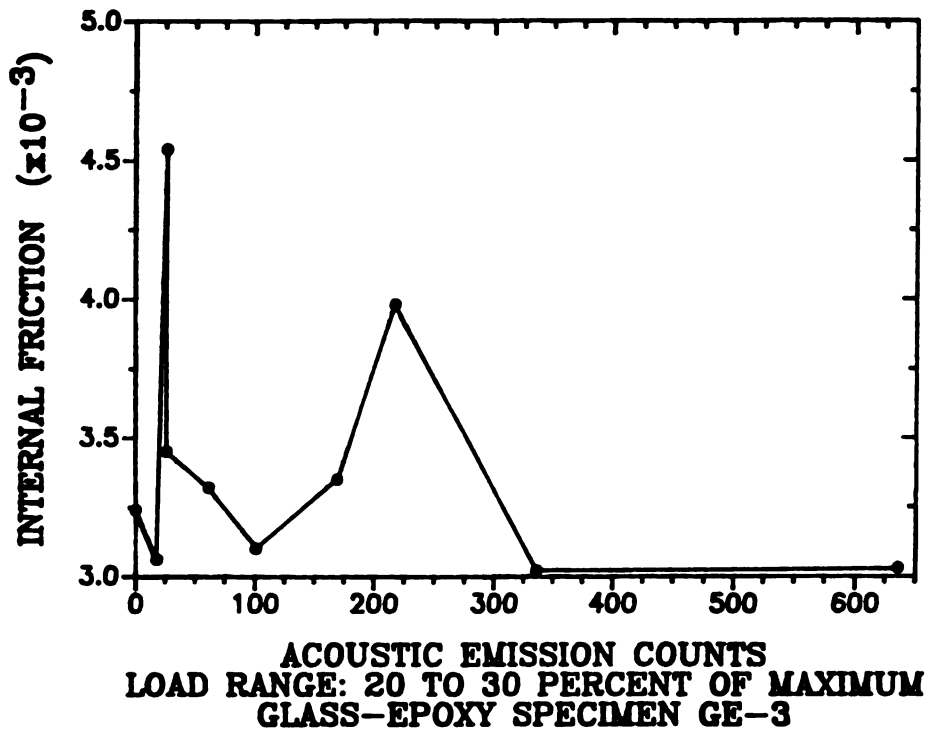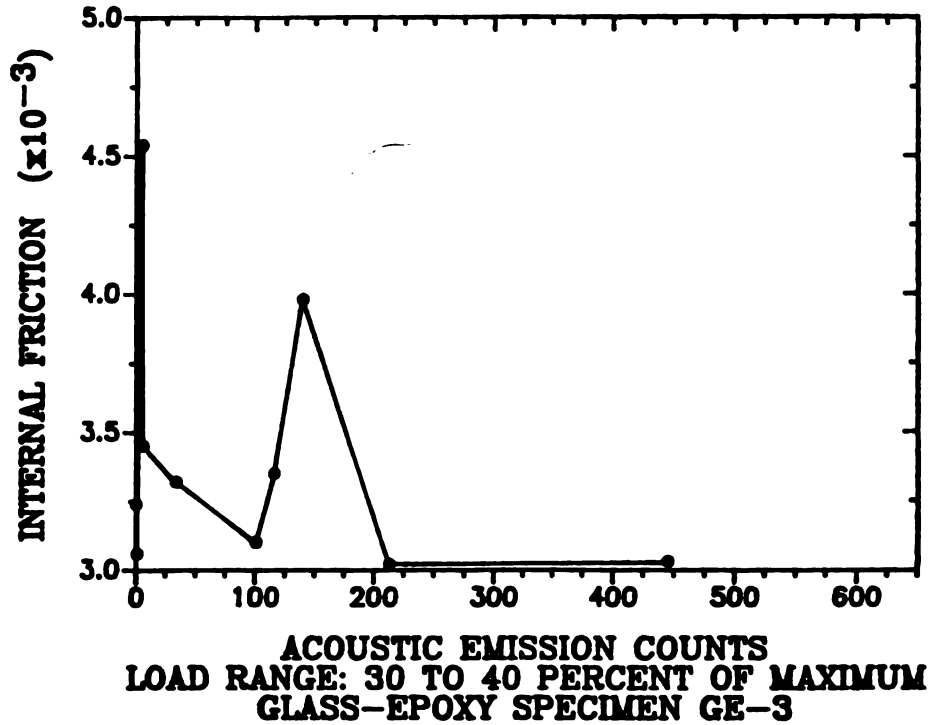
Figure 38 a,b. Internal friction versus acoustic emission counts accumulated over 1000 fatigue cycles, GFRP specimen GE-3. a) load range from zero to 10 percent of maximum load, b) 10 to 20 percent.
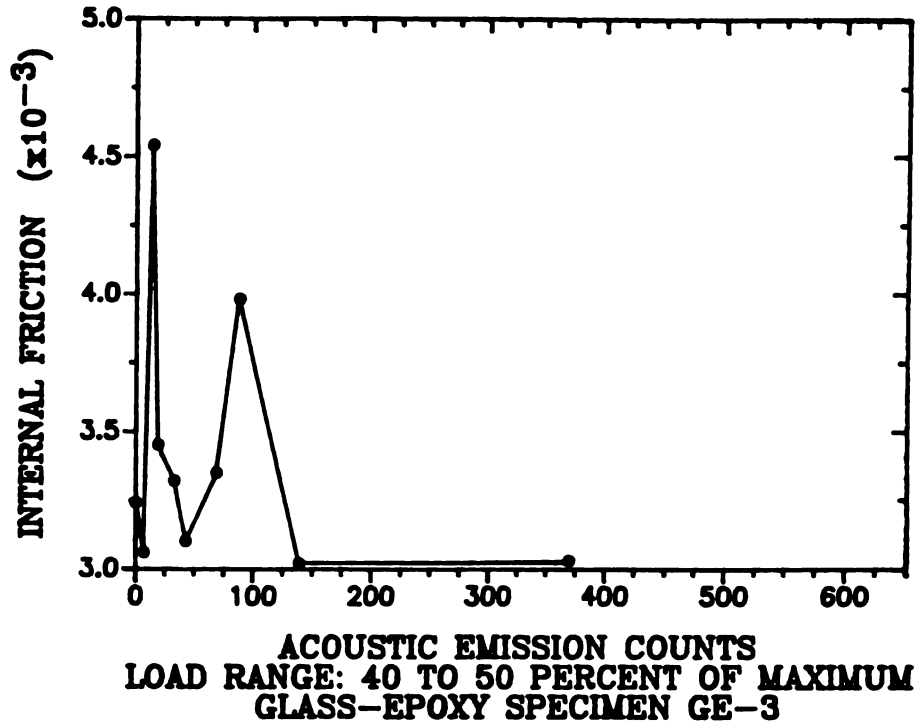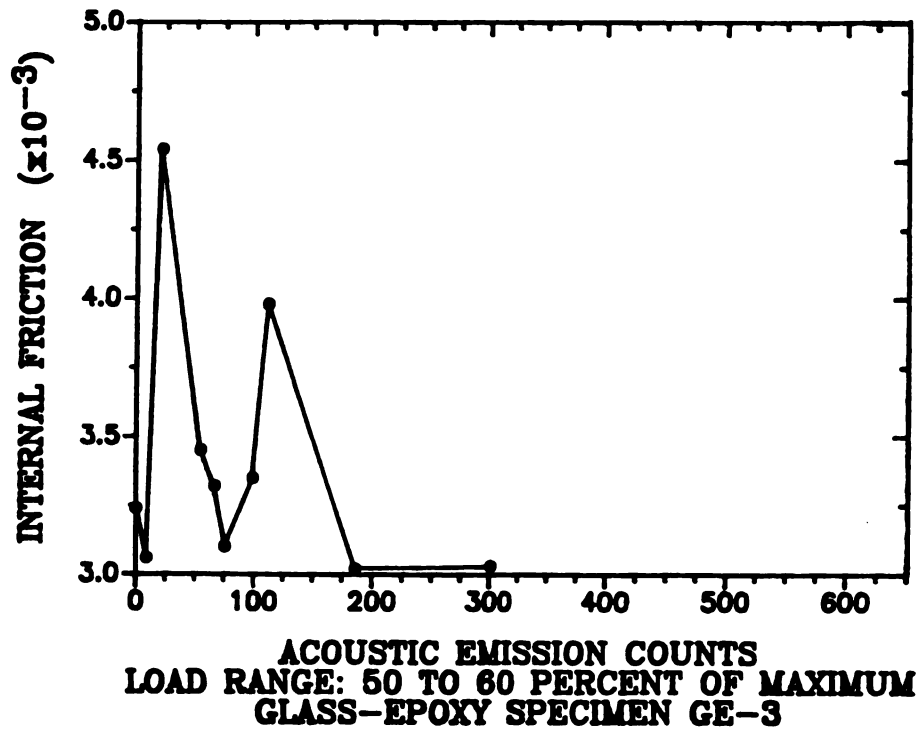
c)

d)

Figure 38 c,d.   Internal friction versus acoustic emission counts accumulated over 1000 fatigue cycles, GFRP specimen GE-3.   c) load range from 20 to 30 percent of maximum load, d) 30 to 40 percent.

e)

f)

Figure 38 e,f.   Internal friction versus acoustic emission counts accumulated over 1000 fatigue cycles, GFRP specimen GE-3.   e) load range from 40 to 50 percent of maximum load, f) 50 to 60 percent.

g)

h)

Figure 38 g,h. Internal friction versus acoustic emission counts accumulated over 1000 fatigue cycles, GFRP specimen GE-3.   g) load range from 60 to 70 percent of maximum load, h) 70 to 80 percent.
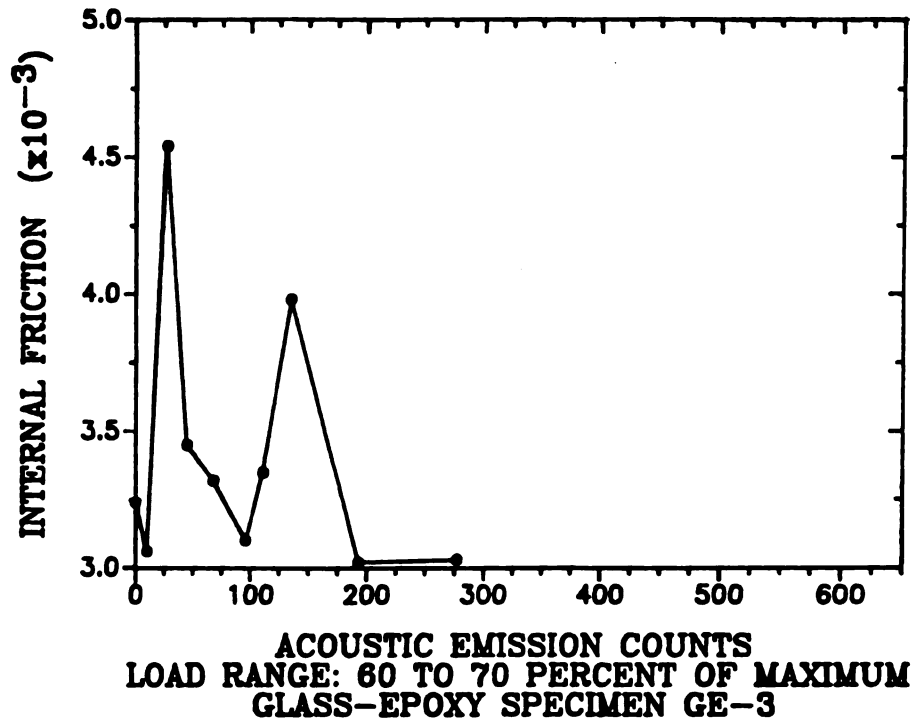
i)

j)

Figure 38 i,j. Internal friction versus acoustic emission counts accumulated over 1000 fatigue cycles, GFRP specimen GE-3. i) load range from 80 to 90 percent of maximum load, j) 90 to 100 percent.

a)

b)

Figure 39 a,b. Internal friction versus acoustic emission counts accumulated over 1000 fatigue cycles, GFRP specimen GE-4. a) load range from zero to 10 percent of maximum load, b) 10 to 20 percent.
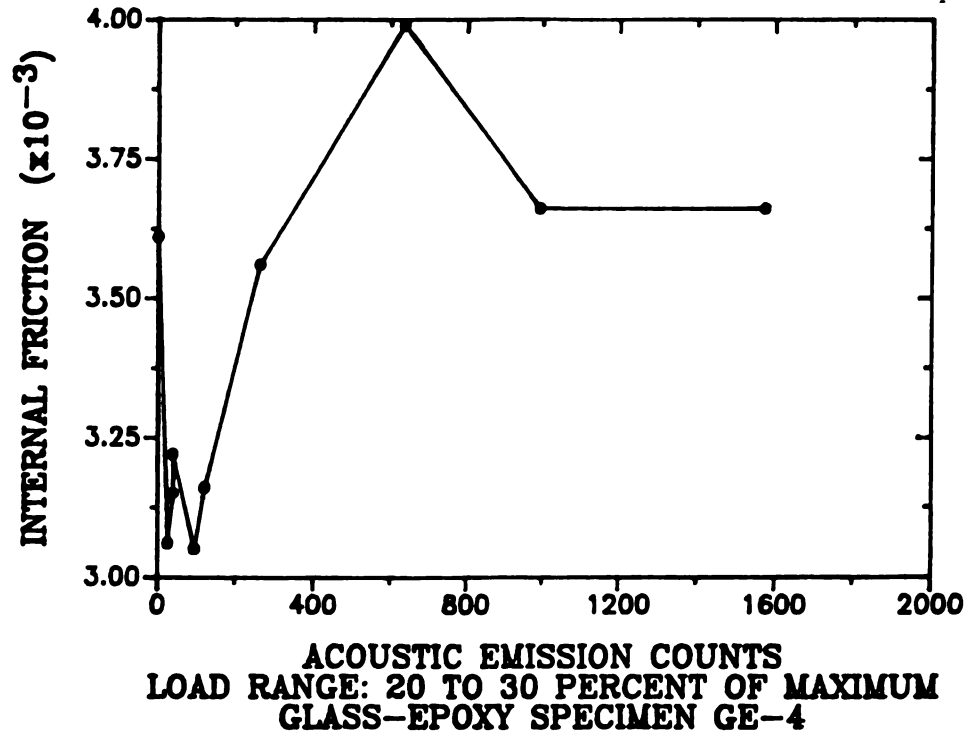
c)
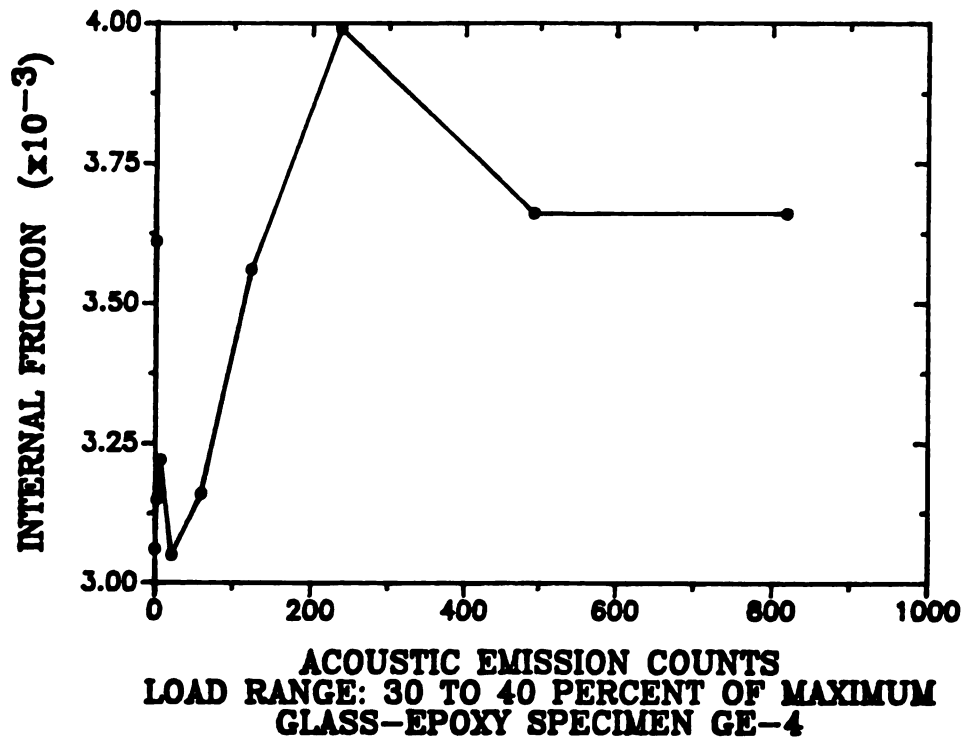
d)

Figure 39 c,d. Internal friction versus acoustic emission counts accumulated over 1000 fatigue cycles, GFRP specimen GE-4. c) load range from 20 to 30 percent of maximum load, d) 30 to 40 percent.
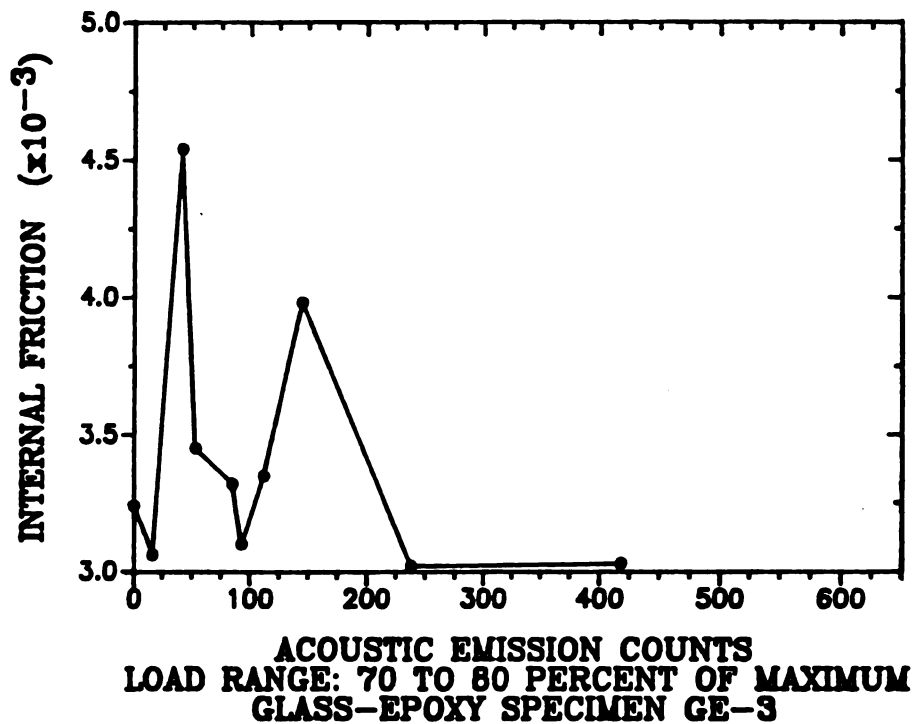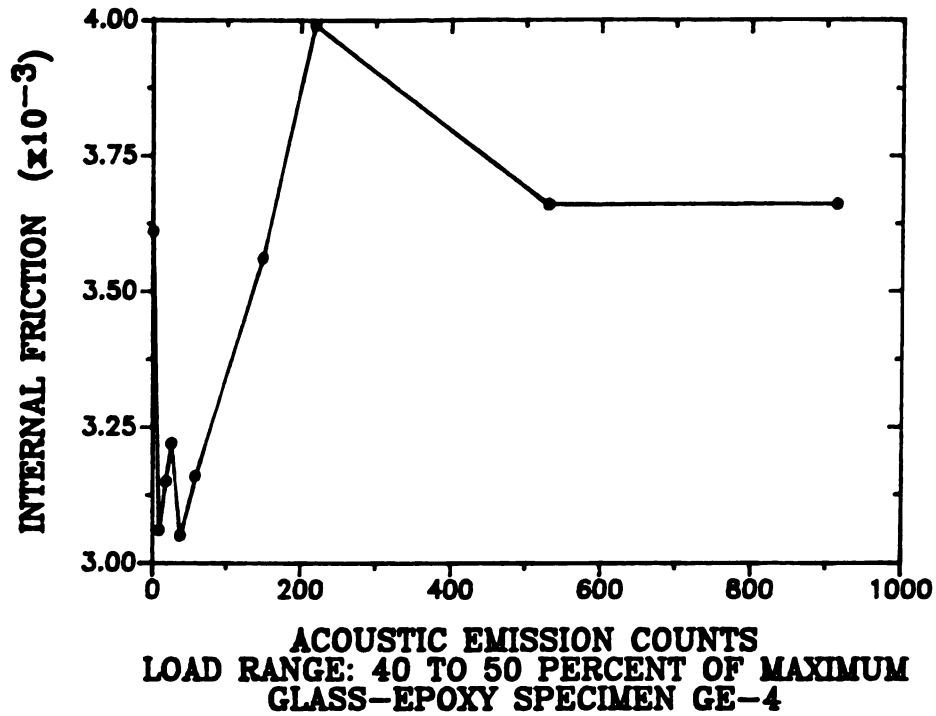
e)
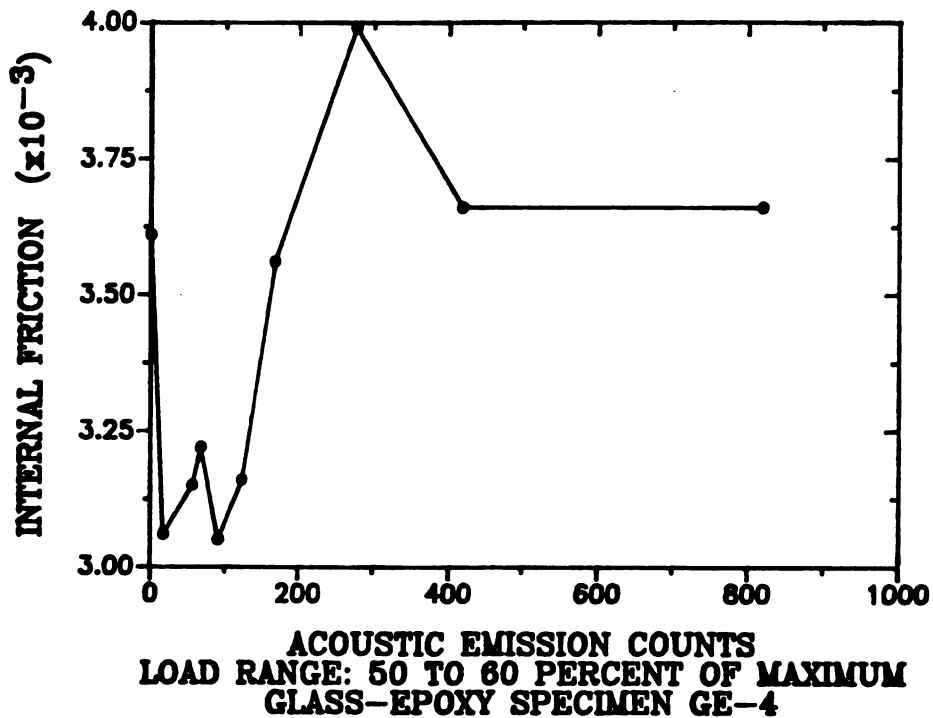
f)

Figure 39 e,f. Internal friction versus acoustic emission counts accumulated over 1000 fatigue cycles, GFRP specimen GE-4. e) load range from 40 to 50 percent of maximum load, f) 50 to 60 percent.
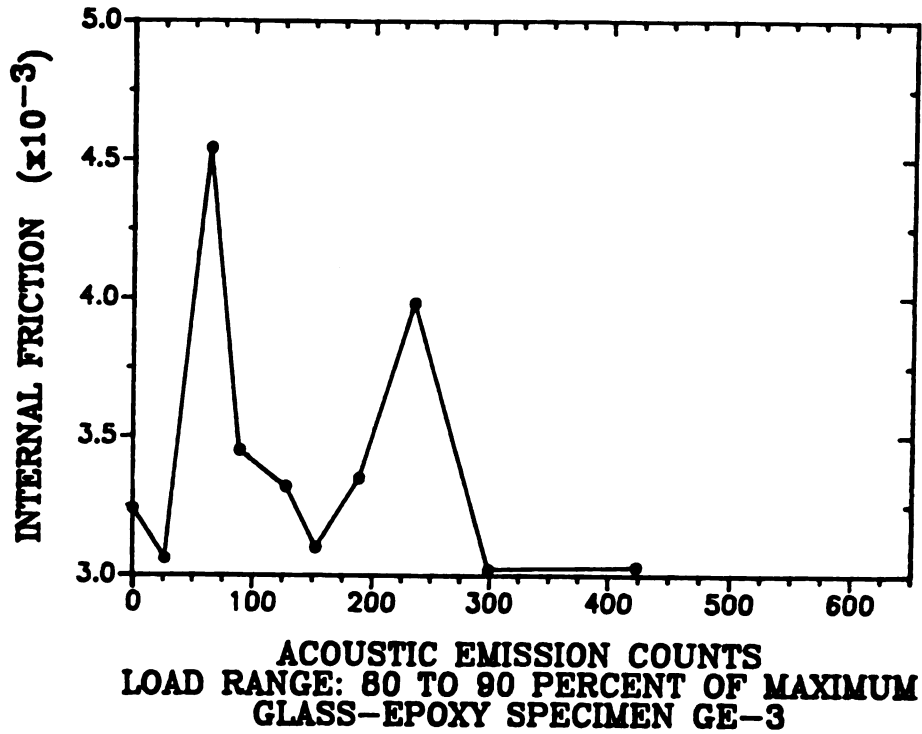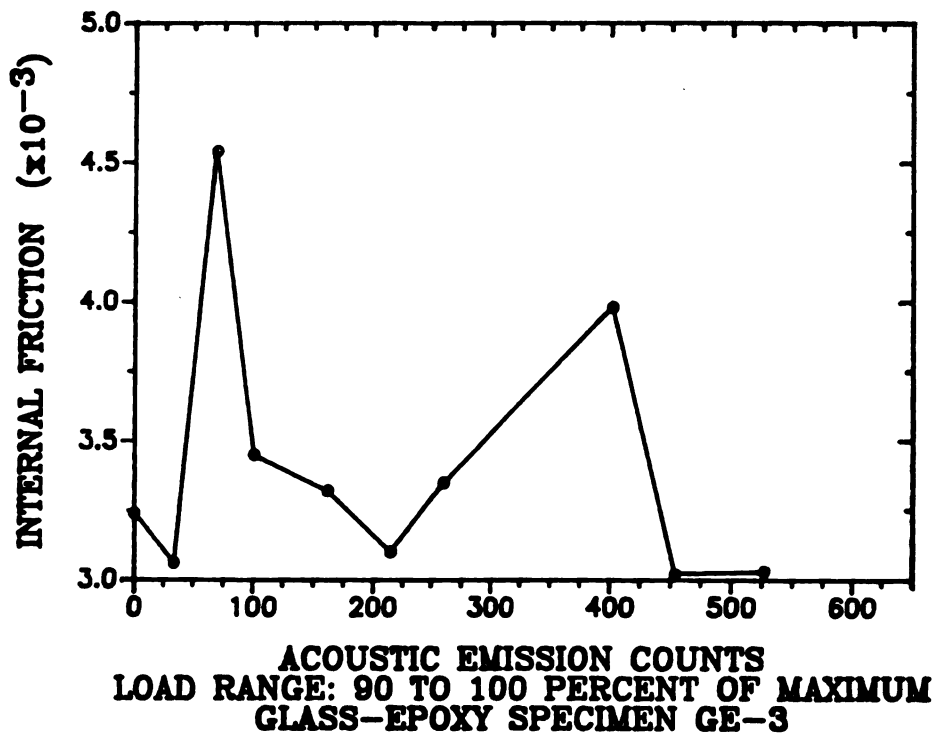
g)

h)

Figure 39 g,h. Internal friction versus acoustic emission counts accumulated over 1000 fatigue cycles, GFRP specimen GE-4. g) load range from 60 to 70 percent of maximum load, h) 70 to 80 percent.
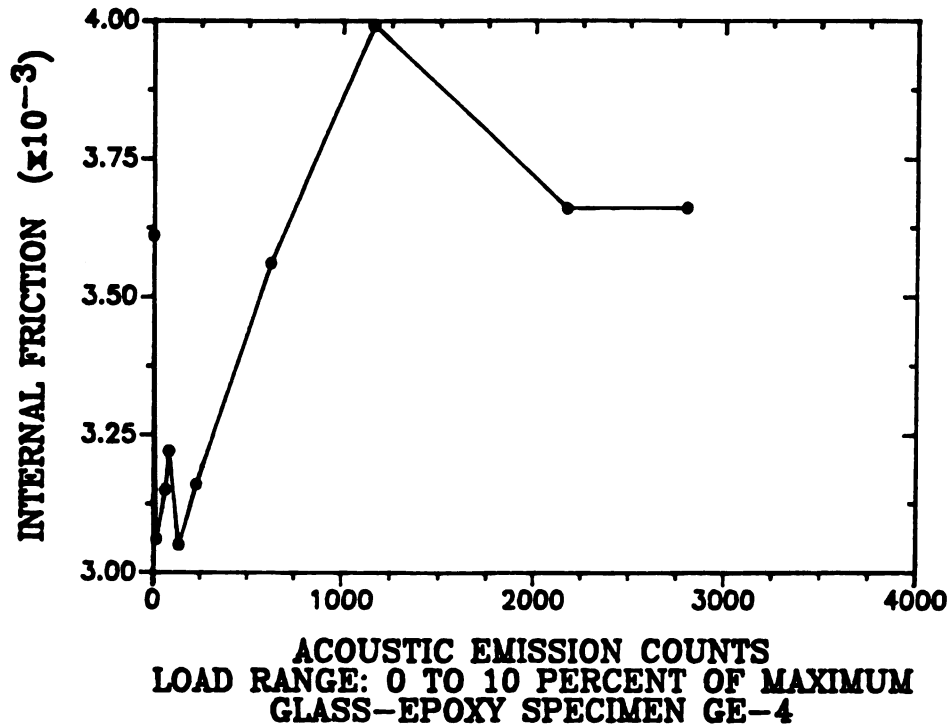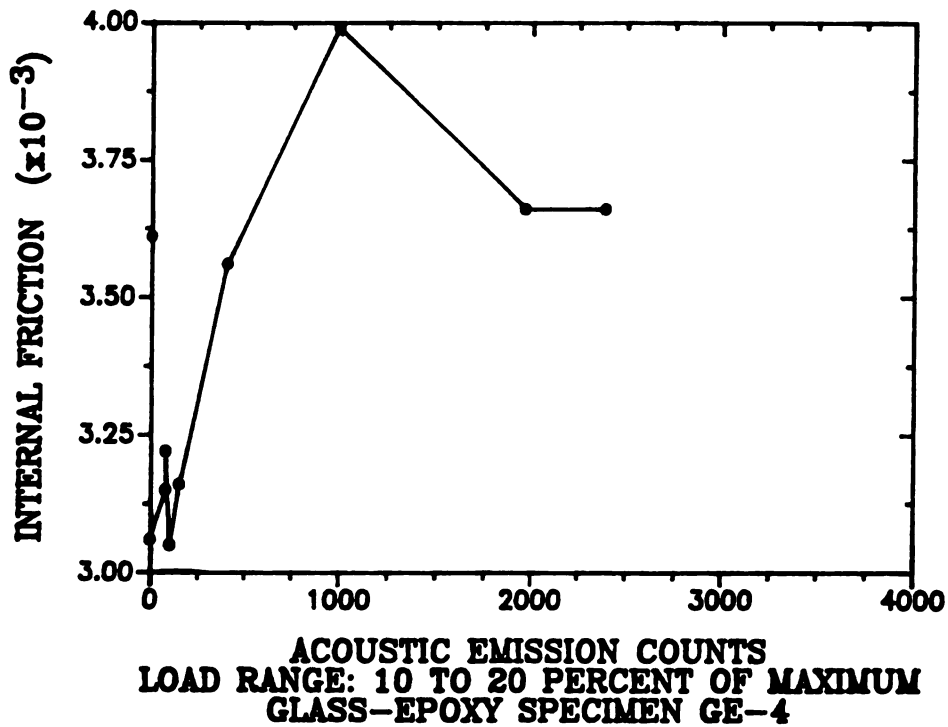
i)

j)

Figure 39 i,j. Internal friction versus acoustic emission counts accumulated over 1000 fatigue cycles, GFRP specimen GE-4. i) load range from 80 to 90 percent of maximum load, j) 90 to 100 percent.
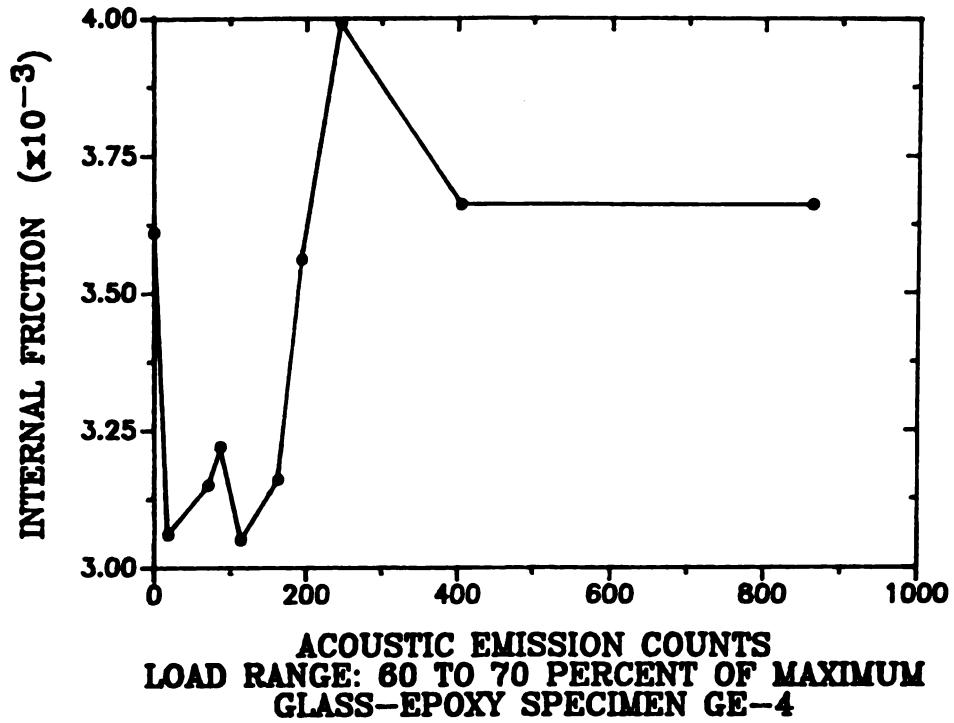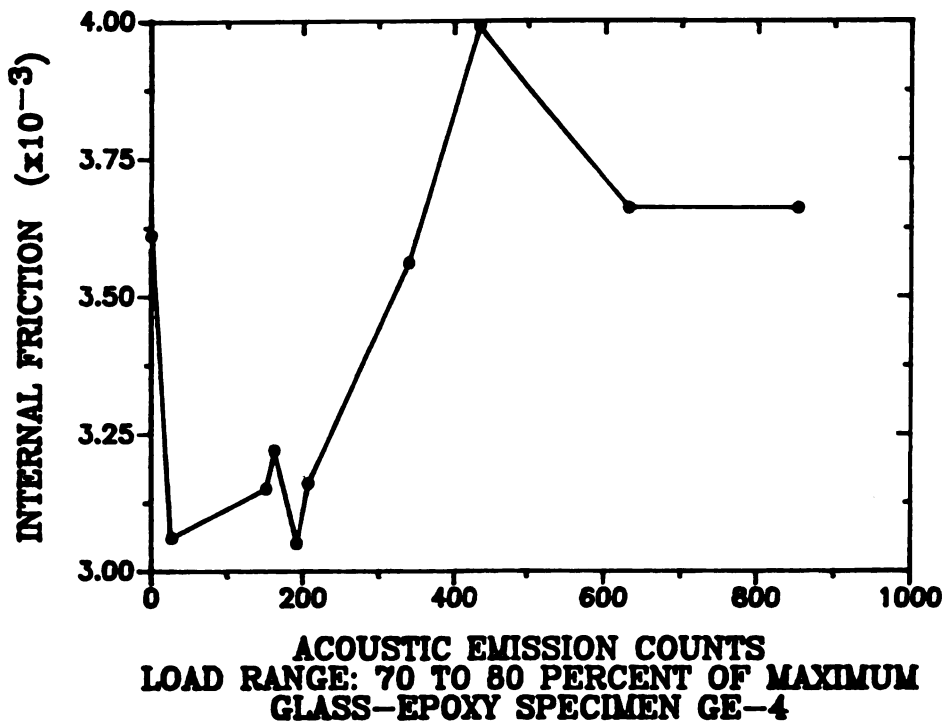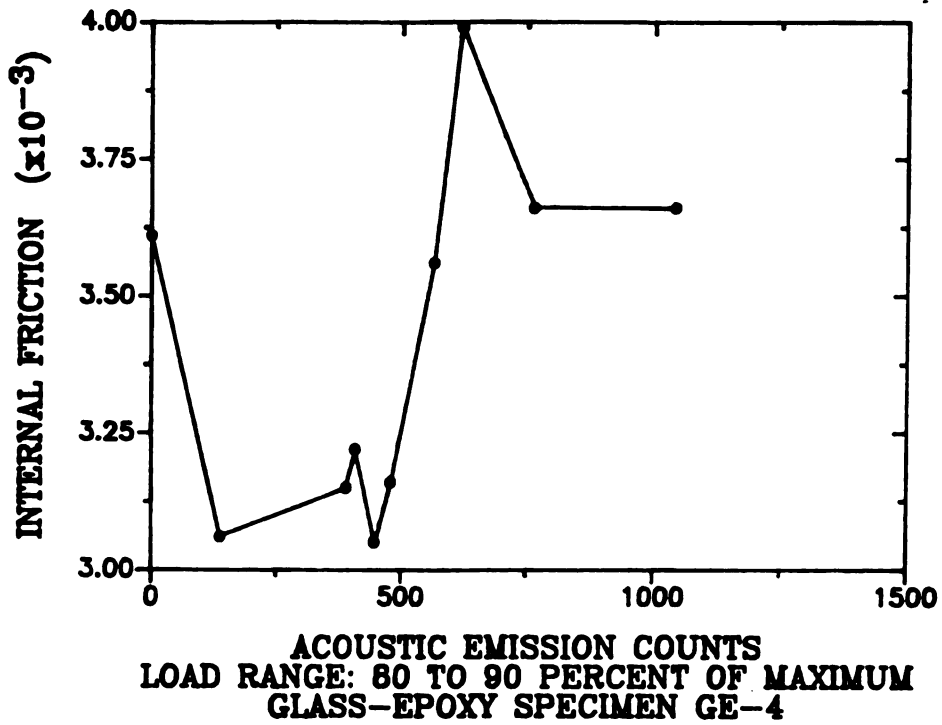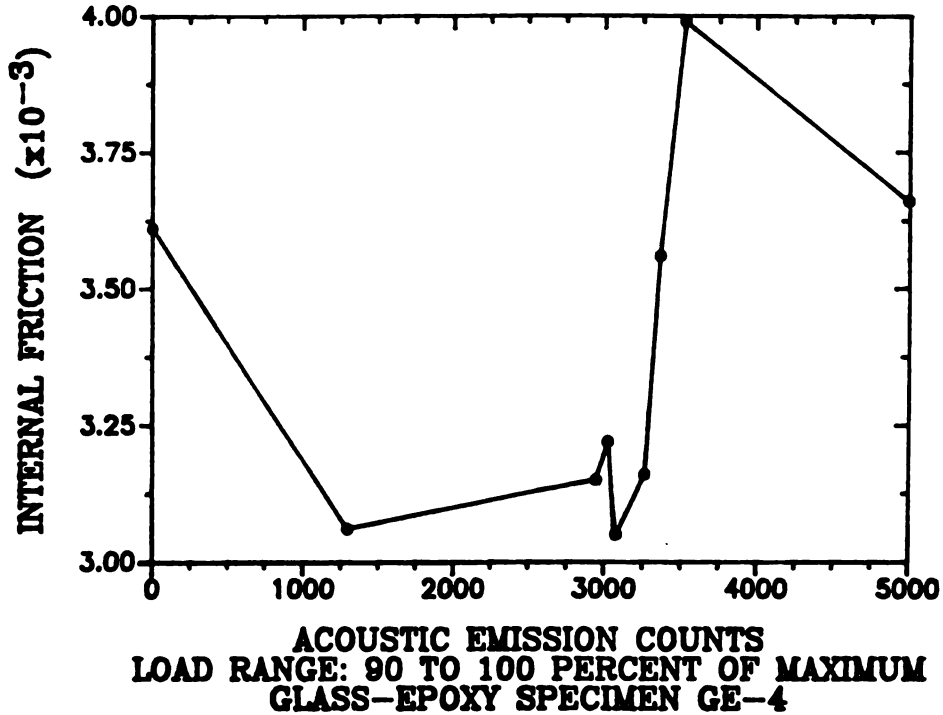
emission counts showed a piecewise linearity, but in general, appeared similar to the plots of internal friction versus fatigue load cycles, with local maxima and minima due to the variation of internal friction.

The significance of a linear increase of AE with internal friction is not clear at this point, but clearly, in Figures 37, 38 and 39, the lower the relative slope between examination points (since the internal friction coordinates were fixed for the set of plots for each specimen), the more AE was produced, from one load range to another. The observation that AE varied among load ranges was examined in Section 4.5. This section attempts to tie AE counts into changes in internal friction; one of the initial goals of the study.

It is observed that in some load ranges (Figures 37 through 39), AE counts accumulate at a rate which correlates linearly with the development of internal friction. Only where there are at least three data points involved, can this aspect of analysis be applied. The apparent linearity does not necessarily imply that the load range in question has anything to do with crack growth. On the contrary, those load ranges which have the most acoustic emission during the larger changes in internal friction or Young's modulus are likely responsible for damage growth (Section 4.5).

Some load ranges produced more AE on the leading side of the major peak, whereas other load ranges produced more AE on the trailing side of the major peak. This observation suggests that damage during recovery and during degredation may occur in different ranges of the load cycle. This in turn, suggests an evolution of the damage as recovery and degredation occur.

As example, Figures 37.c, d and e, in load ranges 20 to 30, 30 to 40 and 40 to 50 percent of maximum respectively, show the lagest amount of AE on the leading side of the major peak. Figure 37.a, b and c, in load ranges 0 to 10, 10 to 20 and 20 to 30 percent of maximum show the most AE on the trailing side of the major peak. The remainder of Figures 38 and 39 are left to the reader to examine and make similar comparisons.

There is some support for this observation. During the fatigue cycles in which the largest change of internal friction was observed, the load range responsible for the damage likely produces the most AE. This is with respect to the confirmation that the AE detected at the ends of the load range was contaminated by a substantial amount of machine or system noise (Section 4.3).

For all GFRP specimens, the occurance of the most AE during the part of the load range in which the physical property changes is likely in the load range in which the most damage occurs. The occurance of AE in a part of the load range in which the physical property does not change may represent the friction during which recovery occurs.

5. Conclusions.

5.1. AE in load ranges.

The end ranges of the load cycle produce most of the acoustic emission. Machine noise tests revealed that substantial numbers of AE events and counts accumulated at the points of load reversal, precluding the reliability of AE data at the ends of the load range.

Some intermediate load ranges produced more AE than their neighboring ranges, due to frictional contact of asperities on the internal crack faces, or crack propagation and arrest. However, the apparent upward drift of the load ranges in which AE occured may attest to the evolution of that particular AE site, as requiring a higher stress to force the contact of internal asperities, or the further growth of damage.

5.2.   Evolution of damage as tracked by internal friction and Young's modulus.

The increasing and decreasing behavior of internal friction and Young's modulus possibly indicates the fast initiation, growth and recovery of a major damage mode, probably the midplane shear crack which developed in the GFRP composite specimens. The similar behavior of Young's modulus and internal friction in the Macor specimens suggests that the progression of microcracking damage and recovery may have followed a similar evolution.

The change of internal friction relative to the change of Young's modulus (sensitivity ratio) was much greater at low loads than at the higher loads. The damage that occured at the low loads had the greater effect on internal friction. The higher loads had less effect on internal friction, and more of an effect on Young's modulus.

5.3.   Increasing variation of Young's modulus with maximum fatigue load.

One set of specimen and measurement point conditions provided a fairly clear trend of increasing variation of Young's modulus with increasing fatigue load. Seven Macor specimens, with Young's modulus measured at 0.012 n.d. contributed to the trend. Regression analysis gave the relation of approximately 2.0 MPa increase of modulus variation per 10 percent increase in fraction of M.O.R. (modulus of rupture), with a conditional standard deviation of 0.031 MPa.

5.4.   Evolution of Young's modulus and internal friction
with number of fatigue load cycles.

The Young's modulus and internal friction of both materials varied unexpectedly. Both materials displayed similar behavior of both physical properties versus loading cycles. Two possible damage mechanisms are: (1) the nonlinear progression of damage through the specimen and (2) an aggressive, fast acting recovery process. Nonlinear damage progression is not unlikely given the midplane shear crack that developed in the GFRP specimens under four point bending. Both materials recover to some degree, but mechanical flexural fatigue may periodically accelerate the damage.

Location of the source may be possible by using multiple transducers placed on the specimen and the use of appropriate software in the analysis computer. Source location may provide evidence of the nonlinear progression of damage through specimens of both materials.

The use of a 'guard transducer' is not necessary, due to the natural attenuation of machine and system noise through the mechanical interfaces between the specimen and the Instron.

5.5.   Afterview of experiment.

The detection and analysis of acoustic emission is a delicate and somewhat gray or subjective science. Much of the subjectivity is qualified by knowledge of the simultaneous behavior of other parameters, such as cracking or monitoring physical properties. Much care must be taken to assure one's self of the best possible AE information.

The unexpected results of small positive and negative changes in Young's modulus and internal friction were analyzed to pursue any trend or explanation. A return to the literature supported the possibility that there may

155

have been some physical recovery of Young's modulus and internal friction,
as a cyclically driven process.

5.6.   Recommendations for future work.

As exploratory experimentation, this study points out several directions of
further work.

It is recommended to design an experiment to mechanically induce a
homogeneous damage in the specimen. Homogeneous damage may enable
the correlation of acoustic emission with the other prime measures of damage,
namely internal friction and Young's modulus.

It is also important to determine, in situ, the physical properties of
Young's modulus and internal friction. The measurement of Young's
modulus after every load cycle may allow the close comparison or correlation
with AE detected during damage, regardless of the type of apparatus forcing
the damage.

Appendices

6. Appendices.

A. Physical properties of Macor, Corning code 9658 [79].

Composition: Glass-ceramic, 55% mica crystal, 45% matrix glass

Compound	Approximate weight %
SiO_2	46%
Al_2O_3	16%
MgO	17%
K_2O	10%
F	4%
B_2O_3	7%

Density:	2.52 g/cm^3
Porosity:	0
Hardness:	250 Knoop
Maximum use temperature:	1000 °C, 1832 °F, no load
Coefficient of thermal expansion:	94×10^{-7} in/in °C
	52×10^{-7} in/in °F
Compressive strength:	50,000 psi, 333 MPa
Flexural strength:	15,000 psi, 100 MPa
Dielectric strength:	1000 Volts-mil
Volume resistivity:	$>10^{14}$ ohm-cm

6.B. Physical properties of 3-M GFRP composite type 1003 [92].

Composition:	E-glass fiber reinforced epoxy matrix, 55% fibers, 45% matrix epoxy
Maximum use temperature:	120 °C (250 °F)

For unidirectional layup, at 21 °C:

Four point bending strength:	1150 MPa
Flexural modulus:	38.6 GPa
Tensile strength:	965 MPa
Tensile modulus:	39.3 GPa
Compressive strength:	880 MPa

References

References

1. Hasselman, D.P.H. "Unified Theory of Thermal Shock Fracture Initiation and Crack Propagation in Brittle Ceramics." J. Amer. Cer. Soc., 52 [11]: 600 - 604, 1969.

2. Kingery, W.D. "Factors Affecting Thermal Stress Resistance of Ceramic Materials." J. Amer. Cer. Soc., 38 [1]: 3 - 15, 1955.

3. Kim, Y., Lee, W.J. and Case, E.D. "Thermal Fatigue in SiC Fiber Reinforced Aluminosilicate Glass-Ceramic Composite." pp. 479 - 486 in Metal and Ceramic Matrix Composites: Processing, Modeling and Mechanical Behavior. Ed. by Bhagat, R.B. The Minerals, Metals and Materials Society, 1990.

4. Rogers, W.P., Emery, A.F., Bradt, R.C. and Kobayashi, A.S., "Statistical Study of Thermal Fracture of Ce ramic Materials in the Water Quench Test." J. Amer. Cer. Soc., 70 [6]: 406 - 412, 1987.

5. Evans, A.G. "Residual Stress Measurement Using Acoustic Emission." J. Amer. Cer. Soc., 58 [5 - 6]: 239 - 243, 1975.

6. Lewis III, D. and Rice, R.W. "Comparison of Static, Cyclic and Thermal-Shock Fatigue in Ceramic Composites." Cer. Eng. and Sci. Proc., 3 [9 - 10]: 714 - 721, 1982.

7. Lewis III, D. "Cyclic Mechanical Fatigue in Ceramic - Ceramic Composites -- An Update." Cer. Eng. and Sci. Proc., 4 [9 - 10]: 874 - 881, 1983.

8. Ewart, L. and Suresh, S. "Crack Propagation in Ceramics Under Cyclic Loads." J. Mat. Sci., 22: 1173 - 1192, 1987.

9. Evans, A.G. "Fatigue in Ceramics." Int'l Journal of Fracture, 16: 485 - 496, 1980.

10. Nishijima, S., Matsushita, K., Okada, T., Okamoto, T. and Hagihara, T. "Dynamic Young's Modulus and Internal Friction in Composite Materials." pp. 143 -151 in Nonmetallic Materials and Composites at Low Temperatures, Vol. 3. Ed. by Hartwig, G. and Evans, D. Plenum Press, N.Y. and London, 1986.

11. Matsushita, K., Kuratani,S., Okamoto, T. and Shimada, M., "Young's Modulus and Internal Friction in Alumina Subjected to Thermal Shock." J. of Mat. Sci. Letters, 5: 345 - 348, 1984.

12. Suzuki, S., Takahashi, M., Hickichi, Y. and Sakamura, H., "Internal Friction of Network-Forming Oxide Glasses in the Systems P_2O_5 - (GeO_2, TeO_2, Sb_2O_3, V_2O_5)." J. Amer. Cer. Soc., 70 [4]: 254 - 256, 1987.

13. Ono, T., Nagata, K., Hashiba, M., Miura, E., Nurishi, Y. and Shimada, T. "Internal Friction, Crack Length of Fracture Origin and Fracture Surface Energy in Alumina-Zirconia Composites." J. of Mat. Sci., 24: 1974 - 1978, 1984.

14. Marlowe, M. "Elasticity and Kilocycle Internal Friction of Y_2O_3." Master's Thesis, Dept. of Ceramic Eng. Iowa State Univ., Ames, Iowa 1963.

15. ASTM C 623 - 71 (1985). Standard Test Method for Young's Modulus, Shear Modulus and Poisson's Ratio for Glass and Glass-Ceramics by Resonance. Amer. Soc. for Testing of Materials, Vol. 15.02, Glass: Ceramic Whitewares, pp. 171 - 176, 1988.

16. ASTM C 848 - 78 (1983). Standard Test Method for Young's Modulus, Shear Modulus and Poisson's Ratio for Ceramic Whitewares by Resonance. Amer. Soc. for Testing of Materials, Vol. 15.02, Glass: Ceramic Whitewares, pp. 268 - 273, 1988.

17. ASTM C 747 - 74 (1979). Standard Test Method for Moduli of Elasticity and Fundamental Frequencies of Carbon and Graphite Materials by Sonic Resonance. Amer. Soc. for Testing of Materials, Vol. 15.01, Refractories: Carbon and Graphite and Products: Activated Carbon, pp.199 - 206, 1988.

18. Kolsky, H. Stress Waves in Solids. Oxford University Press, London England, pp. 15 - 22, 1953.

19. Zener, C. Elasticity and Anelasticity of Metals. University of Chicago Press, Chicago, Illinois, pp. 54 - 58, 1948.

20. Forster, F. "Ein Neues Messverfahrer zur Bestimmung des Elastzitatmodulus und der Dampfung." ("A New Method for Determing the Elastic Modulus and Damping"). Zeitschrift fur Metallkunde (Journal of Metallurgy), 29, [4]: 109 - 115, 1937.

21. Rayliegh, J.W.S. The Theory of Sound. Second Ed., Vol. 1, (1877). Dover Publications, New York, N.Y., pp. 31 - 37, 1945.

22. Pickett, G. "Equations for Computing Elastic Constants from Flexural and Torsional Resonant Frequencies of Vibration of Prisms and Cylinders." ASTM Proceedings, Amer. Soc. for Testing of Materials, 45: 846 - 865, 1945.

23. ASTM F - 417 - 78 (1984) Standard Test Method for Flexural Strength (Modulus of Rupture) of Electronic Grade Ceramics. Amer. Soc. for Testing of Materials, pp. 440 - 436, 1988.

24. ASTM C 203 - 85 Standard Test Method for Breaking Load and Flexural Properties of Block - Type Thermal Insulation. Amer. Soc. for Testing of Materials, Vol 4.06, Thermal Insulation: Environmental Acoustics, pp. 34 - 39, 1988.

25. ASTM C 158 - 84 Standard Test Method for Flexural Testing of Glass. Amer. Soc. for Testing of Materials, Vol. 15.02, Glass: Ceramic Whitewares, pp. 19 - 24, 1988.

26. Mullin, J.V. and Knoell, A.C. "Basic Concepts in Composite Beam Testing." Mat. Rsch. and Stds., 12: 16 - 33, 1970.

27. Bhatia, A.B. Ultrasonic Absorption. Oxford Press, U.K., pp. 40 43, 1967.

28. Volterra, E. and Zachmanoglou, E.C. Dynamics of Vibrations. C.E. Merrill Books, pp. 349 - 357, 1965.

29. Hamstead, M.A. "A Review: Acoustic Emission, a Tool for Composite Materials Studies." Experimental Mechanics, 24 [3]: 7 - 13, 1986.

30. Evans, A.G., Linzer, M. and Russel, L.R. "Acoustic Emission and Crack Propagation in Polycrystalline Alumina." Mat. Sci. and Eng., 15: 253 - 261, 1974.

31. Evans, A.G. and Linzer, M. "Failure Prediction in Structural Ceramics Using Acoustic Emission." J. Am. Cer. Soc., 56 [11]: 575 - 581, 1973.

32. Evans, A.G., Nadler, H. and Ono, K. "An Acoustic Emission Study of the Fracture of Zinc Selenide." Mat. Sci. and Eng., 22: 7 - 14, 1976.

33. Safai, S., Herman,H. and Ono, K. "Acoustic Emission Study of Thermal - Sprayed Oxide Coatings." Am. Cer. Soc. Bulletin, 58 [3]: 624, 1979.

34. Romrell, D.M. and Bunnell, L.R. "Monmitoring of Crack Growth in Ceramic by Acoustic Emission." Mat. Eval., 12, 267 - 271, 1970.

35. Evans, A.G., Tittman, B.R., Ahlberg, L., Khuri-Yakub, B.T. and Kino, G.S. "Ultrasonic Attenuation in Ceramics." J. Appl. Phys., 49 [5]: 2669 - 2679, 1978.

36. Evans, A.G., Linzer, M., Johnson, H., Hasselmann, D.P.H. and Kipp, M.E. "Thermal Fracture Studies in Ceramic Systems using an Acoustic Emission Technique." J. Mat. Sci., 10: 1608 - 1615, 1975.

37. Kazuhiro, E., Shigekawa, H. and Hyodo, S. "Acoustic Location of Fracture Origin in Optical Glass Fibers." J. Am. Cer. Soc., 67 [6]: C-104 - C-105, 1984.

38. Kahn, M. "Acoustic and Elastic Properties of PZT Ceramics with Anisotropic Pores." J. Am. Cer. Soc., 68 [11]: 623 - 628, 1985.

39. Jen, C-K., Chung, C-J., Shapiro, G., Monchalin, J-P., Langlois, P. and Bussiere, J.F. "Acoustic Characterization of Poling Effects in PZT Ceramics." J. Am. Cer. Soc., 70 [10]: C-256 - C-259, 1987.

40. Tseng, D., Long, Q.Y. and Tangri, K. "An Acoustic Emission Study of Martensitic Transformation of Retained Austenite in Intercritically Annealed HSLA Steels." Acta. Met., 35 [7]: 1887 - 1894, 1987.

41. Kraut, E.A. "Review of Theories of Scattering of Elastic Waves by Cracks." IEEE Trans. on Sonics and Ultrasonics, SU - 23 [3]: 162 - 167, 1976.

42. Dieter, G.E. Mechanical Metallurgy, Third Ed. McGraw Hill Inc., N.Y., pp. 137, 1986.

43. Operation Manual, PAC Acoustic Emission Computer Model 3000 / 3004. Physical Acoustics Corp. Sec. 5.5, p. 98 - 101, 1985.

44. Domany, E., Krumhansl, J.A. and Teitel, S. "Quasistatic Approximation to the Scattering of Elastic Waves by a Circular Crack." J. App. Phys., 49 [5]: 2599 - 2604, 1978.

45. Dickinson, J.T., Snyder, D.B. and Donaldson, E.E. "Acoustic Emission and Electron Emission During Deformation of Anodized Aluminum." J. Vac. Sci. and Tech., 17 [1]: 429 - 432, 1980.

46. Otsuka, H. "Variations on Acoustic Emission Between Graphite and Glass Epoxy Composites." J. Comp. Mat., 5 [11]: 591 - 597, 1981.

47. Shih, G. C. and Ebert, L. J. "Flexural Failure Mechanisms and Global Stress Plane for Unidirectional Composites Subjected to Four-Point Bending Tests." Composites, 17 [4]: 309 - 320, 1986.

48. Shih, G. C. and Ebert, L. J. "The Effect of the Fiber / Matrix Interface on the Flexural Fatigue Performance of Unidirectional Fiberglass Composites." Composites Sci. and Tech., 28: 137 - 161, 1987.

49. Rosensaft, M. and Marom, G. "Evaluation of Bending Test Methods for Composite Materials." Journal of Composites Technology and Research, 7 [1]: 12 - 16, 1987.

50. Davidovitz, M., et al. "Failure Modes and Fracture Mechanisms in Flexure of Kevlar - Epoxy Composites." J. Mat. Sci., 19: 377, 1984.

51. Hwang, W. and Han, K. S. "Interlaminar Fracture Behavior and Fiber Bridging of a Glass - Epoxy Composite Under Mode I Static and Cyclic Loadings." J. Comp. Mat., 23 [4]: 396 - 430, 1989.

52. Johnson, W. S. and Mangalgiri P. D. "Investigation of Fiber Bridging in a Double Cantilever Beam Specimen." J. Comp. Tech. and Rsch., 9: 10 - 13, 1987.

53. Mall, S., Ramamurthy, G. and Rezaizdeh, M. A. "Stress Ratio Effect on Cyclic Debonding in Adhesively Bonded Composite Joints." Composite Structures, 8: 31 - 45, 1987.

54. Wang, S. S. and Wang, H. T. "Interlaminar Crack Growth in Fiber Reinforced Composites During Fatigue." J. Eng. Mat. and Tech., 101 [1]: 34 - 41, 1979.

55. Hwang, W. and Han, K. S. "Fatigue of Composites - Fatigue Modulus Concept and Fatigue Life Prediction." J. Comp. Mat., 20 [3]: 154 - 165, 1986.

56. Hwang, W. and Han, K. S. "Cumulative Damage Models and Multi - Stress Fatigue Life Prediction." J. Comp. Mat., 20 [3]: 125 - 153, 1986.

57. Han, H. T. and Tsai, S. W. "On the Behavior of Composite Laminates After Initial Failure." J. Comp. Mat., 8: 285 - 305, 1974.

58. Han, H. T. and Kim, R. Y. "Fatigue Behavior of Composite Laminates." J. Comp. Mat., 10: 156 - 180, 1976.

59. Awerbuch, J. and Ghaffari, S. "Monitoring Progression of Matrix Splitting During Fatigue Loading Through Acoustic Emission in Notched Unidirectional Graphite / Epoxy Composite." Journal of Reinforced Plastics and Composites, 7: 245 - 264, 1988.

60. Eckles, W. and Awerbuch, J. "Monitoring Acoustic Emission in Cross - Ply Graphite / Epoxy Laminates During Fatigue Loading." Journal of Reinforced Plastics and Composites, 7: 265 - 283, 1988.

61. Awerbuch, J. Madhukar, M. and Gorman, M. "Monitoring Damage Accumulation in Filament - Wound Graphite / Epoxy Laminate Coupons During Fatigue Loading Through Acoustic Emission." Journal of Reinforced Plastics and Composites, 3: 2 - 39, 1984.

62. Favre, J. P. and Laizet, J. C. "Amplitude and Counts per Event Analysis of the Acoustic Emission Generated by the Transverse Cracking of Cross - Ply CFRP." Comp. Sci. and Tech., 36: 27 - 43, 1989.

63. Guild, F. J., Phillips, M. G. and Harris, B. "Amplitude Distribution Analysis of Acoustic Emission from Composites: A New Method of Data Presentation." J. Mat. Sci. Letters, 4: 1375 - 1378, 1985.

64. Henrat, P., Vautrin, A. and Harris, B. "Mechanical and Acoustic Emission Response of Unidirectional and Cross - Plied GRP Composites." Comp. Sci. and Tech., 30: 263 - 277, 1987.

65. Nixon, J. A., Phillips, M. G., Moore, D. R. and Prediger, R. S. "A Study of the Development of Impact Damage in Cross - Ply Carbon Fiber / PEEK Laminates Using Acoustic Emission." Comp. Sci. and Tech., 31: 1 - 14, 1988.

66. Lewis,D., Bulik, C. and Shadwell,D. "Standardized Testing of Refractory Matrix/Ceramic Fiber Composites." Ceramic Engineering and Science Proceedings, 6 [7 - 8]: 507 - 523, 1985.

67. Evans, A.G. "Perspective on the Develpoment of High-Toughness Ceramics." J. Am. Cer. Soc., 73 [2]: 187 - 206, 1990.

68. Evans, A.G. and Fuller, E.R. "Crack Propagation in Ceramic Materials Under Cyclic Loading Conditions." Met. Trans., 5 [1]: 27 - 33, 1974.

69. Smyth, K.K. and Magida, M.B. "Dynamic Fatigue of a Machinable Glass-Ceramic." J. Am. Cer. Soc., 66 [7]: 500 - 505, 1983.

70. Suresh, S. and Brockenbrough, J.R. "Theory and Experiments of Fracture in Cyclic Compression: Single Phase Ceramics, Transforming Ceramics and Ceramic Composites." Acta. Met., 36 [6]: 1455 - 1470, 1988.

71. Ewart, L. and Suresh, S. "Dynamic Fatigue Crack Growth in Polycrystalline Alumina under Cyclic Compression." J. Mat. Sci. Letters, 5: 774 - 778, 1986.

72. Rawlins, M.H., Nolan, T.A., Allard, L.F. and Tennery, V.J. "Dynamic and Static Fatigue Behavior of Sintered Silicon Nitrides: II, Microstructure and Failure Analysis." J. Am. Cer. Soc., 72 [8]: 1338 - 1342, 1989.

73. Ewart, L. and Suresh, S. "Crack Propagation in Ceramics under Cyclic Loads." J. Mat. Sci., 22: 1173 - 1192, 1987.

74. Han, L and Suresh, S. "High-Temperature Failure of an Alumina-Silicon Carbide Composite under Cyclis Loads: Mechanisms of Fatigue Crack-Tip Damage." J. Am. Cer. Soc., 72 [7]: 1233 - 1238, 1989.

75. Ritter, J.E. and Service, T.H. "Cyclic Fatigue and Reliability of Resinoid-Bonded Abrasive Materials." Mat. Sci. and Eng., 82: 231 - 239, 1986.

76. Brockenbrough, J.R., and Suresh, S. "Constitutive Behavior of a Microcracking Brittle Solid in Cyclic Compression." J. Mech. Phys. Solids, 35 [6]: 721 - 742, 1987.

77. Kawakubo, T. and Komeya, K. "Static and Cyclic Fatigue Behavior of a Sintered Silicon Nitride at Room Temperature." J. Am. Cer. Soc., 70 [6]: 400 - 405, 1987.

78. Lewis, D. III. "Observations on the Strength of a Commercial Glass-Ceramic." J. Am. Cer. Soc. Bulletin, 61 [11]: 1208 - 1214, 1982.

79. Macor Product Technical Bulletin, No. 1-R79. Corning Glass Works, Corning N.Y., 14830, 1989 .

80. Reece, M.J., Guiu, F. and Sammur, F.R. "Cyclic Fatigue Crack Propagation in Alumina under Direct Tension-Compression Loading." J. Am. Cer. Soc., 72 [2]: 348 - 352, 1989.

81. Jenkins, M.G., Kobayashi, A.S., White, K.W. and Bradt, R.C. "Crack Initiation and Arrest in a SiC Whisker / Alumina Matrix Composite." J. Am. Cer. Soc., 70 [6]: 393 - 395, 1987.

82. Lathabai, S., Nai, Y-W. and Lawn, B.R. "Cyclic Fatigue Behavior of an Alumina Ceramic with Crack-Resistance Characteristics." J. Am. Cer. Soc. Communications, 72 [9]: 1760 - 1763, 1989.

83. Ritchie, R.O. "Crack Tip Shielding in Fatigue." Mechanical Behavior of Materials - 5. Ed. by Yan, M.G., Zhang, S.H. and Zheng, Z.M. Proceedings of the Fifth International Conference, Vol 2. Beijing, China, June 3 - 6, pp. 1399 - 1417. Pergammon Press, 1987.

84. Green, D.J. "Micromechanisms of Brittle Failure in Ceramics." Mechanical Behavior of Materials - 5. Ed. by Yan, M.G., Zhang, S.H. and Zheng, Z.M. Proceedings of the Fifth International Conference, Vol. 2. Beijing, China, June 3 - 6, pp. 19 - 47. Pergammon Press 1987.

85. Case, E.D. "The Effect of Microcracking upon the Poisson's Ratio for Brittle Materials." J. Mat. Sci., 19: 3702 - 3712, 1984.

86. Wachtman, J.B. and Tefft, W.E. "Effect of Suspension Position on Apparent Values in Internal Friction Determined by Forster's Method." Review of Scientific Instruments, 29: 517 - 520, 1958.

87. Kim, Y. and Case, E.D. "Time - dependent Elastic Modulus Recovery Measurement on Thermally Shocked SiC fiber/Aluminosilicate Composites, Machinable Glass Ceramics and Polycrystalline Alumina." Michigan State University. To be published, 1990.

88. Stravrinidis, B. and Holloway, D.G. "Crack Healing in Glass." Physics and Chemistry of Glass, 24 [1]: 19 - 25, 1983.

89. Michalske, T.A. and Fuller, E.R. "Closure and Repropagation of Healed Cracks in Silicate Glass", J. Amer. Cer. Soc., 68 [11]: 586 - 590, 1985.

90. Inagaki, M., Urashima, K., Toyomasu, S. Goto, Y. and Sakai, M. "Work of Fracture and Crack Healing in Glass." J. Amer. Cer. Soc., 68 [12]: 704 - 706, 1985.

91. Pulliam, G. "Precipitaion in Microscopic Cracks". J. Amer. Cer. Soc., 42 [10]: 477 - 482, 1959.

92. 3M Technical Bulletin, Material Type 1003. 3M Corp. Minnesota, MN 1988.